Winter 12-15-2018

Biosensing by “Growing” Antennas and Error-correcting Codes

Mingquan Yuan
Washington University in St. Louis

WASHINGTON UNIVERSITY IN ST.LOUIS

School of Engineering & Applied Science
Department of Computer Science and Engineering

Dissertation Examination Committee:
Shantanu Chakrabartty, Chair
Roger Chamberlain
Erica Scheller
Srikanth Singamaneni
Xuan Zhang

Biosensing by "Growing" Antennas and Error-correcting Codes

by
Mingquan Yuan

A dissertation presented to
The Graduate School
of Washington University in
partial fulfillment of the
requirements for the degree
of Doctor of Philosophy

December 2018
St. Louis, Missouri

Table of Contents

List of Figures

List of Tables

Acknowledgments

During my graduate study at both Michigan State University and Washington University in St. Louis, I have received enormous encouragement and support from many people, and this dissertation would not have been possible without them.

First and foremost, I would like to express my deepest gratitude to my adviser, Dr. Shantanu Chakrabartty, for guiding me through my time in his research lab. None of the work described in this dissertation would have been possible without his guidance and support. He has always been approachable, supportive and insightful during my entire course of Ph.D. study. Discussion with him has always been a pleasure as I always get valuable advice and inspiration from him. I have learned from him more than just research. His curiosity to unknown field, creativity for problem solving, and enthusiasm for research have provided an excellent example for me and will have an impact on me for my future career and the rest of my life.

I am also grateful to Dr. Evangelyn C. Alocilja at Michigan State University for introducing me to the field of biosensor and providing me with a professional, helpful and joyful lab environment to conduct my research. I am also grateful to all the Nano-Biosensors Laboratory members who have had helped me during my stay there – Yun Wang, Kasey Felten, Patrick Fewins, and Leann Matta to name a few. I would also like to thank Dr. Prem Chahal and Brian Wright at Michigan State University for their valuable suggestions and help.

I would also like to express my thanks to Dr. Srikanth Singamaneni for providing me with all kinds of resources and help to conduct my research. The enthusiasm he has for research is always motivational for me. I am also grateful for the opportunities he has provided for me to interact with many gifted, diligent and helpful graduate students in the Soft Nanomaterials Laboratory – Keng-Ku Liu, Qisheng Jiang, Zheyu Wang, and Rohit Gupta to name a few.

I would also like to thank the rest of my committee: Dr. Roger Chamberlain, Dr. Erica L. Scheller and Dr. Xuan 'Silvia' Zhang for their time, thoughtful comments and suggestions to my research and to this dissertation.

I would also thank all the past and current members of the Adaptive Integrated Microsystems Lab: Kenji Aono, Tao Feng, Liang Zhou, Hassan Khan, Yarub Alazzawi, Ahana Gangopadhyay, Oindrila Chatterjee, Brittany Scheid, Sri Harsha Kondapalli, Darshit Mehta, and Owen Pochettino for research brainstorming and hanging out together. I am also grateful to Dr. Dihui Lai for supervising my internship at RGA. Additionally, I would like to thank all the friends I have made since I started my Ph.D. journey. My time in East Lansing and St. Louis has been a lot of fun because of them.

Last but not the least, I owe the largest debt of gratitude to my family for their endless love. They have always been there when I need them. In particular, I would like to thank my wife, Fan Yang. She has been exceptionally supportive and encouraging. I cannot complete this journey without her by my side.

Mingquan Yuan

Washington University in Saint Louis

December 2018

To my family

ABSTRACT OF THE DISSERTATION

Biosensing by "Growing" Antennas and Error-correcting Codes

by

Mingquan Yuan

Doctor of Philosophy in Computer Science

Washington University in St. Louis, 2018

Professor Shantanu Chakrabartty, Chair

Food-borne disease outbreaks not only cause numerous fatalities every year but also contribute to significant economic losses. While end-to-end supply chain monitoring can be one of the keys to preventing these outbreaks, screening every food product in the supply chain is not feasible considering the sheer volume and prohibitive test costs. Fortunately, two converging economic trends promise to make this end-to-end supply chain monitoring possible. The first trend is that passive radio-frequency identification (RFID) tags and quick response (QR) codes are now widely accepted for food packaging. The second trend is that smartphones are now equipped with the capability to interrogate RFID tags or to decode QR codes. Together, they have opened up the possibility of monitoring food quality by endowing these tags and error-correcting codes with the capability to detect pathogenic contaminants. This dissertation investigates a biosensing paradigm of "growing" transducer structures, such as RFID tags and QR codes, which is triggered only when analytes of interest are present in the sample. This transducer growth or self-assembly process relies on a silver enhancement technique through which silver ions reduce into metallic form in the presence of a target analyte, which in turn leads to changes in electrical or optical properties. By exploiting this, we first demonstrate two remote biosensor platforms, a RFID tag-based biosensor and a QR code-based biosensor, respectively. For the RFID-based biosensor, a chain of silver-shelled

particles is assembled during the analyte detection process, which directly modulates the antenna's effective impedance, and hence leads to an improvement in the tag's reflection efficiency. For the QR code-based biosensor, the operating principle relies on the optical absorption changes resulting from silver enhancement. The target detection process assembles an invalid code-word into a valid QR code. This self-assembly sensing approach should produce few false positives since it is a process which transits from a high entropy state (disassembled transducer) to a low entropy state (assembled transducer). While there can be numerous states of a disassembled transducer structure, there are only a few configurations representing the assembled transducer state. Given that there are no active power sources on the RFID tag or the QR code, it is challenging for the proposed biosensors to perform sample acquisition and pre-processing since they are envisioned to be embedded inside food packages eventually. Paper-based microfluidics have been explored and integrated on the biosensors to provide a self-powered approach for reagent sampling and processing. One use case is to trigger target detection remotely by an end consumer. Thermal absorption properties of graphite have been exploited such that the end user can initiate the process of analyte sampling in paper-based biosensors by shining a beam of light on the sensor.

Chapter 1

Introduction

1.1 Motivation

According to Centers for Disease Control and Prevention (CDC), every year in the United States, food-borne diseases sicken 48,000,000 people (roughly 1 in 6), causing 128,000 of them to be hospitalized, and killing 3,000 [9]. Beyond the fatalities, there are also huge losses related to medical care and food product recalls. The United States Department of Agriculture (USDA) estimates an annual medical care cost of $15.6 billion is caused by food-borne illnesses due to 15 major pathogens [8, 16, 34]. More recent research [78] estimates that an average national cost of $55.5 billion in the United States is directly related to food-borne illness. Other costs of food-borne illness come from product recalls. In 2011, the Grocery Manufacturers Association (GMA) surveyed 36 food companies, and found that more than half had experienced a product recall in the past five years [6]. According to the same survey, the average direct cost for a food product recall in the United States was $10

Figure 1.1: Illustration of end-to-end monitoring of food quality in a supply chain where RFID based and QR code based biosensors can be wirelessly interrogated at different locations of the supply chain.

million, which does not include indirect costs, such as lawsuits, loss of reputation, and sales losses.

End-to-end supply chain monitoring can be one of the keys to preventing these food-borne disease outbreaks and product recalls. However, practically speaking, it is infeasible to test and analyze all food samples at every point in the supply chain, for at least three reasons: 1) Traditional laboratory testing is time consuming (ranging from hours to days) and expensive. 2) The task of screening every product becomes impractical for the sheer volume of products that passes through the supply chain. 3) Food is typically enclosed in a package, where as traditional testing requires direct access to the sample analyte.

Fortunately, two converging economic trends promise to make end-to-end supply chain monitoring possible. The first trend is that passive radio-frequency identification (RFID) tags and quick response (QR) codes are now very widely accepted for food packaging (as shown in Fig. 1.1). For instance, Walmart has required its top 100 suppliers to use RFID for tagging cases and pallets of goods since January 2005 [84]. In the meantime, the price of passive RFID tags has fallen by orders of magnitude when compared to the cost of packaging materials over the last decade (less than \$0.10 per tag) [4, 108]. As a result, it is now economically viable

to embed or attach a passive tag to every package of a food item. The second trend, also illustrated in Fig. 1.1, is that the new generation of smartphones have been equipped with capabilities such as interrogating RFID tags or decoding QR codes and uploading scanned information to the cloud. These two converging economic trends make end-to-end supply chain monitoring possible through crowdsourcing the process of scanning RFID tags and product codes to consumers. Given the rapid penetration of smartphones in the consumer market, RFID tags or QR codes can be interrogated at different segments of the supply chain, from the food source all the way to the market shelves. Thus, an integrated platform combining a biosensing mechanism for detecting contaminants with inexpensive passive RFID tags or QR codes could be an attractive technology to continuously and wirelessly monitor the quality of a food product in a supply chain. The missing part is the technical ability to reliably detect pathogens or contaminants in food samples using passive RFID tag or QR code. Considering the fact that these passive devices do not have access to continuous power sources, it is challenging to design them to perform sample analyte acquisition, pre-processing and analysis. This dissertation will begin to address these challenges.

1.2 Contributions

Key contributions of this dissertation are summarized as follows:

1. *Target detection process assembles sensor structures.* At the core of our proposed RFID based biosensing approach is to assemble a chain of the RF antennas directly with silver enhancement in the presence of target analyte. The impedance matching between the antenna and silicon chip (or equivalently, the antenna's reflection efficiency) is improved by this self-assembling detection process. While there can be numerous states of a disassembled antenna, there are only a few configurations that represent an

assembled and tuned antenna. Therefore, it is highly unlikely that random environmental processes could produce a low-entropy state of a tuned antenna, and hence the process of antenna self-assembly should produce fewer false positives than widely reported detuning approaches. Similarly, the operating principle of the QR code based biosensor described in this dissertation is also to "grow" parts of code-word structures at a controlled rate through self-assembly using silver enhancement. Different from taking advantage of an electrical property change due to silver enhancement in the RFID based biosensor design, the QR code based biosensor relies on an optical absorption change in specific areas of the code-word, also due to silver enhancement. Except for this slight difference, both share the same spirit which is to construct a complete sensor structure based on target analyte detection, which should yield lower false positives and higher reliability. To the best of my knowledge, this is the first reported study that describes the design of biosensors that "grow" transducer structures based on self-assembly which is triggered only when the target pathogens are present in the sample.

2. *Self-powered continuous biosensing based on integration of paper-based microfluidics.* For many applications, there exists a need to monitor the quality of the product at every point of the supply chain so as to detect and track the source of food-borne pathogen contamination. Given that there are no active sources of power on a passive RFID tag or a QR code for acquiring and processing the sample, it is challenging for the proposed biosensor to perform sample acquisition and pre-processing since they are envisioned to be embedded inside food packages eventually. In this dissertation, paper-based microfluidics have been explored and integrated on the two types of biosensors to sample the analyte and direct it into regions where portions of the transducer structure could self-assemble. As a result, self-powered monitoring of product quality in a supply chain is envisioned to be possible by integrating paper-based microfluidics.

3. *Remote activation of analyte sampling based on light absorption.* In a conventional sampling process, the reagent is physically applied (using a pipette or a dipstick) to the sensing region. While this sampling approach is convenient for cases when the analyte can be directly accessed, it is impractical where the analyte is packaged or sealed. This scenario routinely occurs in the food and medicinal supply chains, where the samples are packaged and shipped in sealed containers. As a result, there is a need to monitor the product quality without opening the package. In this study, we use light as a trigger signal to remotely activate the analyte sampling. A graphite layer patterned as a light-absorbing material efficiently converts the light into heat. The resulting change in temperature due to infrared absorption leads to a thermal gradient that then exerts a diffusive force driving the analyte toward the regions of self-assembly. The working principle has been verified in this dissertation, where we demonstrate a higher sample flow rate due to light induced thermal gradients.

1.3 Organization of the dissertation

This dissertation shows that remote biosensing for end-to-end supply chain monitoring is possible by "growing" parts of transducer structures (RF antennas or QR code-words). The remainder of this dissertation addresses several key challenges achieving this goal and is organized as follows:

Chapter 2 In this chapter we first briefly describe the process of silver enhancement, then consider the first-order approximation of received signal strength and finite-element model used for simulating the RFID biosensor. This chapter also describes the model for and simulation of a ratiometric RFID configuration used for compensation and calibration. Two proof-of-concept applications of the proposed technique (detection of

IgG in rabbit serum, and detection of moisture in a sample) are demonstrated in this chapter to verify the proposed sensing approach. The chapter ends with a summary and discussion of future research directions.

The contents of this chapter are largely based on papers [96, 99, 101] co-authored with Dr. Evangelyn C. Alocilja, Dr. Premjeet Chahal and Dr. Shantanu Chakrabartty.

Chapter 3 In this chapter we introduce the operating principle of the proposed QR code based biosensor, including the basics of a QR code and QR code self-assembly via silver enhancement. The materials and methods used to prepare the QR code biosensor and the experimental setup are then described. Four different substrates, including regular copy paper, Whatman filter paper, nitrocellulose membrane and lab synthesized bacterial cellulose, are used for the QR code biosensor prototype fabrication. Measurements obtained using the fabricated biosensor prototypes are included in this chapter as well.

This chapter is mainly based on papers [103, 105] co-authored with Dr. Shantanu Chakrabartty, Dr. Qisheng Jiang, Dr. Keng-Ku Liu and Dr. Srikanth Singamaneni.

Chapter 4 Because the biosensor is envisioned to be integrated inside the food package, a self-powered approach that can sample and process the reagent and control its flow over time is necessary. This chapter mainly extends the work described in Chapter 2 and Chapter 3 by integrating paper-based microfluidics on RFID based and QR code based biosensors to enable self-powered acquisition and pre-processing of samples to the sensing regions. We also show the materials and methods used to integrate the paper-based microfluidics channels on the RFID based biosensor and the QR code based biosensor. This chapter also includes measurements obtained using both fabricated biosensor prototypes. It ends with a summary and discussion of possible future work.

The contents of this chapter are mainly based on a paper [95] co-authored with Dr. Evangelyn C. Alocilja and Dr. Shantanu Chakrabartty and a paper [105] co-authored with Dr. Shantanu Chakrabartty, Dr. Keng-Ku Liu and Dr. Srikanth Singamaneni.

Chapter 5 In this chapter we exploit graphite's thermal absorption properties to drive the process of analyte sampling in paper-based biosensors, which could potentially enable an end user to remotely trigger the sensing process. Our proposed operating principle is first described in this chapter, and is then followed with the methods used to prepare the prototype. The experimental setup and related measurements are also included.

This chapter is based on the papers [103, 104] co-authored with Dr. Shantanu Chakrabartty, Dr. Keng-Ku Liu and Dr. Srikanth Singamaneni.

Chapter 6 In this chapter, we propose to construct a colorimetric XNOR biomolecular logic gate for multi-analyte detection. The two target analytes represent two inputs to the XNOR gate. The absence (or presence) of the target analyte defines logic input 0 (or 1). The proposed hypothetical operating principle is described in detail, which is then followed with experiments designed to verify this hypothesis. According to the experiment results, it does not work out as expected due to an invalid key assumption made at early stage. Some reflections have also been included in this chapter.

Chapter 7 This chapter summarizes the dissertation and concludes with some potential future directions.

Chapter 2

Wireless Biosensing by Self-assembling RFID Antennas

In this chapter, we present a silver-enhancement technique for self-assembling radio-frequency (RF) antennas and demonstrate its application for remote biosensing. When target analytes or pathogens are present in a sample the silver-enhancement process self-assembles a chain of micro-monopole antennas. As the size of the silver-enhanced particles grows, the chain of micro-antenna segments bridge together to complete a macro-antenna structure. The change in the electrical impedance across the bridge modulates the reflection properties of the antenna at a desired frequency. We have used this principle to model, optimize and design a ratiometric mode 915 MHz radio-frequency identification (RFID) based biosensor which uses relative received signal strength indicator (RSSI) to measure and detect different concentration levels of target analytes. We have validated the proof-of-concept for detecting two types of analytes: (a) IgG in rabbit serum at concentration levels ranging from 20 ng to 60 ng; and (b) moisture in a sample at volumes ranging from 5μl to 40μl. A significant advantage of the proposed biosensor is that the concentration level of target analytes or

pathogens can be remotely interrogated in a concealed, packaged or in a bio-hazardous environment, where direct electrical or optical measurement is considered to be impractical.

2.1 Introduction

RFID technology is attractive for biosensing applications because the sensors can be wirelessly interrogated when operating in a concealed, packaged or in a bio-hazardous environment where direct measurement is not considered to be practical. The scenario is specifically relevant for monitoring a product supply-chain (shown in Fig. 2.1) where the use of passive RFID tagging technology is becoming more wide-spread [3, 75]. Integrating biosensing capabilities with passive RFID tags ensures that the sensors are low-cost and because these sensor-tags operate without batteries, their shelf-life is comparable to the products being monitored. To date most RFID based biosensors operate on a unifying principle which is to modulate the electrical impedance seen at the terminals of an RFID antenna [10]. The modulation then changes the RF reflection properties of the tag which can then be measured remotely using an RFID reader. For example, RFID based humidity sensors reported in [12, 38, 80] integrate a layer of water absorbing material on the surface of the tag. Moisture absorption on the layer changes the dielectric constant of the layer which in turn changes the effective impedance of the RFID antenna and hence its reflection properties [12, 38, 80]. The principle has also been used for detecting bio-analytes and bio-markers. For instance, in [17] a molecular imprinted polymer (MIP) based passive RFID sensor was reported for detecting histamines in spoiled fish. Another example is a split-ring resonator (SRR) based RFID biosensor which was reported in [49, 50] and used for detecting prostrate-specific antigen (PSA), a prostrate cancer bio-marker.

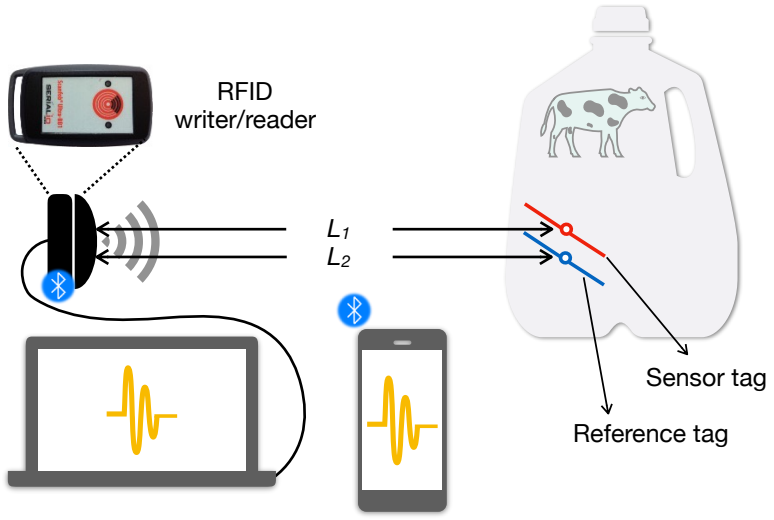

Figure 2.1: Illustration of the RFID tag integrated inside a package and being interrogated by an RFID reader (bluetooth reader shown). Data from the RFID reader can be retrieved by a laptop or using a smartphone via a bluetooth connection.

In this chapter, we propose an alternative concept for implementing a RFID based biosensor. Based on the presence of different concentration levels of target analytes, the structure of the antenna changes leading to the change in the antenna's reflection properties. At the core of this method is a silver-enhancement process that self-assembles parts of the RFID antenna in the presence of target analytes. Compared to conventional approaches, the proposed method has several advantages:

1. This approach can be easily integrated with existing commercial off-the-shelf RFID tags because it is generally easier to modify the large surface area spanned by the antenna rather than manipulating the microscale silicon die hosting the RFID electronics.

2. Because of the large surface area, different parts of the antenna could be functionalized with different types of detection probes, implying that the proposed approach could be easily extended for multi-analyte detection.

3. Because the effective length of the antenna could be directly modified, the proposed approach could be used to obtain a quantitative estimate of the analyte concentration without the need for additional peripheral measurement system.

4. the silver-enhancement process is materially compatible with conventional silver-ink based printable RFID tags and can be extended to flexible substrates.

This chapter is organized as follows: In section 2.2 we briefly describe the process of silver enhancement followed by section 2.3 which describes the finite-element model used for simulating the RFID biosensor. Section 2.3 also describes the model and simulation of a ratiometric RFID configuration used for compensation and calibration purposes. Section 2.4 describes two proof-of-concept applications of the proposed technique: detection of IgG in rabbit serum and detection of moisture in a sample. Section 2.5 presents a discussion of the proposed method highlighting its limitations and challenges. Section 2.6 then concludes this chapter with discussions about the future research directions.

2.2 Operating principle of silver enhancement

The proposed RFID biosensor is based on the physics of silver-enhancement [61, 62] and is illustrated in Fig. 2.2. Gold nanoparticles conjugated with target bioreceptors (for example antibodies shown in Fig. 2.2) or embedded inside a matrix, are first immobilized between two conductive electrodes as shown in Fig. 2.2(a) and the corresponding micrograph. Note that the gold nanoparticles are not large enough to electrically bridge the separated electrodes. This state corresponds to an open-circuit state where practically no DC current flows between the two electrodes. When a silver-enhancement solution comprising of Ag ions (I) and hydroquinone (photographic developing solution) is applied between the electrodes, gold nanoparticles are exposed to the silver-enhancement solution. In the presence of reducing

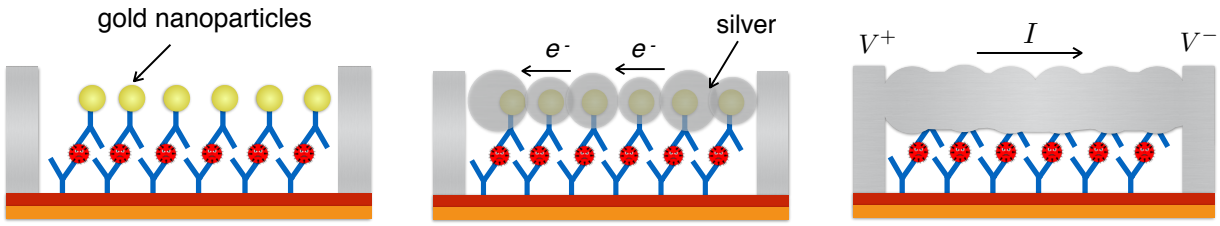

(a) isolation mode (b) subthreshold mode (c) above-threshold mode

Figure 2.2: Illustration of three stages of the silver-enhancement process: (a) before the silver enhancement solution applied, the electrodes are electrically isolated; (b) during the silver enhancement process, the silver ions get reduced to form metallic silver; (c) the path between the two electrodes are electrically bridged and more silver ions are reduced.

agent hydroquinone, the silver ions reduce into metallic silver on the surface of the gold nanoparticles. During this reaction, the gold nanoparticle acts as a catalyst and facilitates further reduction of silver ions. As more silver ions are reduced, a chain of gold nanoparticle cored silver micromonopole antennas self-assembles in between the electrodes as shown in Fig. 2.2(b). As a result, noticeable current can flow between the two electrodes due to displacement currents or due to electron hopping and tunneling. This constitutes a sub-threshold state where the conductive bridge between the electrodes still has not completely formed. With the progression of time and in the presence of more analytes, more silver ions gets reduced and in the limit the chain of micromonopole antennas gets completely bridged as shown in Fig. 2.2(c). Electrons can now freely flow when a potential difference is applied across the two electrodes.

A relationship between the time of silver enhancement process and the size of self-assembled silver particles is shown in Fig. 2.3. When sufficient silver enhancement solution is present, the increase of the particle size is monotonic and almost linear with respect to the time of silver enhancement process. In [62] we reported that the conductance measured between the electrodes after the silver enhancement process is monotonic with respect to the concentration of the target analyte. Details of the experimental results can be found in [61, 62] and have

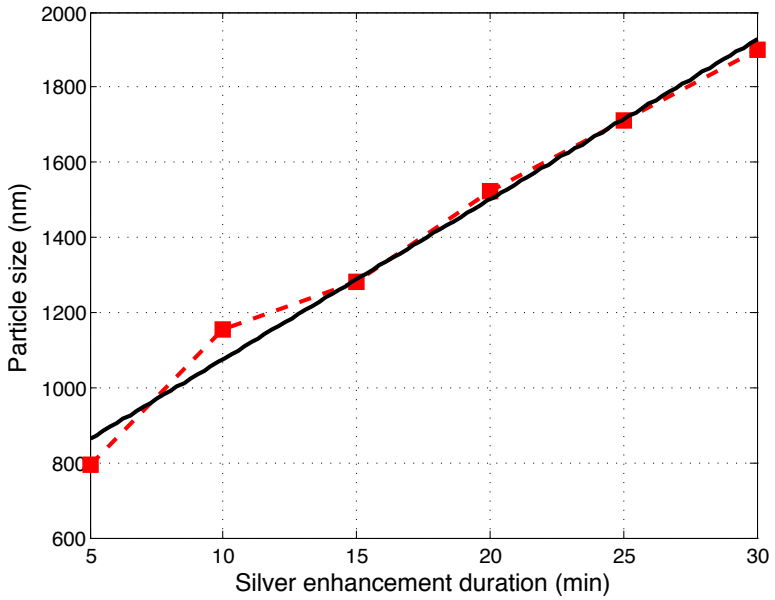

Figure 2.3: Relationship showing the size of reduced silver particles and the total silver enhancement duration.

been omitted for the sake of brevity. The change in conductance could potentially change the reflectance property of the self-assembled RF antenna which can then be used to infer the concentration of the target analyte. Therefore, the starting point of our simulation would be to determine the effect of antenna's reflection properties due to change in conductance because of silver-enhancement.

2.3 Modeling and analysis

2.3.1 Received signal strength first-order approximation

Since the interrogation of the RFID biosensor relies on detecting changes in the reflection properties of the RFID antenna, Friis transmission equation can be used to understand the relationship between the power received at the sensor's antenna P_r and the power of the interrogation signal P_t. The relationship can be expressed as:

$$\frac{P_r}{P_t} = G_t G_r \left(\frac{\lambda}{4\pi L}\right)^2 \tag{2.1}$$

where G_t and G_r are the respective gains of the reader and sensor antennas, λ is the wavelength of the RF signal, and L is the distance between the reader and the tag. The power transfered to the tag electronics, P_{ic}, and the reflected power received at the reader, P_{reader}, can be expressed using equations (2.2) and (2.3) as:

$$P_{ic} = P_r(1 - \Gamma_1) \tag{2.2}$$

$$P_{reader} = P_{ic} G_t G_r \left(\frac{\lambda}{4\pi L}\right)^2 (1 - \Gamma_2) \tag{2.3}$$

where Γ_1 and Γ_2 are input and output reflection coefficients, respectively. For the sake of simplicity we will assume that the two reflection coefficients are equal:

$$\Gamma_1 = \Gamma_2 = \Gamma \tag{2.4}$$

which leads to the reflected power received at the reader as:

$$P_{reader} = P_t \left[G_t G_r \left(\frac{\lambda}{4\pi L}\right)^2\right]^2 (1 - \Gamma)^2 \tag{2.5}$$

Equation (2.5) shows that the received power P_{reader} can be used to infer the magnitude of the reflection coefficient. To eliminate the non-relevant terms in equation (2.5), a control tag is used which is co-located with the sensor tag. Thus, the terms P_t, G_t, G_r, λ and L are

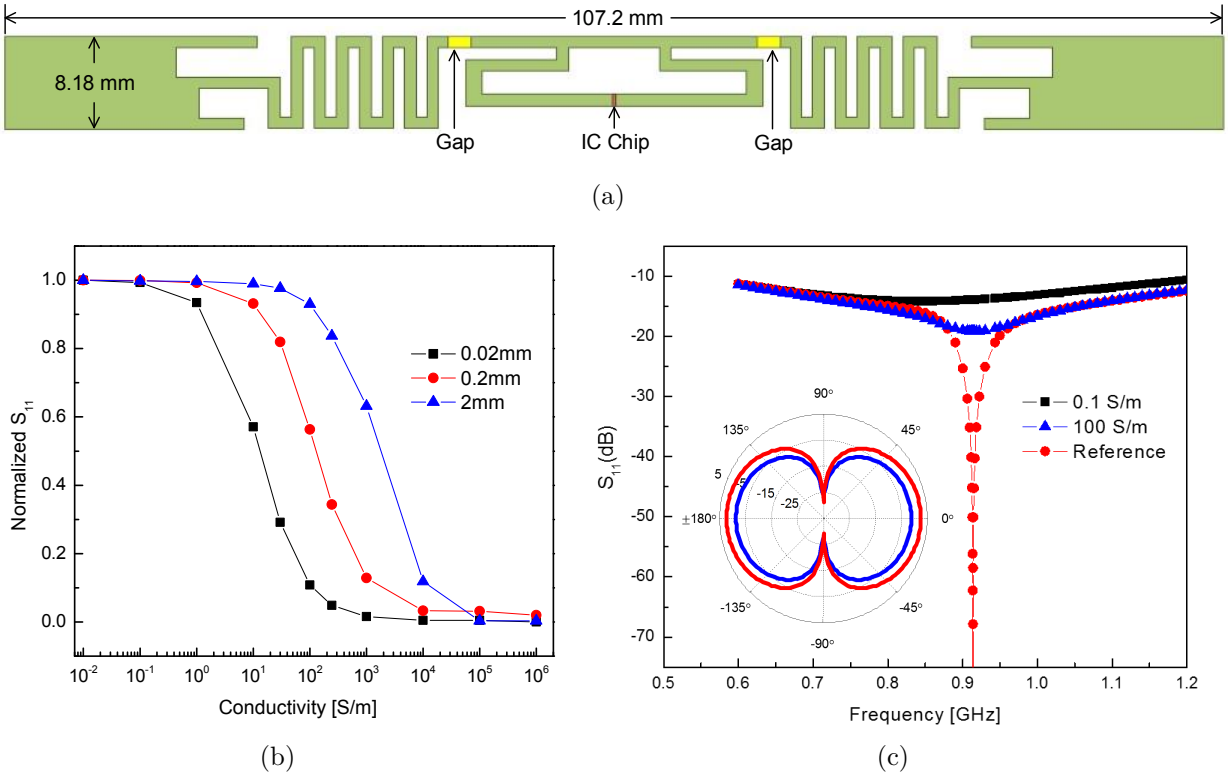

Figure 2.4: (a) Finite-element model of resistance loaded ALN-9640 RFID tag, the gap formed is for resistance loading; (b) Simulated S_{11} at 915MHz for different conductance values of the gap material and gap sizes; (c) Simulated S_{11} as a function of frequency for different conductances of the gap material and for the gap length of 0.2mm.

common to both the tags. Thus, the ratio of the power received from the sensor tag and the power received from the control tag can be expressed as:

$$\frac{P^s_{reader}}{P^c_{reader}} = \frac{(1-\Gamma_s)^2}{(1-\Gamma_c)^2} \tag{2.6}$$

where P^s_{reader}, Γ_s, P^c_{reader} and Γ_c denote the received power and reflection coefficients for the sensor tag and the control tag, respectively.

2.3.2 Finite-element modeling

Equation (2.6) only represents a generic first-order relationship between the reflected power and a tag antenna. To obtain results more specific to a particular type of antenna and tag configuration, we resort to finite-element simulations of the antenna's radiated power. For this study we chose an antenna configuration corresponding to commercial ALN-9640 915MHz RFID tag [2], which is shown in Fig. 2.4(a). The antenna is constructed using Aluminum and a gap is introduced in the antenna (marked by yellow in Fig. 2.4(a)) where the silver-enhancement based sensor could be integrated. For this study we have assumed that the sensor can be modeled using a material whose conductivity changes based on the degree of silver-enhancement as described previously. For the sake of symmetry, the silver-enhancement was integrated on both sides of the antenna and the RF reflection properties of the structure was modeled using HFSS.

The reflection coefficient Γ in equation (2.6) can then be estimated using the antenna's scattering parameter S_{11} [46]. Fig. 2.4(b) shows the relationship between the simulated S_{11} at 915MHz and different values of conductances for the material in the gap. The results show that lower value of reflection coefficients (S_{11}) can be reached when the material has a conductance equal to that of aluminum, due to superior impedance matching. As the conductance of the material reduces, the impedance mismatch increases the magnitude of S_{11}. This trend is observed for different gap lengths (shown in Fig. 2.4(b)), except that for smaller gap length, the change in S_{11} occurs at lower conductances. This study shows that the changes in reflection properties can be used to detect two orders of change in conductance. Fig. 2.4(c) shows the frequency characteristics of the antenna for different values of material conductances as compared to the control (or reference) tag which does not have any gap.

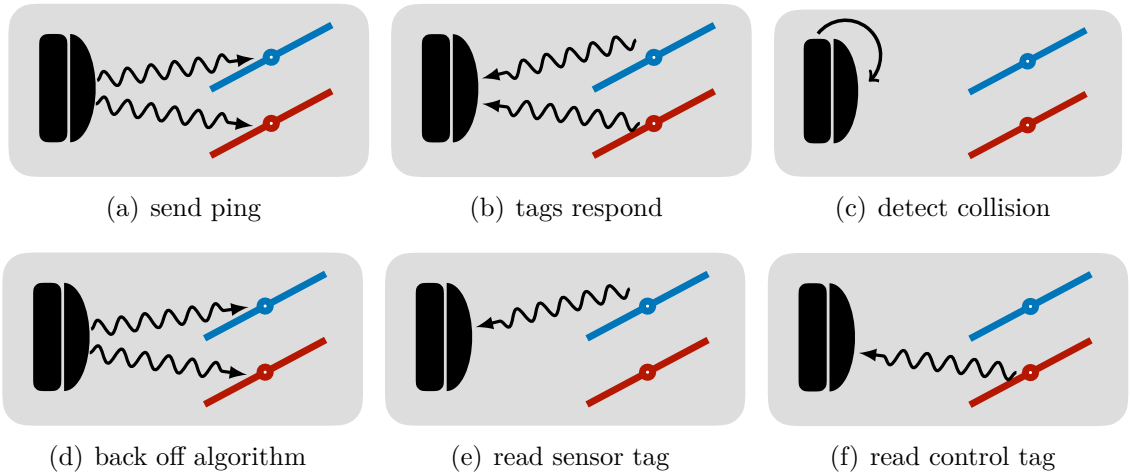

(a) send ping (b) tags respond (c) detect collision

(d) back off algorithm (e) read sensor tag (f) read control tag

Figure 2.5: Using multi-access capability of Gen-2 UHF RFID protocol for ratiometric RSSI measurement.

The results clearly show a change in the scattering parameter plot (also show in the polar plot in the inset) due to impedance loading of the antenna.

2.3.3 Loading effect of control tag and ratiometric readout

In the next set of simulation studies, we evaluated the loading effect of the control tag on the sensor antenna. As was described in section 2.3.1, the control tag has the similar antenna structure and co-located with the sensor tag for ratiometric compensation. Note that the current RFID standards like the Gen-2 UHF standard support multi-access capability where different tags (with different identification codes) can be interrogated separately using a random back-off algorithm [20]. The protocol is illustrated in Fig. 2.5 where the reader first pings both the tags (state (a)) in its neighborhood. Then, both the tags respond to the ping (state (b)) and the reader then detect a collision (state (c)). The reader then instructs the tags to respond after a random delay (state (d)) after which each of the tags respond separately (state (e) and (f)).

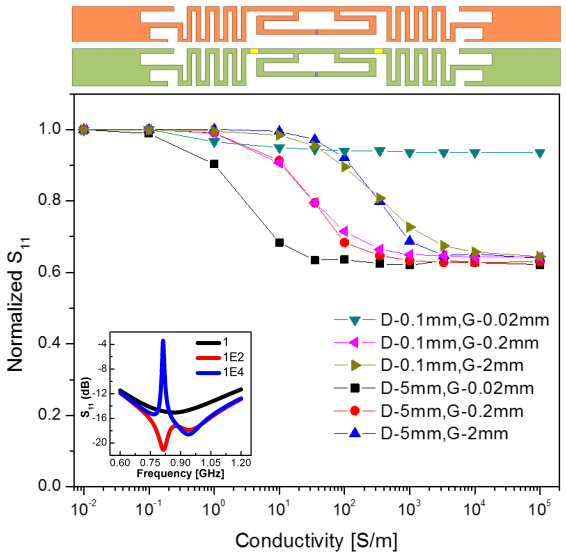

(a) Located on the same plane

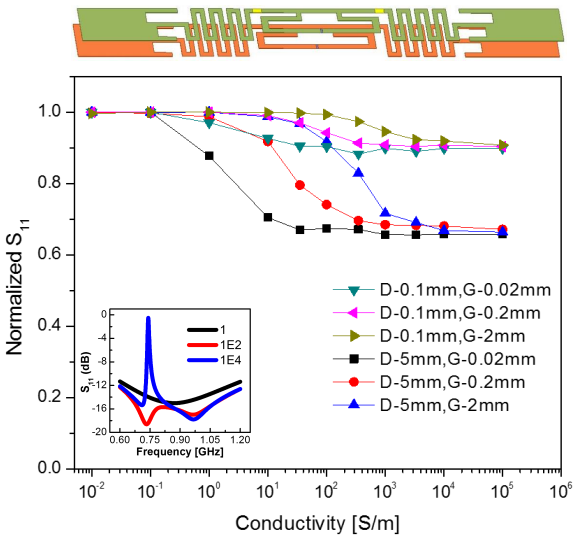

(b) Stacked vertically

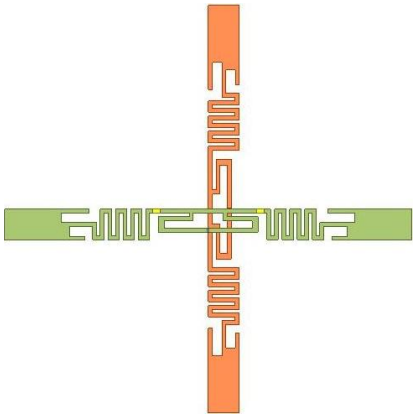

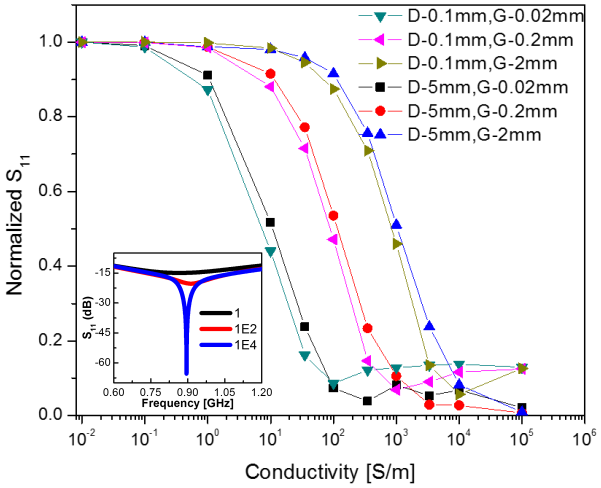

(c) Oriented 90^o with respect to each other

Figure 2.6: Simulated S_{11} for a ratiometric readout comprising of a sensor tag (shown in green) and calibration tag (shown in orange) placed in different orientations: (a) both tags located in the same place; (b) both tags stacked vertically; and (c) tags oriented 90^o with respect to each other. (D denotes the distance between the sensor antenna and the control antenna, G denotes the gap length)

Thus, even though the tags are co-located, a reader can measure the RSSI for each of the tags. For our simulations we have assumed that only one of the tags respond at a time and the effect of the non-responsive tag is to affect the antenna loading characteristics. Fig. 2.6 shows the simulation results for three configurations of tag placements: (a) when both the tags are located on the same plane; (b) when the tags are vertically stacked; and (c) when the tags are oriented 90^o with respect to each other. For all the simulations the distance between the two antennas D and the gap length G were varied along with the conductance of the gap material. In cases (a) and (b) the coupling effect can be clearly seen in the S_{11} plot (inset) which show multiple resonant peaks, peak broadening and a shift in the resonance frequencies. However, if the S_{11} is measured at 915MHz, the response is still monotonic with respect to the conductance of the gap material. However, from a practical point of view configuration (a) and (b) might be problematic because for both cases the reader sensitivity could be significantly reduced due to the degradation in the quality factor. For the configuration shown in (c), both the S_{11} response and the conductance characteristics are minimally affected. Thus, this configuration will be used for our proof-of-concept experiments.

2.4 Proof-of-concept applications

We apply the proposed RFID sensing for two proof-of-concept applications: (a) detection of IgG in a sample; and (b) detection of moisture in a sample. The functionalization and modification of the antenna gap is shown in Fig. 2.7 for both the applications. For all the experiments, commercial passive EPC Gen 2 UHF RFID tags manufactured by Alien Technologies have been used.

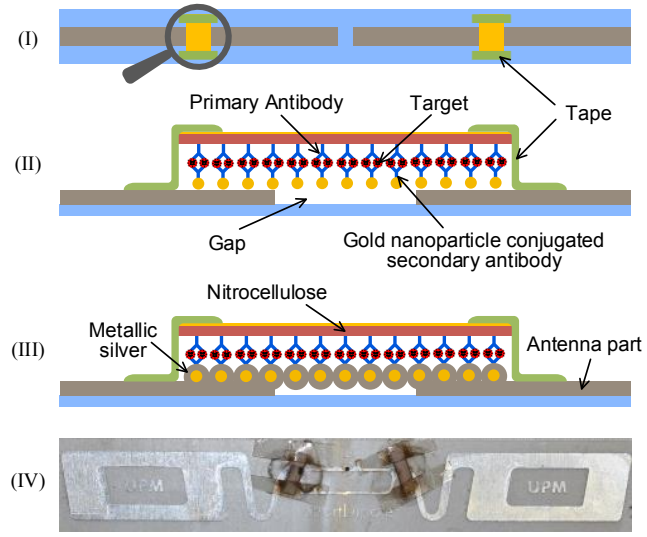

(a) IgG detection

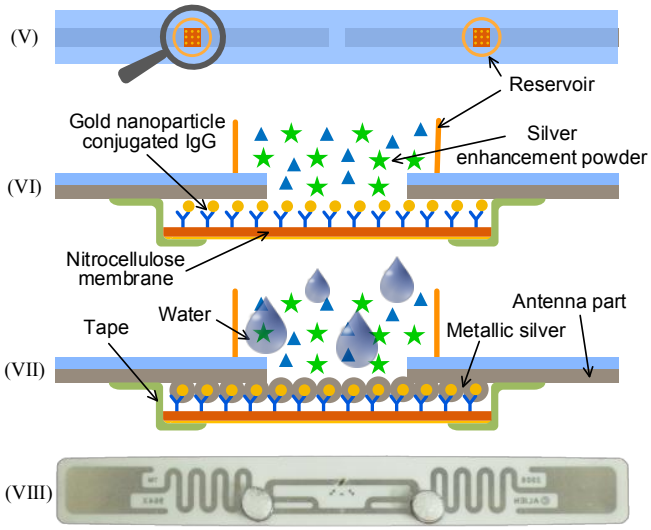

(b) Moisture detection

Figure 2.7: Working principle of the silver-enhancement process for dipole antenna based biosensor and humidity sensor: (a) IgG detection: (I) top view of the biosensor structure with one gap on each side covered with NC membrane; (II) cross-sectional view of the antenna gap with gold nanoparticle conjugated anti-rabbit IgG forming a sandwich structure before silver-enhancement; (III) cross-sectional view after the gap is bridged using silver-enhancement; (IV) top view of 915MHz COTS dipole antenna based RFID biosensor structure. (b) Moisture detection: (V) top view of the biosensor structure with one gap on each side; (VI) cross-sectional view of the antenna gap with gold nanoparticle conjugated anti-rabbit IgG immobilized on NC membrane before silver-enhancement; (VII) cross-sectional view after the gap is bridged after DI water is applied to facilitate the silver-enhancement; (VIII) top view of 915MHz COTS dipole antenna based RFID humidity sensor structure.

2.4.1 IgG detection

Operating principle

The working principle of the proposed RFID biosensor for IgG detection is shown in Fig. 2.7(a). The tag antenna with a gap on each side is first glued to a plastic backing material as shown in Fig. 2.7 (I). The gap is then covered by a nitrocellulose (NC) membrane with the NC side facing the aluminum antenna. Then target specific antibodies (aIgG) are immobilized on the surface of NC membrane. When a solution of the conjugates of the target and the secondary antibody (in this case IgG and gold nanoparticle conjugated anti-IgG (aIgG-AuNP)), IgG-aIgG-AuNP, is applied from the side of the NC membrane, the conjugates move to the surface of NC membrane due to capillary forces. In this regard, the process of conjugation and hybridization with the immobilized antibodies is similar to that of a lateral-flow immunoassay [60] and the details about fabrication of the application pad and the conjugate pad can be found in [89] and has been omitted here for the sake of brevity. Due to antibody-antigen hybridization, a sandwich structure (aIgG-IgG-aIgG-AuNP) is formed and is shown in Fig. 2.7 (II). The excess unbonded sandwich conjugates are washed away from the NC membrane due to capillary force. The remaining aIgG-IgG-aIgG-AuNP conjugates are now detected using the silver-enhancement of the RFID antenna as described in section 2.2.

Materials and methods

Silver Enhancement Kit for Proteins and Nucleic Acids was obtained from Ted Pella (Redding, CA, USA). Anti-Rabbit IgG (whole molecule) conjugated with gold nanoparticles produced in goat (product number: G7402), anti-rabbit IgG antibody produced in goat (product number: R2004) and IgG from rabbit serum (product number: I5006) were purchased from Sigma-Aldrich (St Louis, MO, USA). Glutaraldehyde and Methanol were also obtained from

Sigma- Aldrich (St Louis, MO, USA). Nitrocellulose (NC) membrane with flow rate of 135 sec/4cm was purchased from Millipore (Billerica, MA, USA). Deionized (DI) water used in the experiment was obtained through Millipore water purification systems (Billerica, MA, USA). Passive 915 MHz UHF RFID tags (ALN 9640) were purchased from atlasRFID store (Birmingham, AL, USA). Scanfob Ultra-BB2 Wireless GEN2 UHF RFID Reader/Writer (Cedar Park, TX, USA) was used as detector in the experiment. All experiments were carried out in a certified Biological Safety Level II laboratory.

The NC membrane was cut into small pieces, washed with DI water three times and dried for 30min. Then NC membrane is immersed in 10% (v/v) methanol for 45min and left dry for 30min in air. After that, it is washed with 0.5% (v/v) glutaraldehyde solution and dried in air for 60min. Anti-IgG (R2004, primary antibody used in this experiment) is then applied on NC membrane, which is sealed with parafilm in petri dish and incubated at 37°C for 1 hour. Then NC membrane is washed with DI water for 3 times and air dried for 1h. Until now, the pretreatment of NC membrane is done and ready to use.

Each side of the dipole antenna is cut to form a small gap. The dipole antenna is attached to the plastic substrate with double-sided tape. The NC membranes are then attached to the surface of antenna with tape to cover each of the gaps. Then the conjugates of the target and secondary antibody (IgG-aIgG-AuNP) are applied on two gaps of antenna from the side edges of the NC membranes. The reagent volumes used for different antennas are 2μl, 4μl and 6μl, separately. Then, the dipole antennas are sealed with parafilm in the petri dish and incubated at 37°C for 1 hour. The NC membranes are then washed 3 times with DI water and dried in the drier box. Silver-enhancement solution is prepared by mixing the initiator and enhancer with volume ratio of 1:1. The NC membrane is then immersed in silver-enhancement solution. To facilitate the silver ions reduction, the silver-enhancement reaction is taken place in 37°C for 25min instead of room temperature. After the silver-enhancement process, the

NC membrane is washed with DI water, dried and ready to be read by 915MHz Scanfob Ultra-BB2 reader.

2.4.2 Humidity detection

Principle, materials and methods

The working principle of the RFID biosensor for humidity detection is shown in Fig. 2.7(b). The principle is similar to that of IgG detection and is based on the principle of silver-enhancement technique that can electrically bridge the split RFID dipole antenna parts. However, the difference is that the silver-enhancement solution is applied in a dried form. Silver-enhancement kit was purchased from the vendor in two separate forms (named as initiator and enhancer) and in liquid forms. The initiator and enhancer were dried and crystallized separately in a dark environment. The procedure of the NC membrane treatment is similar to that of the procedure described in the previous section. The NC membrane is also cut into small pieces, washed with DI water three times and dried. It is then treated 10% (v/v) methanol for 45 min and dried for 30min. 0.5% (v/v) glutaraldehyde solution is used to treat NC membrane, which is dried in air for 60 min. The difference from the procedure described for IgG detection is that the gold nanoparticle conjugated anti-IgG (aIgG-AuNP) is now immobilized on the NC membrane. aIgG-AuNP is applied on NC membrane, which is sealed with parafilm in petri dish and incubated at 37°C for 1 hour. Then it is washed with DI water and dried for 1h.

Each side of the RFID dipole antenna (ALN-9640) is cut to form a small electrically insulated gap of dimensions 0.4mm. The pretreated NC membranes are glued to the surface of antenna with tape. Two gaps of the dipole antenna are covered by aIgG-AuNP immobilized NC membranes with nitrocellulose side facing the aluminum antenna. On the other side of the

RFID dipole antenna (plastic substrate side of the RFID antenna), a reservoir is affixed right on each gap with J-B KwikWeld super glue, shown in Fig. 2.7 (V) and (VI). The reservoir here works as a container for the storage of silver-enhancement powder. After 4 hours' super glue curing time, the powder of silver enhancer (with ratio of initiator and enhancer of 1:1) is filled into the reservoir. The basic humidity sensor's operation principle is similar to that of the biosensor described previously in this paper. When the humidity sensor is exposed to the water, the dry silver-enhancement powder gets dissolved and liquid silver-enhancement solution is regenerated. As the silver-enhancement solution diffuses through the NC membrane silver ions are reduced into metallic silver on the surface of gold nanoparticles. Similar to the self-assembly principle described in section 2.2, the reduced silver electrically bridges the antenna gap, as shown in Fig. 2.7 (VII).

2.5 Measurement results

The complete schematic RFID based detection and measurement system is shown in Fig. 2.1. The system includes a 915 MHz RFID writer/reader (Scanfob Ultra-BB2) which can interfaces with a laptop with cable or smart phone via bluetooth connection for data analysis and display. The formation of micro-antennas in the gap can effectively bridge the two split dipole antenna parts, which modulates the length of the dipole antenna. As a result, different concentration of target analytes can be quantified based on the RFID interrogation distance under the same power emitted from the RFID writer/reader. An unmodified 915 MHz dipole antenna (same structure as our experimental implemented biosensor dipole but without any treatment) is interrogated by the RFID writer/reader as a calibration source. Note that this procedure of using an COTS RFID reader is more practical for use in the field rather than probing the feed-points of the antenna and measuring its effective S_{11}. Also, the antenna is loaded by the tag's chipset (which is an active element) and therefore using a network

analyzer to measure S_{11} may not serve as an accurate indicator of the power reflected by the tag. The farthest distances of the biosensor and the calibration tag that can be interrogated by RFID reader are denoted as L_1 and L_2, respectively. All the measured maximum detection distances of the biosensor (L_1) are normalized with regards to that of the calibration dipole antenna (L_2).

2.5.1 IgG detection results

Fig. 2.8(a) shows the normalized detection length of dipole antenna biosensor when different amount of IgG-aIgG-AuNP conjugates (ranging from 0μl to 6μl) are used. For the biosensor when no IgG-aIgG-AuNP conjugates are applied (equivalent to the situation that no target analyte is detected), the normalized detection length is only around 12% to that of the calibration dipole antenna. When each side of the antenna is cut to form a small gap, the input impedance of it is changed, which causes the RFID tag operating with lower efficiency. Under the same power emitted from the RFID writer, it can only be sensed in a much shorter distance compared to the original unmodified dipole antenna. For dipole antenna with certain amount of IgG-aIgG-AuNP conjugates applied, both the controlled (without silver-enhancement) and the experimental (with silver-enhancement) were run. The measured results are monotonic with respect to the different volumes of IgG-aIgG-AuNP conjugates applied, shown in Fig. 2.8(a). In this proof-of-concept study, a minimum amount of target analytes which can be differentiated from the control experiment was 26.9ng. The signal-to-noise threshold levels pre-programmed on the COTS RFID reader determines this lower-limit of detection for this study. When the gap of the dipole antenna is completely electrically bridged by the micro-antennas, the RFID antenna's reflection properties is mainly determined by the host dipole structure. The detection length of the biosensor gets saturated in the range between 64% to 77% when a high target concentration (53.8ng in this paper)

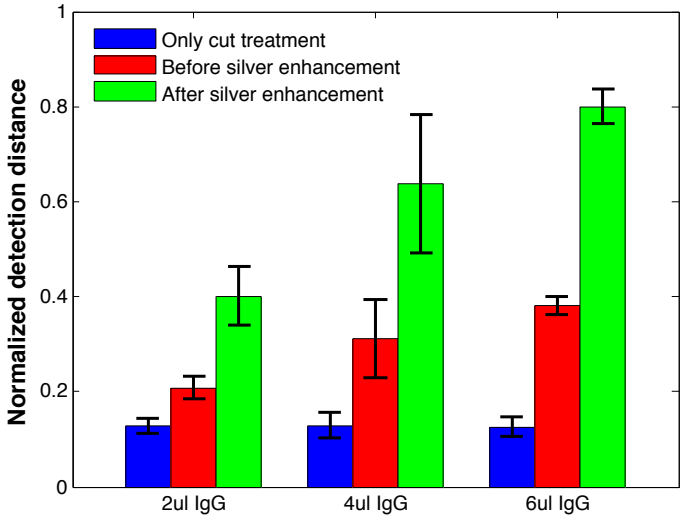

(a)

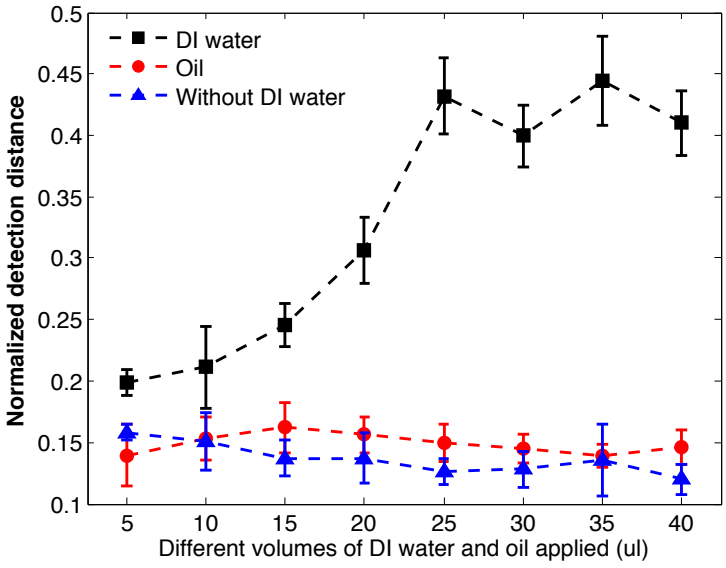

(b)

Figure 2.8: (a) Normalized maximum detection length of dipole antenna biosensors with regard to that of the calibration antenna when different volumes of IgG are applied; (b)Normalized maximum detection length of dipole antenna humidity sensor with regard to that of the calibration antenna when different volumes of DI water and oil are applied.

is applied. Even if more target conjugates are applied to the biosensor, it will not improve the bridging quality (impedance matching) and also will not contribute to the increase of detection length.

2.5.2 Humidity detection results

Fig. 2.8(b) shows the normalized maximum detection range when different volumes of DI water (ranging from 5μl to 40μl) are applied. There is an obvious increase in the detection length when water is applied to the humidity sensor compared to that without DI water applied. For the dipole antenna without the presence of DI water, the maximum normalized detection length is around 12% to 15% with respect to that of the calibration antenna. The minimum amount of DI water applied to the humidity sensor in this experiment is 5μl and the detection range increased to 19.89% of that of the calibration antenna which is nearly doubled compared with the detection length without DI water applied. It indicates that the gap between the separated antenna parts starts to be bridged by the silver-enhancement.

The measured detection range shows a nearly monotonic relationship with respect to the volume of DI water. The detection length of the humidity sensor stops to monotonously increase when the volume of applied DI water reaches 25μl and keeps stable at the value between 40% and 45%. It is because silver-enhancement process has completely bridged the gaps of the dipole antenna and the response of the RFID tag is mainly determined by the host dipole structure. Vegetable oil (with volumes ranging from 5μl to 40μl) is applied to the humidity sensor as control experiment. Fig. 2.8(b) shows that normalized detection range does not vary much (at a value between 13% and 16%) when different volumes of vegetable oil is applied. The measurements show that the applied vegetable oil will not contribute to the increase of the humidity sensor's detection length since it cannot facilitate the silver deposition which modifies the input impedance of the RFID dipole antenna.

2.6 Summary and discussion

In this chapter we presented a novel approach for designing RFID based biosensors which used self-assembly of the tag antenna using a silver-enhancement technique. The silver-enhancement approach self-assembles a chain of micro-antennas (gold nanoparticle cored silver shelled particles) based on target analytes. The growth of these micro-antennas changes the input impedance of the RFID dipole antenna which ultimately modifies the reflection properties of the RFID tag. The change in reflection properties can be detected and measured using a COTS RFID reader. In this chapter, we have also proposed a ratiometric approach for robust measurement of the reflected signal strength. The optimal configuration uses two co-located tags that are oriented 90^o with respect to each other and minimizes mutual antenna loading. The approach has been applied and demonstrated for two proof-of-concept applications: (a) detection of IgG in a sample; and (b) detection of humidity in a sample. The measured results show that the ratiometric measurement can not only be used to detect target analytes but also to measure their concentration levels within a certain range. The challenge for the proposed sensor and will form part of the future research is the integration of sample acquisition interface (like microfluidics or lateral-flow structures) with the product package being monitored. The future work will also explore the end to end multi-physics simulation of the proposed concept that combines the physics of analyte-receptor interactions with the physics of silver-enhancement and the physics of antenna propagation.

Chapter 3

Wireless Biosensing by Self-assembling QR codes

This chapter extends our previous work on silver enhancement based self-assembling structures for designing reliable, self-powered biosensors with forward error correcting (FEC) capability. At the core of the proposed approach is to self-assemble an invalid quick response (QR) code into a valid QR code that can be optically scanned using a smart-phone in the presence of target analyte based on silver enhancement. The scanned information is first decoded to obtain the location of a web-server which further processes the self-assembled QR image to determine the concentration of target analytes. To choose an appropriate paper substrate to print and self-assemble the QR code, we have explored four different substrates that includes regular printing paper, Whatman filter paper, nitrocellulose membrane and lab synthesized bacterial cellulose. We report that out of the four substrates bacterial cellulose outperforms the others in terms of probe (gold nanorods) and ink retention capability. The patterning of the QR code on the substrate has been achieved using a combination of low-cost ink-jet

printing and a regular ballpoint dispensing pen. In this chapter the proof-of-concept detection using prototypes of QR encoded FEC biosensors has been demonstrated.

3.1 Introduction

The last decade has seen significant proliferation of smart-phones into the consumer market and across different parts of the world [26]. Not only are these mobile devices equipped with multi-modal communication (voice and data) capabilities, they are also equipped with different sensing capabilities as well. For instance, by using the images acquired from phone's integrated camera and by applying different image processing algorithms, the smart-phone can be used for different optical sensing applications ranging from mobile microscopes [51, 81], heart-rate monitors [29, 47] and environmental sensing [5, 79].

Another application of optical sensing that is the use of smart-phones to scan quick-response (QR) codes as shown in Fig. 3.1. A QR code for instance could encode the location of a web-server from which the product specific information (e.g. active ingredients, side-effects and consumer ratings) could be retrieved. In the area of biosensors, QR codes have been mainly used to encode product information. For instance, in [77] Kubota used a QR code to describe the specifications of an electrochemical paper-based p-nitrophenol biosensor. Similarly, in [22] QR code was used to encode platform and patient information on a lateral flow immunochromatographic sensor for detecting human immunodeficiency virus (HIV) and measuring prostate-specific antigen (PSA). In this case a Google glass was used to scan the code and retrieve the data from the cloud server. In [67] Zharnikov reported a method to pattern a 29×29 QR code using nanoparticles transferred using an ultra-thin hydrogel template. However, the patterning technique was not integrated with the underlying process of biosensing.

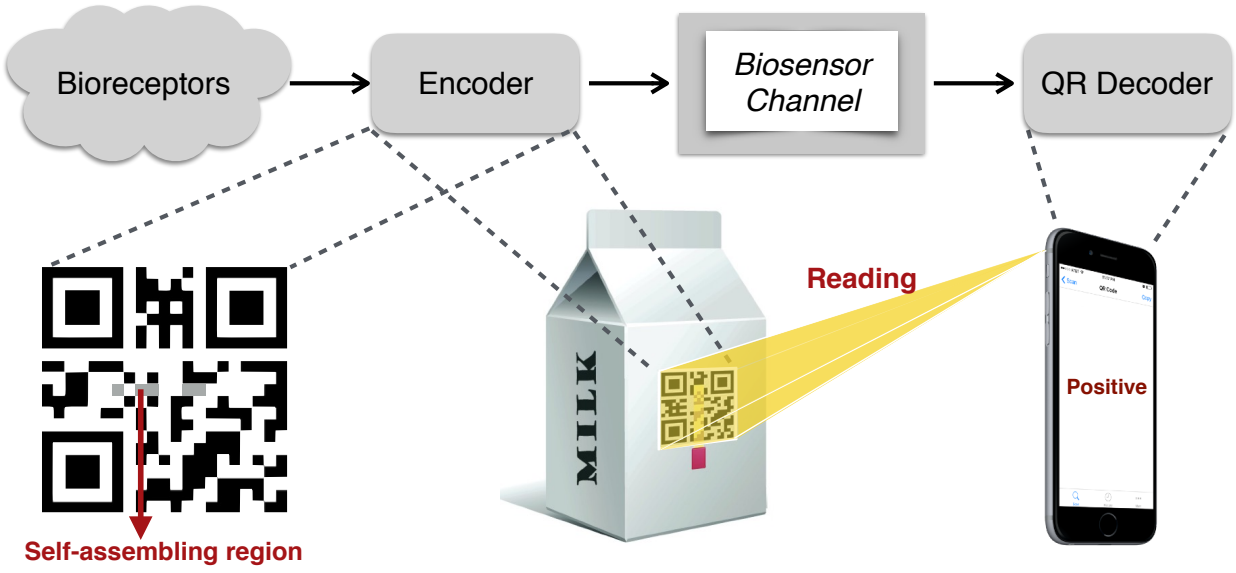

Figure 3.1: Framework of a forward error-correcting biosensor specific to the proposed self-assembled QR code. A smart-phone is used for scanning and decoding the code and determining the presence or absence of target contaminants.

However, if the information encoded by a QR code could also reflect the concentration levels of target analytes in a product, then by using a smart-phone the consumer could determine the freshness of a perishable product like milk (as shown in Fig. 3.1) before purchase. This ability could therefore be useful for preventing food-borne disease outbreaks and product recalls like the 2015 Listeria outbreak due to contaminated ice-cream [68]. The QR code also provides a platform to integrate the concept of forward error-correcting biosensors [59] where the process of biosensing could be combined with error-correcting codes to achieve a higher reliability and throughput in analyte detection. In this FEC framework the biosensor is modeled as a communication channel where the conversion of the binding event between the analyte with its biological receptor (e.g. antibody or aptamer) is considered to be noisy [43]. Therefore, by using a channel encoder comprising of different spatial and logical bioreceptor patterns [43], the effects of channel noise could be potentially mitigated. As an example,

a low-density parity check type encoder constructed using antibody based logic gates was reported in [31].

For this work, we propose the QR code as a bio-encoder, as shown in Fig. 3.2, and the smart-phone as the decoder or measurement device. The QR bio-encoder is constructed by overlaying an unassembled QR code over a paper-based microfluidics assay that samples and directs the analyte into regions of the QR code that could self-assemble. In this work self-assembly is achieved using a silver-enhancement process which is triggered only when target analytes are present in the sample, which results in the change in optical absorption in specific regions of the QR code. This chapter builds upon our previous work in the area of silver-enhancement [61, 62, 97, 98, 100, 102] where we had demonstrated self-assembly of radio-frequency (RF) antenna structures and for implementing conductance based biosensors. In these previous studies, silver-enhancement procedure was used to amplify and measure the concentration of gold-nanoparticles which was shown to be equivalent to measuring the concentration levels of the target analytes. In this chapter we show that the QR decoding process can also measure the concentration levels of immobilized gold-nanoparticles with the assumption (based on our prior work) that this ability can easily translate to measuring the concentration levels of target analytes as well.

This chapter is organized as follows: Section 3.2 briefly introduces the basics of a QR code and self-assembly sensing principle using QR code. Materials and methods used to prepare the biosensor and the experimental setup have been introduced in Section 3.3. Four different substrates, including regular printing paper, Whatman filter paper, nitrocellulose membrane and lab synthesized bacterial cellulose, are used for the QR code biosensor prototype fabrication. Section 3.4 presents measurements obtained using the fabricated biosensor prototypes, and Section 3.5 concludes the chapter with discussions of future work.

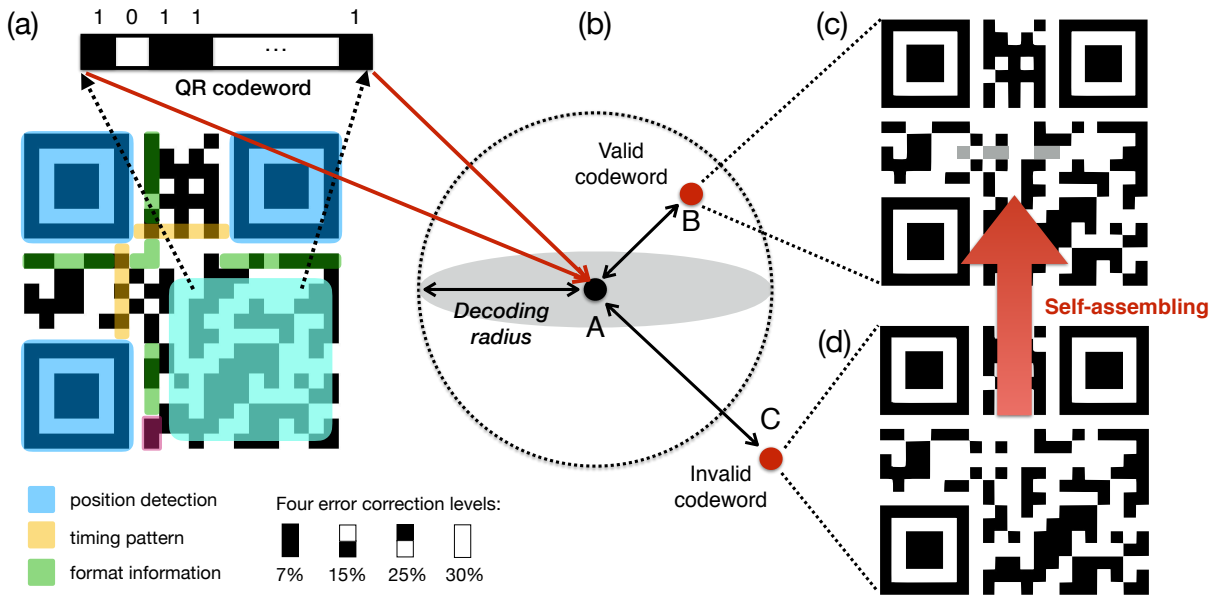

Figure 3.2: Principle of the proposed QR code self-assembly and decoding process: (a) different parts of a QR code; (b) decoding procedure where any assembled QR is successfully decoded if the code-word lies within the decoding radius; and examples of a QR code that can be (c) successfully decoded; and (d) cannot be decoded.

3.2 Principle of operation

3.2.1 Operating principle of QR code biosensor

QR code is a two-dimensional barcode which was developed to enhance the data encoding capacity per unit area compared to a traditional barcode [32]. Since its inception for use in tracking automobile parts, QR codes have now been widely adopted in commercial tracking, entertainment, ticketing and labeling applications. While several references can be found in literature describing the theory and decoding of QR codes [11, 44, 83, 91], for the sake of completeness we briefly describe the structure of the code without too much emphasis on different variants and versions of the code. Typically, four kinds of data, namely numeric, alphanumeric, byte/binary, and kanji, can be encoded and stored in the QR code.

As an example, Fig. 3.2(a) shows a version 1 (21×21 pixels) QR code encoding the word "POSITIVE". The reader can readily verify this by using the QR decoder app on their smart-phone. The position detection pattern (highlighted by a blue square in Fig. 3.2(a)) located at the three of the four corners are used for alignment, such that a QR code scanner can normalize and calibrate for any image scaling or misalignment. Format information (shown in Fig. 3.2(a)) contains the error correction rate and mask pattern of a QR code. This information is read first to determine the "strength of error-correction" before the code is decoded. The timing pattern helps the decoder to detect the position of each cell in the QR code. Data encoding and decoding use a Reed-Solomon error correction algorithm that can correct for corruption in parts of the scanned QR code. Like any FEC code, a QR code can embody different strengths of error correction (Low-7%, Medium-15%, Quartile-25% and High-30%) by trading-off data storage capacity. For example, in Fig. 3.2(a) the area marked in yellow encodes the error correction level "L", which implies that the code can be reliably decoded even if approximately 7% of the data is corrupted or damaged. We will exploit this error-correcting capability in the proposed FEC biosensor where parts of the QR code-word will self-assemble and become decodable based on the presence of target analytes in the sample.

This FEC process illustrated in Fig. 3.2 where a valid QR image (image that can be successfully decoded) is visualized as a vector (A) in a high-dimensional space (illustrated in three dimensions in Fig. 3.2(b)). The decoding radius in Fig. 3.2(b) quantifies the error-correcting capability of the QR code. Any vector that differs from the valid QR code (A) by a certain degree (for instance Hamming distance or Euclidean distance) but lies within the hyper-sphere can be successfully decoded and any vector that lies outside cannot be decoded. This is illustrated in Fig. 3.2 which shows two examples of assembled QR codes (B and C) that differ from each other regions that is highlighted. The QR code B lies within

the decoding radius and can therefore be successfully decoded whereas the code-word C lies outside the radius and hence cannot be decoded. In the proposed FEC biosensor, the sensing process (or the process of growing or assembling the QR code) follows a trajectory starting from an unassembled QR codeword like C to an assembled codeword like B, if and only if target analytes are present. Also illustrated in Fig. 3.2 is that the decoding distance between the assembled QR codeword and the perfect QR codeword can be used to determine the concentration of the target analyte.

3.2.2 Self-assembly and analyte detection based on silver enhancement

Silver-enhancement based analyte detection relies on the formation of a sandwich structure comprising of primary probes (e.g. antibodies), target and gold nanorod (AuNR) conjugated secondary probe, as illustrated in Fig. 3.3(a). In our previous work [61, 62] we have described the mechanism of the sandwich formation for different substrates and for detecting different target analytes which we briefly summarize in this section. The AuNR conjugated secondary probes first hybridize with their target analytes which then bind with the primary probes that are immobilized on specific locations on a substrate (e.g. silicon or nitrocellulose paper). Any unbounded secondary probes are washed away leaving the sandwich structure (labeled by AuNR) intact. Because the dimensions of AuNRs are in a scale of nanometers, they are not large enough to be optically visible or electrically detectable. Therefore, in literature a silver-enhancement procedure is used to stain the gold labels (nanoparticles or nanorods) and measure its concentration [24, 73].

When a silver enhancement solution (comprising of silver ions (Ag^+) and hydroquinone, a photographic developing solution) is applied, silver ions start reducing into metallic silver on

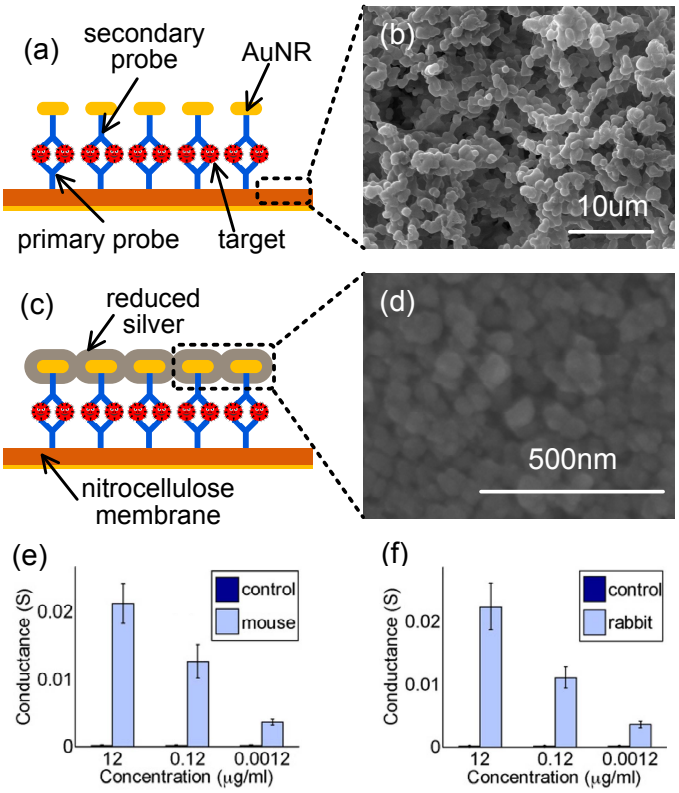

Figure 3.3: Analyte detection using silver-enhancement: (a) sandwich structure labeled using AuNR and before the process of silver-enhancement; (b) SEM image of nitrocellulose membrane surface; (c) after the silver-enhancement process, the silver ions reduces on the AuNR; (d) SEM image showing silver ions were reduced on the surface of AuNRs and grow the particle in size with silver-enhancement; (e) and (f) summarize previous experimental results showing that the growth of silver-particles leads to a change in conductance which is proportional to the concentration level of mouse and rabbit IgG [61].

the surface of the gold. This process is completely self-powered by the chemical activation energy and does not require any external biasing. Also, during this process, gold serves as a catalyst and facilitate further reduction of silver-ions. As time progresses, more silver ions are reduced and a chain of AuNRs cored silver micro-structures assemble, as shown in Fig. 3.3(c). This results in an equivalent increase in conductance (as shown in Fig. 3.3(e) and (f)) which can be measured to determine the concentration of the captured targets. In [97, 102], we have used the silver-enhancement principle to grow radio-frequency antennas in different antenna patterns. In this work we use the silver-enhancement principle to grow parts of a QR code that can be optically scanned. When sufficient silver enhancement solution is present, the increase of the particle size is monotonic [62] with respect to the time, which reduces the intensity of the scattered light. Thus, the regions where the silver-enhancement successfully occurs become darker. Note that besides silver enhancement, gold solution can also be reduced and deposited on the gold nanorod surface, and works in a similar way as the process of silver-enhancement. However, the time-scale for gold-enhancement is much longer than silver-enhancement, the relative change in intensity is much lower and the cost of using gold as an enhancer is much higher than silver.

To understand how the silver-enhancement can be combined with a QR code, consider the modified QR code shown in Fig. 3.2(c) which is the same QR code as the one shown in Fig.3.2(a). The only difference is that five black squares have been reduced in intensity to gray. This simulates the condition when different concentrations of analytes lead to different degrees of staining. The code in Fig. 3.2(c) can still be decoded (in this case with WeChat App on iPhone 6) and the reader can verify this using his/her smart-phone. However, when these five black modules/squares are completely removed from the code , as shown in Fig. 3.2(d), the code can not be decoded by a smart-phone because the code-word lies outside the decoding radius, as shown in Fig. 3.2(b).

(a) (b) (c) (d)

Figure 3.4: Experiment showing different stages of QR self-assembly: (a) an example of QR code printed on a white paper (information encoded in this QR code: Adaptive Integrated Microsystems Laboratory http://aimlab.seas.wustl.edu/); (b) the same QR code printed on a plastic substrate using AuNR ink; (c) the plastic substrate after 20 min of silver-enhancement; and (d) information in the QR code decoded with a smart-phone app.

3.2.3 Developing ink-jet printed QR code with silver enhancement

We verified the process of encoding and decoding QR codes self-assembled using the silver-enhancement process in the following experiment. QR code in Fig. 3.4(a) was ink-jet printed on the mesoporous polyethylene substrate using AuNR solution as ink and was developed with silver enhancement solution, as shown in Fig. 3.4. Before loading the cartridge filled with the AuNR solution to print the QR code, the printer head was purged by printing the MIS purge document using aqueous inkjet vehicle. Around 10-20 pages were printed by selecting "Heavyweight Matte paper" and "Best Photo" in the printer preferences until pigment disappeared. Then the cartridge filled with AuNR solution was loaded. Another 5 pages (or more) of the MIS purge document were printed on Heavyweight Matte paper and Best Photo using AuNR ink until the ink appeared consistent. Then the mesoporous substrate was loaded and the QR code was printed. After the QR code printed on the substrate dries up, the code is not visible as shown in Fig. 3.4(b). This is because the size of the AuNR is in nanometer. The mesoporous substrate was then treated with silver

enhancement solution (composing of the initiator and enhancer with volume ratio of 1:1). After a 20 min development process, more and more silver ions get reduced on the surface of AuNR. The size of the particle gets increased from nanometer scale to micrometer scale. The area on the substrate where is originally printed with AuNR can be visually seen in black, as shown in Fig. 3.4(c). Then the substrate was rinsed with DI water gently to remove the remaining silver enhancement solution and stop the process of silver enhancement. The developed code can then be decoded with QR code scanner, as illustrated in Fig. 3.4(d). It should be noted in Fig. 3.4(c) that the area where no AuNR is printed gets darker after silver enhancement compared to that in Fig. 3.4(b). It is because the AuNR solution printed on the mesoporous is not firmly captured by the substrate. Once the substrate is treated with silver enhancement solution for development, some of those AuNRs are washed away from their original spots and are captured again in other spots by the substrate. These AuNRs also participate in the silver enhancement process since they are also exposed to the solution, which turns the substrate darker. Fortunately, due to the error-correcting capability (15% of codewords can be restored in this case), the QR code can still be correctly decoded.

3.3 QR code biosensor prototype on different substrates

Whitman filter-paper [19, 66] or nitrocellulose [13, 14] have been extensively used as paper substrates for biosensors in the literatures. In this work we have explored the use of bacterial cellulose (BC) as the substrate to fabricate the QR code biosensor. BC is a biocompatible and bioactive material that has been approved by the US Food and Drug Administration (FDA) for the usage in clinical indications [1]. As a substrate BC is attractive due to its open nanoporous structure, simple surface chemistry, excellent mechanical properties, low cost and scalable synthesis [45, 92]. Even under vigorous mechanical agitation and harsh chemical conditions, bacterial cellulose still exhibits excellent stability. These features of BC

have been previously used for designing flexible Surface Enhanced Raman Scattering (SERS) substrate which shows ideal capabilities for bacteria collection [86]. In this chapter, we show that BC also demonstrate excellent ink retention capability that ensures the printed QR code is stable when subjected to liquid analytes.

3.3.1 Materials and methods

Materials and apparatus

Gold chloride ($HAuCl_4$), Hexadecyltrimethylammonium bromide (CTAB), sodium borohydride ($NaBH_4$), silver nitrate ($AgNO_3$), ascorbic acid and silver enhancement kit were purchased from Sigma-Aldrich (St. Louis, MO, USA). Nitrocellulose (NC) membranes with flow-time (measure of flow rate) of 135sec/4cm was purchased from Millipore (Billerica, MA, USA). Deionized (DI) water used in the experiment was obtained through Millipore water purification systems (Billerica, MA, USA). An EPSON stylus C88+ ink-jet printer was used to print the QR code. The printing substrate, aqueous inkjet vehicle, the empty cartridge and aqueous inkjet vehicle were purchased from Novacentrix (Austin, TX, USA). Paper mate profile retractable ballpoint pens were bought from Amazon.com, Inc. All the chemicals were used as received without further purification. The experiments were carried out in a certified Biological Safety Level II laboratory.

Synthesis of AuNRs

AuNRs were synthesized by using seed-mediated method [27, 37]. Seed solution was synthesized by adding 0.6 ml of an ice-cold $NaBH_4$ (10 mM) solution into 10 ml of $HAuCl_4$ (0.25 mM) and CTAB (0.1 M) solution under vigorous stirring at room temperature. The color of the seed solution changed from yellow to brown. Growth solution was prepared by mixing 5

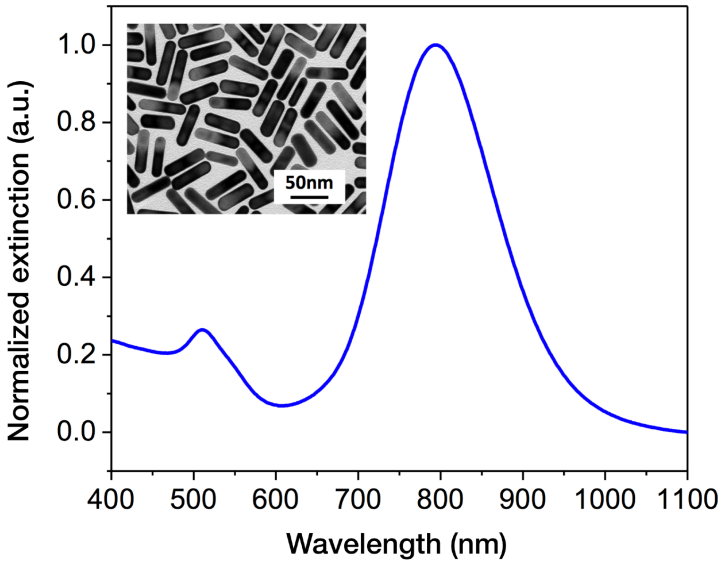

Figure 3.5: Optical extinction spectrum of AuNR verifying the dimensions of the nanorods (inset: TEM image of AuNR).

ml $HAuCl_4$ (10 mM), 95 ml CTAB (0.1 M), 1 ml $AgNO_3$ (10 mM) and 0.55 ml ascorbic acid (0.1 M), consecutively. The solution was homogenized by gentle shaking. To the resulting colorless solution, 0.12 ml of freshly prepared seed solution was added and kept undisturbed in the dark for 14h. Prior to use, the AuNR solution was centrifuged twice at 8000 rpm for 10 min to remove excess CTAB and re-dispersed in DI water. UV-Vis extinction spectrum was measured using Shimadzu UV-1800 UV-Vis spectrophotometer and shown in Fig. 3.5. The extinction spectrum of AuNR exhibits two characteristic bands at 510 nm and 794 nm, which corresponding to the transverse and longitudinal plasmon resonances, respectively. The length and diameter of AuNR were respectively measured to be 58.7±4.5 nm and 14.5±1.0 nm using Transmission electron microscopy (TEM) (inset in Fig. 3.5). TEM image was collected using a JEOL JEM-2100F field emission microscopy.

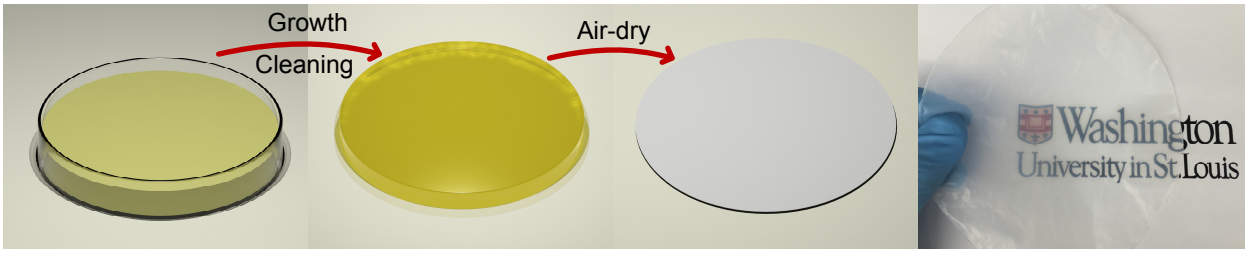

(a) Bacteria in broth (b) BC hydrogel (c) BC paper (d) BC paper photo

Figure 3.6: Schematic illustration bacterial cellulose growth process: (a)-(c) schematic illustration showing bacterial paper synthesis process; (d) photo of synthesized bacterial cellulose.

Synthesis of bacterial cellulose

Fig. 3.6 shows the schematic illustration of bacterial cellulose fabrication process. *Gluconacetobacter hansenii* (ATCC 53582) was cultured in test tubes containing 16 ml of #1765 medium at 30°C under shaking at 250 rpm. The #1765 medium is composed of 2 % (w/v) glucose, 0.5 % (w/v) yeast extract, 0.5 % (w/v) peptone, 0.27 % (w/v) disodium phosphate, and 0.5 % (w/v) citric acid. Bacterial culture solution (incubated 3 days) was added to the medium to make a total 7 ml solution. The solution was subsequently transferred to petri dish and incubated at room temperature without disturbance as shown in Fig. 3.6(a). After 5 days, a thin film of bacterial cellulose was formed. For purification, the film was harvested from the petri dish and washed in a 500 ml of 0.1 M NaOH aqueous solution under boiling condition for 2 h. The obtained bacterial cellulose hydrogel (schematic illustrated in Fig. 3.6(b)) was then dialyzed in DI water for 2 days. The purified bacterial cellulose hydrogel was then air dried. Photo of the as synthesized bacterial cellulose is shown in Fig. 3.6(d).

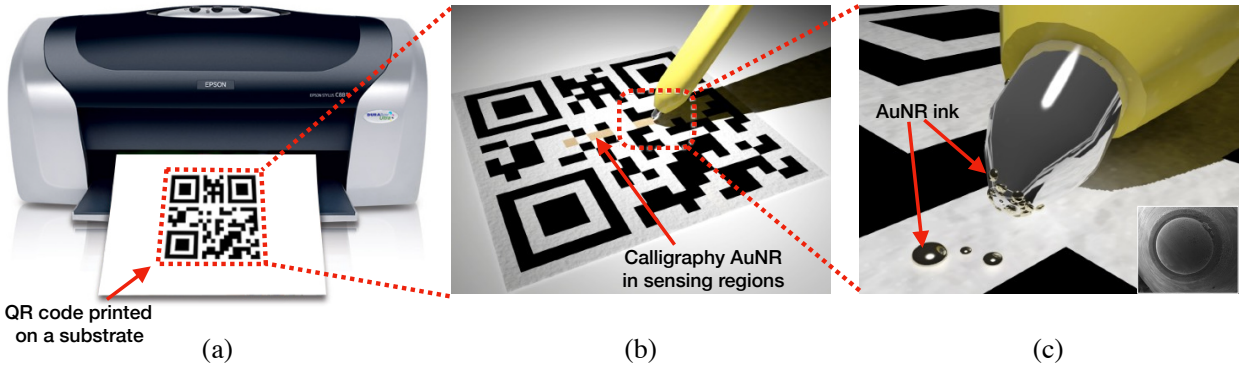

Figure 3.7: Schematic illustration showing QR code biosensor fabrication procedure: (a) print the predefined QR code (invalid) on the substrate with normal black ink; (b) AuNR ink filled in the gel pen and dispensed on the self-assembling region; (c) schematic diagram showing AuNR ink drops on the pen tip surface (inset: SEM image of top view of the pen tip).

3.3.2 QR biosensor prototype fabrication

The invalid or unassembled QR code is firstly printed on the substrate using EPSON C88+ printer with normal black ink, as shown in Fig. 3.7(a). We have used four different substrates in this paper, including regular printing paper, Whatman filter paper, nitrocellulose membrane and lab synthesized bacterial cellulose. Once the printed QR code patterns are dried, AuNR ink is dispensed in the self-assembling regions where the five black modules have been intentionally removed (Fig. 3.7(b)). To dispense the AuNR ink in the self-assembling region more efficiently, ink-jet printing technique has been tried and reported in our previous work [105]. Unfortunately, it's found that direct dispensing of AuNR ink in the enhancement regions is not consistent for different concentration levels due to the physical properties of the AuNR ink (e.g. viscosity, surface tension) is not optimized for EPSON C88+ printer.

In this work, we resorted to a low cost calligraphy method using a regular gel pen to dispense the AuNR ink on the QR assembly regions directly, as shown in Fig. 3.7(b). Similar procedure using a regular ballpoint pen to dispense AuNR solution was reported in our previous work [87,

88]. The original ink in the pen's refill container is pushed out using nitrogen gun after the tip and refill are separated. The gel pen refill and the tip are cleaned with ethanol by sonication for 2 days in a centrifuge tube. The ethanol is replaced every 3 hours until the color of ethanol doesn't change (no more ink gets dissolved in ethanol). Both the pen's refill container and the pen tip are dried with nitrogen gun. The AuNR solution is then injected into the cleaned gel pen refill and the pen is ready to dispense the AuNR ink solution in the QR assembling regions (Fig. 3.7(b) and (c)). Inset shows the top view of the pen tip.

3.4 Measurement results

3.4.1 Silver enhancement on different paper substrates

We have compared the process of self-assembly by calligraphing text (in this case"AIM LAB") with AuNR ink and developing it using silver enhancement technique on different substrates in the following experiment. Four different substrate materials – printing paper, Whatman filter paper, nitrocellulose membrane and bacterial cellulose – have been used and compared in this experiment. Same text has been patterned on these four substrates with AuNR at same concentration level and developed with silver enhancement solution as time progresses, as shown in Fig. 3.8. Before silver enhancement, text on four different samples are nearly invisible (Fig. 3.8 (a1), (b1), (c1) and (d1)) because AuNRs are in a dimension scale of nanometers and are too small to be visibly observed. After silver enhancement the printing paper substrate turns into dark quickly in 4 minutes, which makes the text unrecognizable, as shown in Fig. 3.8(a3). It is mainly because the chemical reagents contained in printer paper binder also facilitate silver reduction.

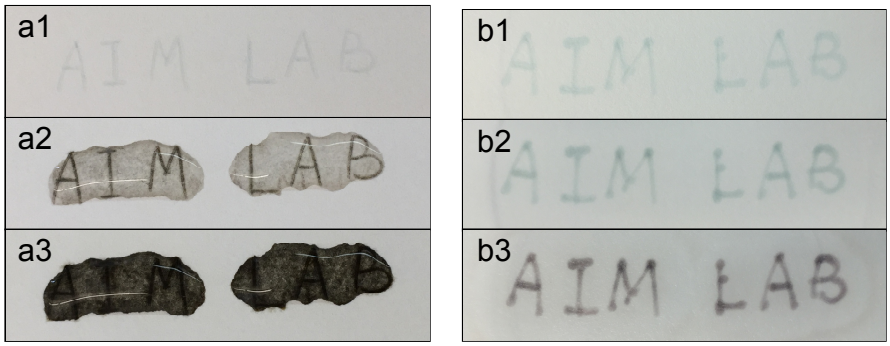

(a) printing paper (b) filter paper

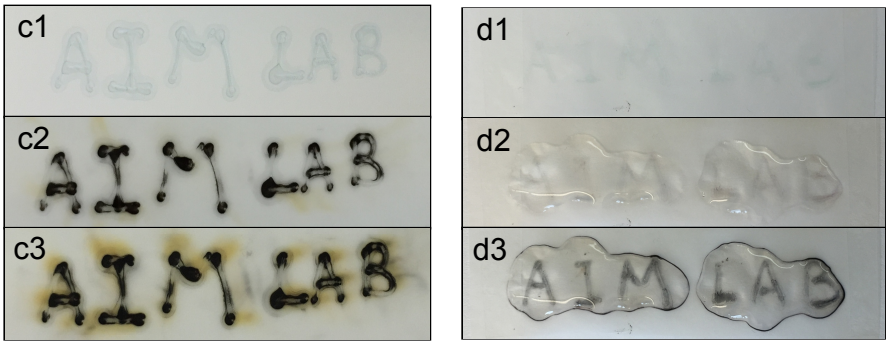

(c) NC membrane (d) bacterial cellulose

Figure 3.8: Text calligraphed on four different substrates using AuNRs ink and developed with silver enhancement: (a1)-(a3) regular printing paper, before SE, 2min and 4 min after SE, separately; (b1)-(b3) Whatman filter paper, before SE, 2min and 7min after SE; (c1)-(c3) nitrocellulose membrane, before SE, 2min and 7min after SE; (d1)-(d3) bacterial cellulose, before SE, 2min and 7min after SE.

Better results have been obtained on the other three substrates due to much less self-contained impurities. For instance, Whatman filter paper is only comprised of super-refined cellulose fibers. Calligraphed text on this substrate is legible after 7 minutes' silver enhancement (Fig. 3.8(b3)). However, during this process the applied silver enhancement solution spreads out and evaporates very quickly due to porous surface feature of filter paper. As a result, continuously adding silver enhancement solution on the filter paper is necessary to provide sufficient reagent to facilitate further silver deposition.

Similarly, nitrocellulose membrane is also highly porous (pore size in micrometers). As a result, continuously applying silver enhancement solution on the calligraphed text is necessary to promote further silver reduction. Although the text is legible after 7 minutes' silver enhancement on nitrocellulose membrane, part of the AuNRs are dispersed away from their original spots by the applied silver enhancement solution and they have also undergone silver enhancement process. As a result, the color of the adjacent area of the text becomes blotted and reduces the legibility of the text.

AuNR text on bacterial cellulose substrate is developed and remain clear and legible after 7 minutes' silver enhancement. Different from above mentioned substrates, bacterial cellulose could retain silver enhancement solution in the spot where it is originally applied since it is has a much smaller pore size (in nanometer scale). One time silver enhancement application is sufficient to develop the calligraphed text on the substrate. Note that there is a noticeable black line surrounding the silver enhancement solution drop after 7 minutes' development as shown in Fig. 3.8(d3) which is known as "coffee ring effect" [18, 35, 106]. Because of different evaporation rates across the silver enhancement solution drop, solution evaporated on the edge is replenished by the liquid from the interior. In this way, some AuNRs dispensed on the surface of the bacterial cellulose that are not firmly captured by the substrate surface are dispersed to the edge. In the meantime, these AuNRs are also exposed to the silver enhancement solution, and have undergone silver enhancement process.

The AuNRs retention capabilities of four different substrates have also been examined. The substrates are first immersed in the AuNRs solution with same concentration over night. Then they are gently rinsed with DI water and air dried. Surface morphologies before and after silver enhancement have been compared with SEM examination for different substrates, as shown in Fig. 3.9. AuNRs can be uniformly captured on the surface of Whatman filter paper, nitrocellulose and bacterial cellulose. With silver enhancement, metallic silver clusters

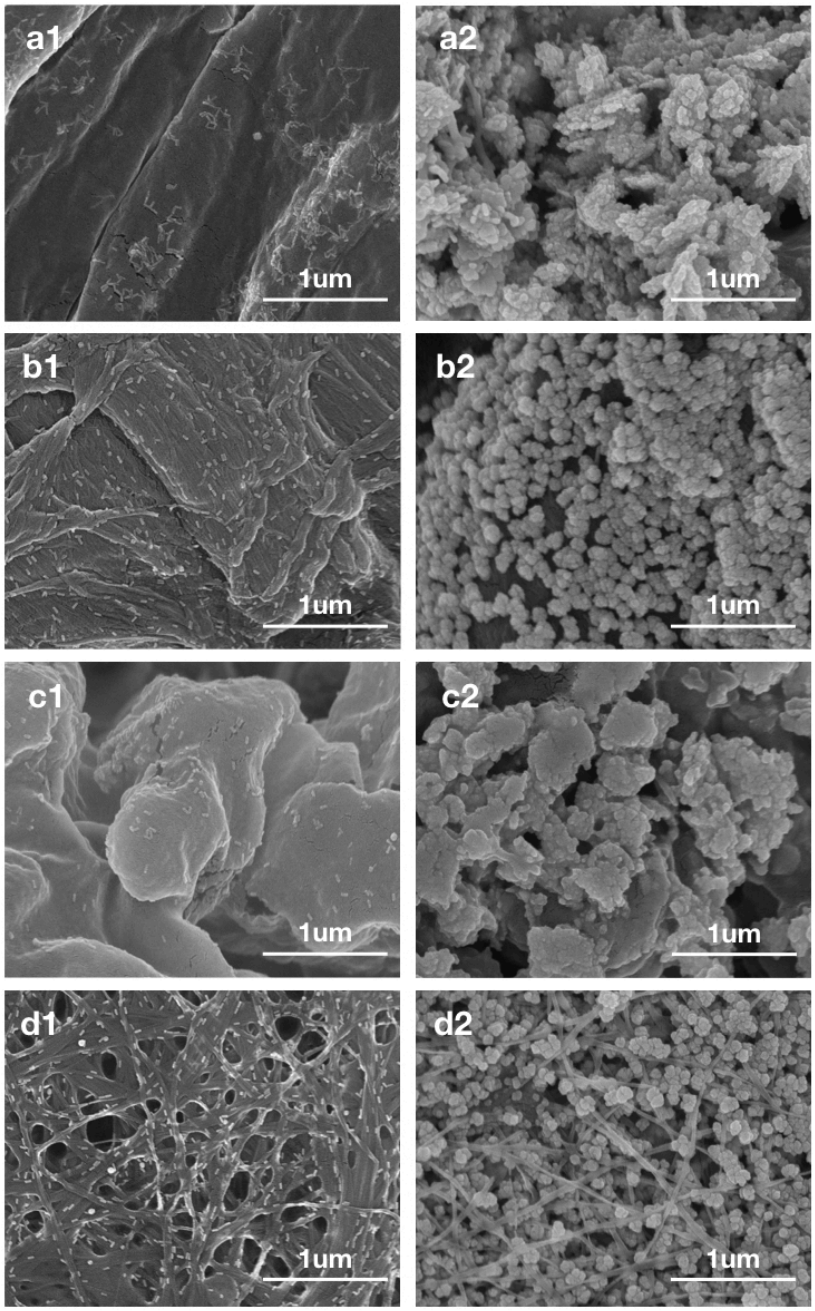

Figure 3.9: SEM images showing AuNRs before and after 15 minutes' silver enhancement on different substrates (a1-a2: printing paper; b1-b2: Whatman filter paper; c1-c2: nitrocellulose; d1-d2: bacterial cellulose).

have been formed on both printing paper and nitrocellulose substrates. Compared to other three cellulose substrates, the ultrafine nanoscale network feature of bacterial cellulose (shown in Fig. 3.9(d1) and (d2)) anchors the AuNR cored silver shelled particles in its 3D network, and hence provides higher retention capability.

3.4.2 QR code self-assembly on different substrates

Self-assembling process of the proposed FEC biosensor prototype have also been validated on these four substrates as shown in Fig. 3.10. AuNRs solution with concentration of 4.13×10^{-9} M has been dispensed onto prototypes' self-assembling regions using a low cost calligraphy method as described in section (3.3.2). Self-assembling process occurs once the silver enhancement solution is applied to the regions where AuNRs have been patterned. However, in the case of printing paper not only AuNRs but also other chemical binders facilitate the silver ion reduction. As a result, silver deposition occurs in the region of substrate wherever exposed to the silver enhancement reagent, which makes the QR code undecodable in less than 4 minutes as shown in Fig. 3.10(a3).

Although good text development result has been achieved on filter paper as shown in Fig. 3.8(b), filter substrate of the prototype gets yellow in the self-assembling process (Fig. 3.10(b2) and (b3)). The QR code deviates from a valid QR code, lies outside of the decoding radius and becomes a invalid code-word ultimately. This is because impurities contained in ink (used to print QR code) get dissolved in silver enhancement solution and have been dispersed off their original spots as silver enhancement solution spread out on the porous filter paper. As time progresses, more ink impurities get accumulated in the regions where black QR code modules are not printed. Silver ions get reduced and accumulates in those regions, which acts as the noise and corrupts the QR code ultimately. Same thing

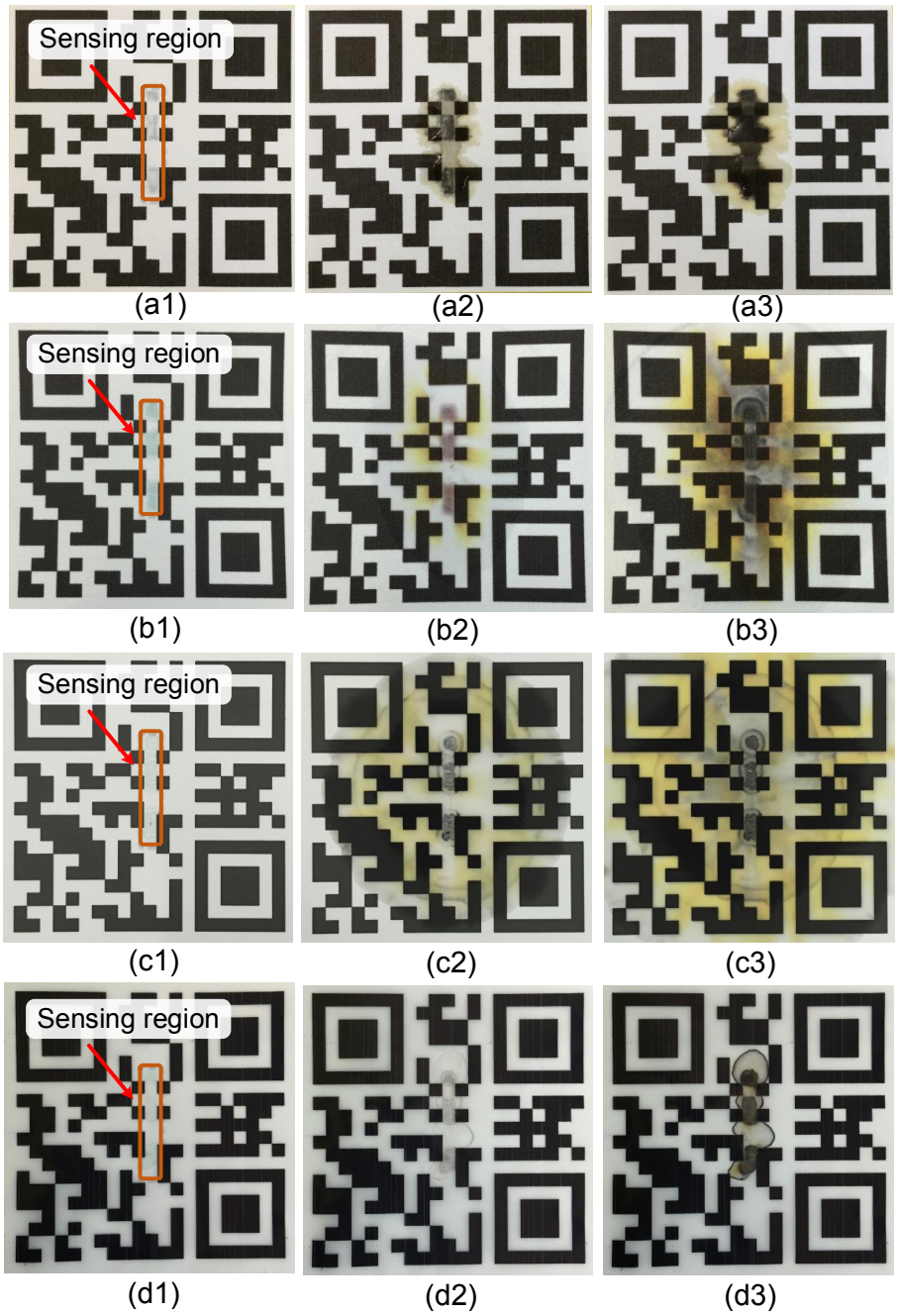

Figure 3.10: QR code biosensor prototype using: (a1)-(a3) printing paper, before SE, 2min and 4min after SE, separately; (b1)-(b3) filter paper, before SE, 5min and 15min after SE; (c1)-(c3)nitrocellulose membrane, before SE, 5min and 15min after SE; (d1)-(d3) bacterial cellulose, before SE, 5min and 15min after SE.

occurs on the nitrocellulose membrane based QR code biosensor prototype also because of its porous feature, as shown in Fig. 3.10(c1)-(c3).

Besides bacterial cellulose's high particle retention capability due to its ultrafine nanoscale network, it also has advantages over previous substrates: 1) there's no impurities contained in the substrate can facilitate the silver enhancement; 2) it is not as porous as filter paper and nitrocellulose paper so that the applied silver enhancement solution can be retained in the spot where it is originally applied. Fig. 3.10(d3) shows the self-assembled FEC sensor using bacterial cellulose substrate after 15 minutes' self-assembling. The modules where AuNRs were dispensed have been successfully developed and in the meantime keep their neighborhood area intact. "Coffee ring effect" observed in Fig. 3.8(d3) persists in this case, as shown in Fig. 3.10(d3). Fortunately, due to the error correction capabilities embedded in the QR codes encoding process, it has little effect on the decoding process. QR code can be successfully decoded with a standard smart-phone and readers can verify this using their own smart-phones.

3.4.3 Quantitative measurement using QR codes

We also verified whether the proposed sensing approach could be used to infer the concentration levels of target analytes. Three dilution levels (1:1, 1:3 and 1:9) of AuNR solution at the concentration of 4.13×10^{-9} M were prepared and dispensed in the self-assembling regions of QR code on bacterial cellulose. The time used to successfully decode the QR code after the silver-enhancement solution applied was measured for different dilution levels. Each measurement was repeated three times and the relative error-bars were also shown in Fig. 3.11. As it can be seen from Fig. 3.11, the QR code detection time, or assembly time increases monotonically with respect to the AuNR dilution levels, thus demonstrating the use of QR decoding for measuring concentration levels of target analytes.

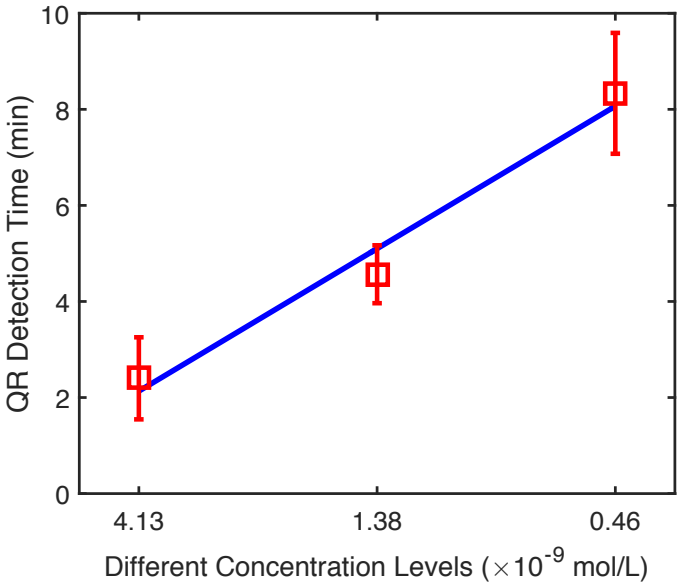

Figure 3.11: Time measured to assemble the valid QR code using silver enhancement for different concentration levels of AuNR solution on the bacterial cellulose substrate.

3.5 Summary and discussion

In this chapter a QR encoded FEC biosensor which is based on self-assembly with silver enhancement technique is demonstrated. The silver enhancement process self-assembles segments of a QR code that can be scanned and decoded using a standard smart-phone. Similar to our previously reported approach for self-assembling RF antennas, this method can also be viewed as a process that transitions from a high-entropy state (random codeword) to a low-entropy state (valid QR codeword) which is opposite to the effect due to environmental artifacts. Thus, we believe that similar to the spirit of FEC biosensing principle the proposed method should yield lower false-positives and higher reliability.

We have compared four paper-based substrates for printing and assembling QR codes which includes regular printing paper, Whatman filter paper, nitrocellulose membrane and lab synthesized bacterial cellulose. Among these four different substrates, lab synthesized bacterial

cellulose outperforms the other three. Although "coffee ring effect" occurs after the silver enhancement process, the assembled QR code can be correctly decoded due to the FEC capabilities embodied in the encoding process of the QR code. It also has been shown in the paper that QR code self-assembling time can be used to infer the target analyte concentration levels.

Based on the QR based decoding, there are two use cases for the proposed biosensor in real-world applications. In the first use case, a consumer triggers the sampling of the analyte using a capillary channel (a dipstick configuration) and then waits for the result of silver-enhancement. Our measurement results show that the detection time will provide an estimate of the concentration of the target analyte which then could be used as a contamination flag. The second use case, which is more challenging is that the embedded biosensor continuously samples the analyte and updates the QR code. In this case the key challenges lie in the packaging of the biosensor and accurately controlling the flow of different reagents so that its operation matches the shelf-life of the product. Another challenge is to reproduce the quality of the biosensor and reduce its production cost when fabricated in large volumes. To address this issue the research focus will be to investigate inexpensive approaches for developing silver-enhancement reagents and to investigate reliable dispensing of the AuNR ink and other reagents using the inkject printing technique. Future work will also focus on enhancing the shelf-life of the biosensing platform and on optimizing the amount of reagent used for analysis. Also, future work will focus on leveraging cloud-based computation and data-fusion capabilities to improve the reliability of detection and to provide updated feedback to the end user.

Chapter 4

Sample Acquisition with Paper-based Microfluidics

Although in Chapter 2 and Chapter 3 we have verified the proof-of-concept biosensor prototypes (RFID based and QR code based) which can be used for bio-molecule detection by self-assembling part of transducer strucutres (RF antennas or QR code-words) using a silver enhancement technique. Both of these biosensors require a direct access to the sample analyte, which would be a issue in the scenario when the samples to be analyzed are concealed. The scenario routinely occurs in food and medicinal supply-chain where the samples are packaged and shipped in sealed containers. Hence a self-powered approach that can sample and process the reagent, and control its flow is necessary. In this chapter, we will probe the use of paper-based microfluidics for self-powered reagent delivering and processing. We will investigate to integrate paper-based microfluidics channels on both passive RFID and QR code based biosensors for silver enhancement reagent delivering.

4.1 Introduction

Paper based microfluidics devices, also known as "lab on paper", is an active area of research because it provides a simple, low-cost platform to analyze liquid samples in the field. Examples of such platform include biological assays that can detect and measure different concentration levels of *Salmonella* [40, 76], glucose [71, 94], cholesterol [70] and protease[90]. The principle underlying all these paper-based platforms is to immobilize protein-based reactive elements (enzymes, antibodies, aptamers, peptides or DNA) on paper in conjunction with a transducer that converts the binding of the target analyte with the protein into a measurable signal.

Broadly these devices can be categorized into four classes based on their detection method [54]: a) colorimetric detection [40]; b) electrochemical (EC) detection [70, 71]; c) chemiluminescence (CL) detection [94] and d) electrochemiluminescence (ECL) detection [63]. Colorimetric method is useful when a yes/no answer (target present or absent) is sufficient, whereas the EC method is used when a high detection sensitivity is required. The CL and ECL methods have not been widely used for paper-based biosensors since they require a optical-shield for read-out.

Irrespective of their read-out methods, all these techniques require a direct access to the biosensor (optically or electrically), and hence cannot be used under scenarios when the samples to be analyzed are concealed. The scenario routinely occurs in food and medicinal supply-chain where the samples are packaged and shipped in sealed containers. For such applications there exists a need to monitor the quality of the product at every point of the supply-chain (without opening the package) so as to prevent and track the source of any contamination due to food-borne pathogens. Hence a self-powered approach that can sample and process the reagent, and control its flow is necessary. In this chapter paper-based microfluidics channels have been intergrated on the RFID based biosensor and QR code

based biosensor reported in chapter 2 and 3 to control the process of sample acquisition and silver enhancement in a passive manner.

4.2 Integration of paper-based microfluidics on RFID biosensor

In this section, we first show that paper-based microfluidics can be used for low-cost and self-powered sample acquisition, sample flow and sample mixing. Second, we show that the microfluidic network can be integrated with a low-cost, ink-jet printed antennas on a plastic substrate. Third we demonstrate a proof-of-concept detection using an integrated commercial RFID tag compliant with the Gen-2 ultra-high-frequency (UHF) standard. The basic principle of self-powered assembly and the growth of RF antenna elements has been described in chapter 2 and is omitted here for the sake of brevity.

4.2.1 Integration with paper-based microfluidics

Principle of operation

One of the focus of this section is to show that the principle of RF antenna self-assembly can be integrated with paper-based microfluidics by selecting the regions where silver-enhancement could occur. Most of the paper-based microfluidics devices are fabricated by patterning hydrophilic channels and hydrophobic barriers on cellulose-based paper membranes, such as cellulose chromatography papers [85] and cellulose filter paper [55]. In this paper, we have used nitrocellulose membranes (manufactured by Millipore) as our microfluidics substrate due to its high antibody binding capacity and consistent pore size [74]. This is important because the length of the microfluidic channels is determined by the degree of penetration of

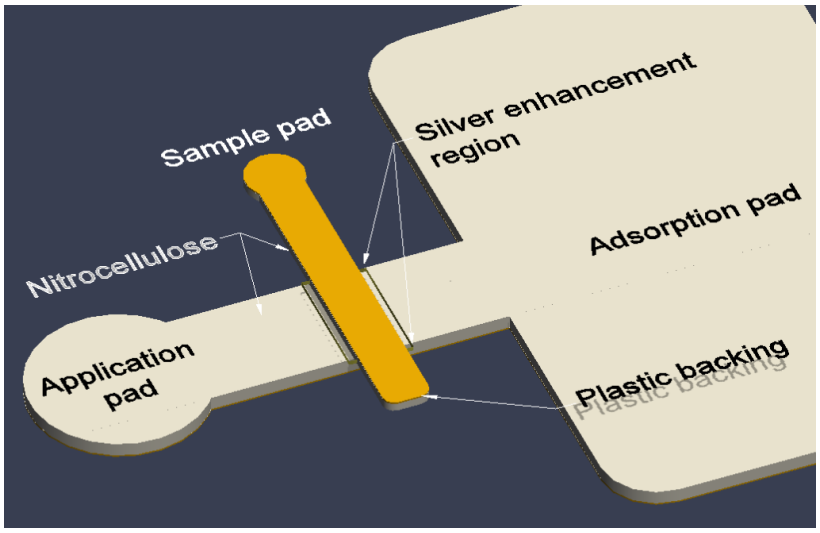

Figure 4.1: Concept of integrating the principle of silver enhancement with paper-based microfluidics.

the liquid through the porous nitrocellulose membrane, which is approximately modeled by the Washburn's equation [55] as:

$$L = \sqrt{\frac{\gamma R cos\theta}{2\eta} t} \tag{4.1}$$

where L is the liquid penetration distance in the paper, R is the average radius of pore size, γ is the surface tension of the liquid, η is the liquid viscosity and t is the time of the penetration. Both the parameters L and t have been used to optimize the size of the microfluidic channels as discussed in section 4.2.3. Also for the sake of reliability, in this paper we have avoided the use of photolithography and wax printing to form reagent channels. Instead we have resorted to laser cutting to create different shapes that can function as liquid channels. Note that laser-ablation will typically burn the walls of the nitro-cellulose membrane. However, we only cut the 4mil plastic backing on the nitrocellulose membrane (both HF13504XSS and HF18004XSS). We carefully adjusted the power/current and the cutting speed of the Full Spectrum Laser LLC MLE-40 to make sure the membrane is not over burned. After this

laser pre-treatment, a razor blade is used to cut through the desired shape along the lines created by the laser cutting on the plastic substrate. The flow of the reagents through the channel is self-powered through capillary force of the membrane and the rate of the flow is controlled by changing the channel width. This can be used to control the rate of flow of the silver-enhancement solution as illustrated in Fig. 4.1. The region where silver enhancement occurs is the area (depicted by the labeled black box) where the two nitrocellulose membranes face each other. When the silver enhancement solution is applied to the application pad, it diffuses through the nitrocellulose channel to the adsorption pad and in the process it interacts with the gold-nanoparticles located in the target area.

Integration of paper-based microfluidics on RFID tag

A visualization of a complete RFID antenna with an integrated microfluidic platform is shown in Fig. 4.2 where a dipole antenna structure is printed on the mesoporous substrate as shown in Fig. 4.3. We will refer to the side of the substrate where the antenna is printed as the "front side" and the opposite side that does not contain printed antenna will be referred to as the "back side". Two small apertures are created on the polyethylene substrate on two sides of the gap, labeled as "SE aperture" in Fig. 4.2(b). These two SE apertures provide a path for the silver enhancement reagent to flow from the back side of the substrate. The antenna gap is covered with a nitrocellulose membrane ("AuNP Pad") with the nitrocellulose side facing the gap on the front side. The "SE Pad" and "Adsorption Pad" are then attached on the back side of the substrate with the nitrocellulose side facing the SE apertures, as shown in Fig. 4.2(b). These three pads serve as reservoirs which control the flow of the liquid reagent through the nitrocellulose channels.

Target specific antibodies, anti-IgG in this case, are then immobilized on the AuNP Pad where faces the gap of the ink-jet printed antenna. Similar to the operation principle of the

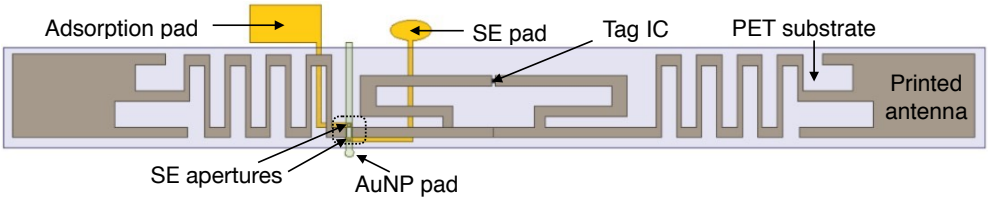

(a) Schematic of the self-powered microfluidics RFID biosensor

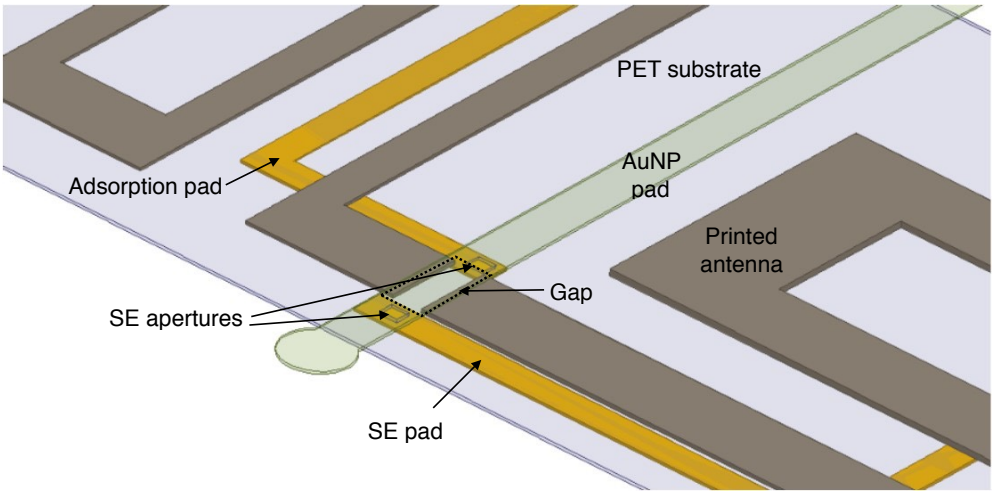

(b) Magnification of the area marked in Fig. 4.2(a)

Figure 4.2: Assembly and integration of microfluidics channels within the RFID biosensor.

lateral-flow immunoassay method [89], the target analyte, IgG in this case, first conjugates with the gold nanoparticle labeled anti-IgG to form a partial sandwich structure (IgG-aIgG-AuNP). When the partial sandwich conjugate is applied to the AuNP Pad, it flows along the nitrocellulose membrane due to its capillary force. Due to antibody-antigen hybridization, a complete sandwich structure, aIgG-IgG-aIgG-AuNP, can be formed when the partial sandwich structured target analytes flow into the area where target specific aIgG is immobilized. The state of the antenna gap region after the formation of sandwich structure is similar to that shown in Fig. 2.2(a), where the gap is electrically insulated since the gold nanoparticle size is not sufficient large to electrically bridge the split antenna segments. When silver enhancement solution is applied to the SE Pad, it moves through the nitrocellulose channel to the AuNP pad and then adsorption pad through SE apertures. Once the sandwich structure is exposed

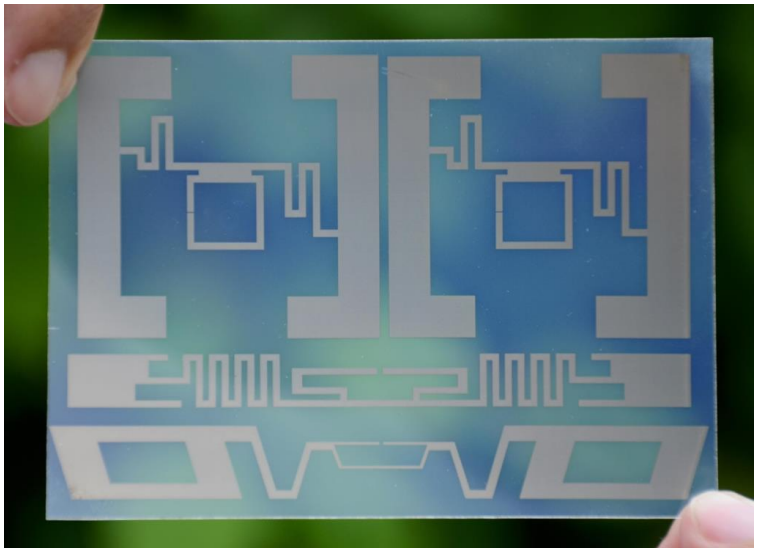

Figure 4.3: Ink-jet printed dipole antenna samples using conductive ink with EPSON C88+ printer. From top to bottom: ALN-9634 tag, ALN-9640 tag and UPM Raflatac Short Dipole.

to the silver enhancement solution, silver ions reduction process occurs. As time progresses, more and more silver ions get reduced on the surface of the gold nanoparticles, as a result of which the size of the shell grows and ultimately electrically bridges the antenna gap (similar to the state that shown in Fig. 2.2(c)). The assembly of silver micro-monopole antennas in between the antenna gap tunes the effective length of the ink-jet printed antenna.

4.2.2 Materials and methods

Materials

Silver Enhancement Kit, anti-rabbit IgG conjugated with gold nanoparticles, anti-rabbit IgG, IgG, Glutaraldehyde and Methanol were were all purchased from Sigma-Aldrich (St. Louis, MO, USA). Nitrocellulose (NC) membranes with flow rate of 135sec/4cm and 180sec/4cm were purchased from Millipore (Billerica, MA, USA). Deionized (DI) water used in the experiment was obtained through Millipore water purification systems (Billerica, MA, USA).

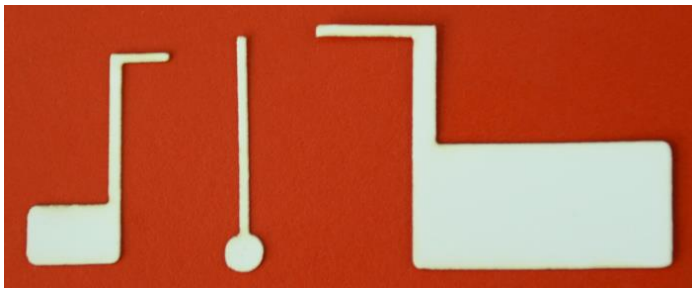

Figure 4.4: Nitrocellulose membrane pads cut using a Full Spectrum Laser MLE-40 system. From left to right: SE Pad, AuNP Pad and Adsorption Pad.

The chipset attached to the ink-jet printed antenna was removed from EPC Gen 2 ALN-9640 tag which was purchased from Alien Technology (San Jose, CA, USA). MLE-40 laser system from Full Spectrum Laser (Las Vegas, NV, USA) was used for nitrocellulose membrane pads cutting. An EPSON stylus C88+ ink-jet printer was used to print the antenna structure. The printing substrate and the JS-B25P silver ink were purchased from Novacentrix (Austin, TX, USA). Scanfob Ultra-BB2 Wireless GEN2 UHF RFID Reader/Writer (Cedar Park, TX, USA) was used for remote interrogation and measurements. All the experiments were carried out in a certified Biological Safety Level II laboratory.

Procedure

The nitrocellulose membrane was cut into the desired shapes to form SE pad, AuNP pad and Adsorption pad using the MLE-40 laser according to the shapes shown in Fig. 4.4. Finite-element simulation was used to optimize dipole antenna structure layout to match the impedance of the antenna and the ALN-9640 RFID tag chip. Details of the antenna optimization is provided in [64] and is omitted here for the sake of brevity. The antenna with 80μm gap was ink-jet printed using EPSON C88+ printer and JS-B25P silver conductive ink on the mesoporous substrate. After antennas have been printed they are annealed in the oven at a temperature of 70°C for 1 hour. This process facilitated the evaporation of

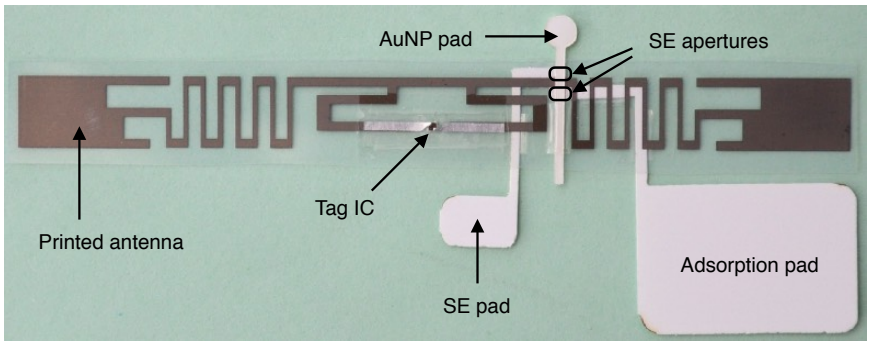

(a) Front side of the self-powered microfluidics RFID biosensor prototype

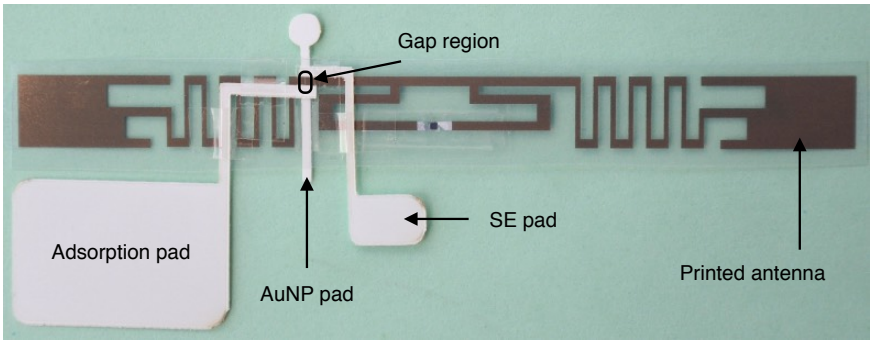

(b) Back side of the self-powered microfluidics RFID biosensor prototype

Figure 4.5: Photos of the front side and back side of the sensor prototype.

solvent contained in the silver conductive ink and it created a uniform conductance across the antenna structure. The ALN-9640 tag chip was removed from the original tag and was attached to the printed antenna using tape, as shown in Fig. 4.5.

Using the procedure described in [102], anti-IgG was immobilized on the nitrocellulose surface of AuNP pad where faces the printed antenna gap. Two SE apertures with a dimension of around 1.0mm×1.5mm were created on two sides of the gap on the mesoporous substrate as shown in Fig. 4.5. The AuNP pad was then attached to the antenna using the tape. The two SE apertures were created to provide a path for the silver enhancement solution to flow from SE pad that was attached on the back side of the substrate. The SE pad and the adsorption pad were attached to antenna such that their end-points covered the two SE apertures, separately, as shown in Fig. 4.5(b). The sequential operation of sample processing

can be controlled by the adjusting the length of the flow channel and the pore size of the NC membrane. For instance, silver enhancement procedure requires mixing of the initiator and the enhancer solution in a volume ratio of 1:1. The silver enhancement solution then flows to the end-point of the SE pad (beneath the SE aperture) which is then drawn by the AuNP pad through SE aperture and then by the adsorption pad if sufficient reagent is provided. During this process, the aIgG-IgG-aIgG-AuNP sandwich structure is exposed to the silver-enhancement solution. Silver ions start to get reduced into metallic silver on the surface of the gold nanoparticles, in the process of which the split segments of the ink-jet printed antenna are being bridged given sufficient time and target analyte. Once this silver micro-monopole antennas' self-assembling process has been finished, the response of the sensor tag was measured using the 915MHz Scanfob Ultra-BB2 reader. The RFID reader can interface with a laptop through cable or a smartphone through bluetooth for data analysis and display.

4.2.3 Measurement results

Ink-jet printed gap using silver ink

In this work, we use ink-jet printing method to print the antenna with gap instead of manually creating the gap on an existing tag [100, 102]. This ensures uniformity of the gap and the procedure can be scaled across many samples. Besides, simulation results in [102] show that a smaller gap length can result in a high sensitivity of the biosensor in the situation when the gap conductance is relatively low. Even though the gap between the electrodes can be bridged by silver micro-monopole antenna chain as shown in Fig. 2.2(c), the conductance is not as high as that of bulk silver. To improve the sensor's sensitivity, a small gap is therefore preferred. Due to the offset of printer nozzle and the nature that the silver ink is in liquid

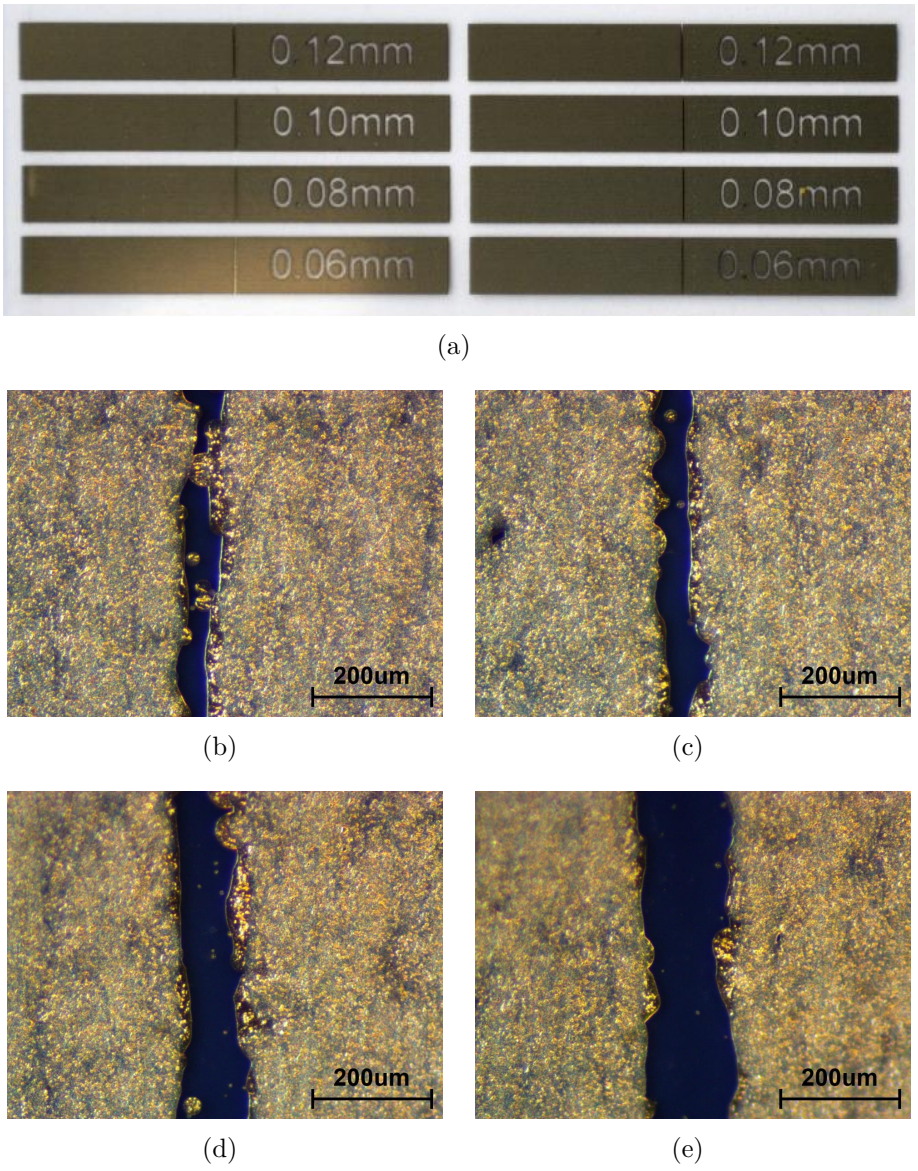

(a)

(b) (c)

(d) (e)

Figure 4.6: (a) Photo of silver ink printed gaps with different sizes on the mesoporous substrate using EPSON C88+ printer (sizes of gaps from top to bottom: 120μm, 100μm, 80μm and 60μm); (b), (c), (d) and (e) are the microscope photos of the actual printed gaps at layout sizes of 60μm, 80μm, 100μm and 120μm, respectively.

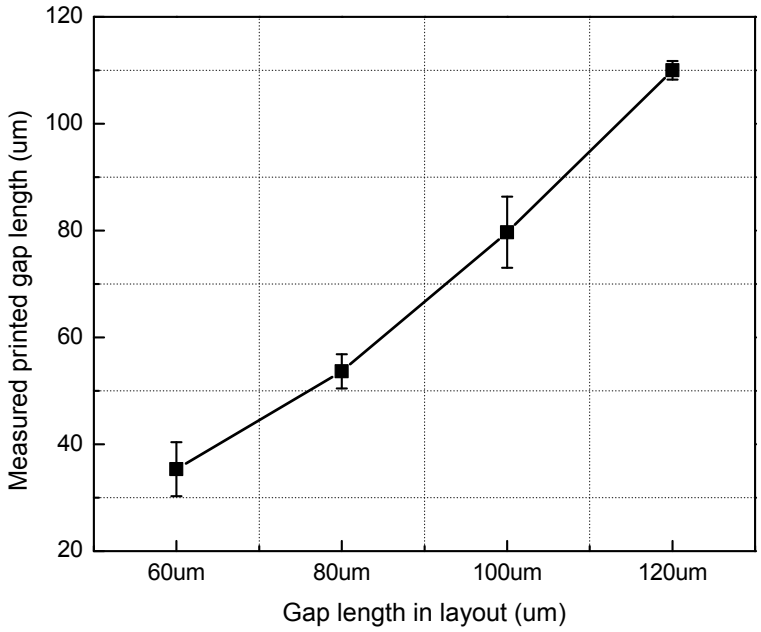

Figure 4.7: Comparison of the gap length drawn in layout with the gap length that are printed.

form, the length of actual printed gap is smaller than that drawn in the layout software. To examine the minimum gap length that can be ink-jet printed, a set of gaps at different sizes (ranging from 60 to 120μm at a increasing step of 20μm) are printed using EPSON C88+ printer as shown in Fig. 4.6(a). Microscope photos of the printed gaps of different lengths are shown in Fig. 4.6(b) to Fig. 4.6(e). With the microscope examination of printed gaps, most of the electrodes of the gaps drawn in a length of 60μm in the layout are electrically shorted as shown in Fig. 4.6(b). A high yield of the printed gaps without ink overlap can be achieved for the gaps drawn at a size equal or larger than 80μm (Fig. 4.6(c) to Fig. 4.6(e)). A comparison of the lengths of actual printed gaps and the lengths drawn in the layout software is shown in Fig. 4.7. The lengths of printed gaps are 10μm to 30μm smaller than that drawn in the layout. In the implementation of the self-powered micro-fluidics sensor, the antenna with the gap length of 80μm is ink-jet printed and used.

Silver enhancement reagent flow rate

The liquid flow speed on the nitrocellulose membrane needs to be optimized since it controls how fast the adsorption pad can absorb the silver enhancement solution and how fast the SE pad can transport the liquid. However, accurate measurement of liquid flow-rate in a nitrocellulose membrane is difficult as the rate decays exponentially with respect to the distance [74]. A more common method used to measure the capillary flow is the time needed for the liquid to move and fill completely a membrane of a given length. The pads used for silver enhancement solution flow rate testing are cut into the shapes shown in Fig. 4.8(a) using MLE-40 laser system. The round reagent application end-point has a dimension of 6mm in radius. The rectangular liquid flowing areas are 40mm in length and have different widths ranging from 1mm to 2.5mm. During the flow rate measurement 120μL silver enhancement reagent solution was applied to the reagent application pad using pipette pump. Two different flow rate membranes (HF13504XSS and HF18004XSS) are tested, separately, and the measured silver enhancement reagent flow rate are shown in Fig. 4.8(b). The detailed parameters and materials of the three pads (SE pad, AuNP pad and adsorption pad) which are used in the implementation of the sensor are listed in the Table 4.1. To note that in the experiment when the silver enhancement solution was applied onto the SE pad with a smaller width, it took a longer time for the reagent to pass through the SE aperture to reach AuNP pad. Our explanation for this phenomena is that if a narrow SE pad is used to guide the silver enhancement reagent to AuNP pad it need more time to aggregate the same amount of the solution at the end-point to pass through the SE aperture and then reach the adsorption pad. This feature can be used to change the monitoring duration by changing the pad width.

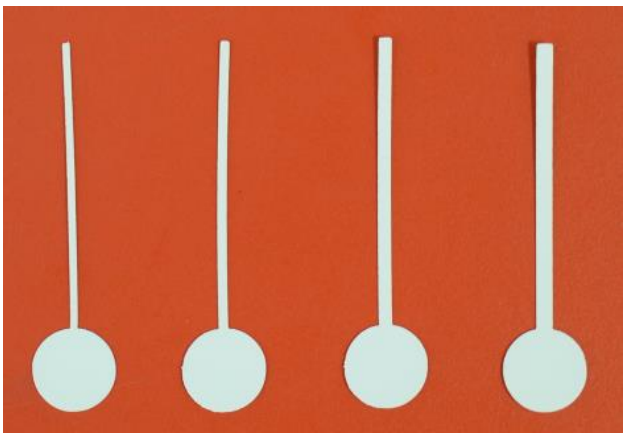

(a)

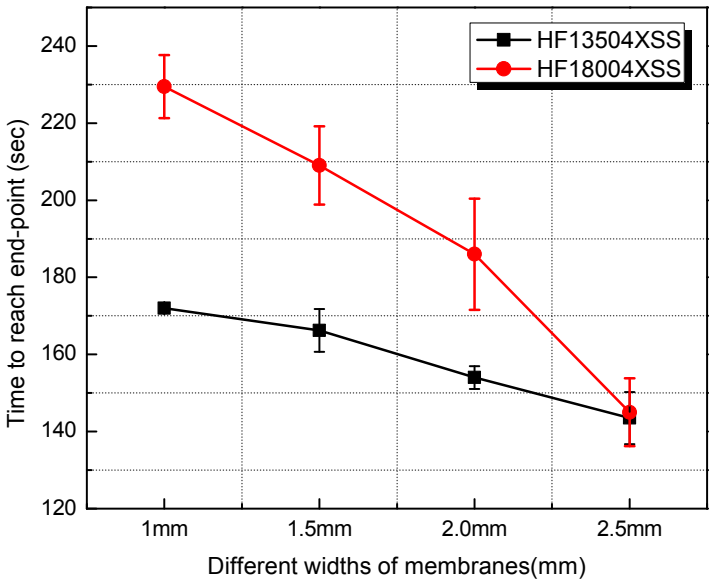

(b)

Figure 4.8: (a) Nitrocellulose membrane pads of different widths cut using Full Spectrum Laser LLC (MLE-40) for silver enhancement solution flow speed measurement; (b) Flow speed of HF13504XSS and HF18004XSS membrane pads at different widths (1mm, 1.5mm, 2.0mm and 2.5mm).

Table 4.1: Materials and Parameters of Three Pads

	SE Pad	AuNP Pad	Adsorption Pad
Membrane	HF13504XSS	HF18004XSS	HF13504XSS
Width (mm)	2.0	1.5	2.0

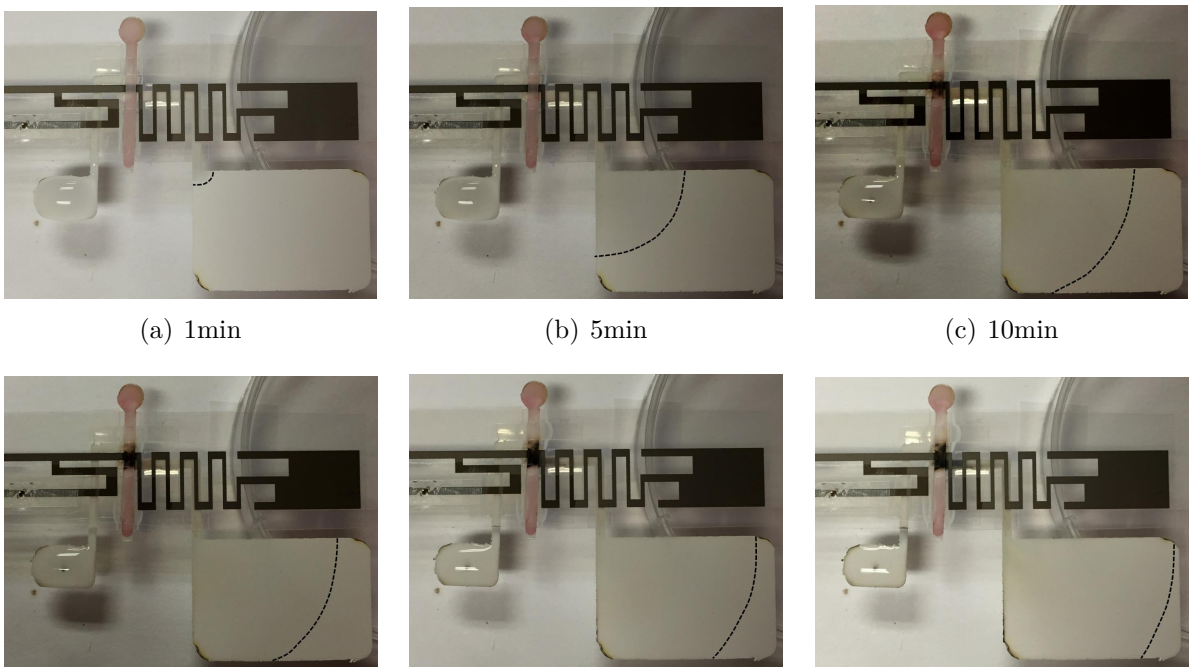

(a) 1min (b) 5min (c) 10min

(d) 15min (e) 20min (f) 25min

Figure 4.9: Demonstration showing that the adsorption pad can continuously absorb the silver enhancement solution during the micro-monopole antenna growth. (a) to (f) show the area covered by absorbing silver enhancement solution after 1min, 5min, 10min, 15min, 20min and 25min separately after the solution path has been formed. The dark dashed lines show the boundaries between the area where silver enhancement reagent front has occupied and where it hasn't.

Measurements using an integrated prototype

The operation of a fully integrated RFID biosensor was verified where the nitrocellulose pads enabled acquisition of the liquid sample acquisition, sample mixing and sample flow to areas where micro-monopole antennas can self-assemble only when target analytes are present. For the fabricated prototypes, the adsorption pad was designed to have a sufficiently large surface area and volume such that it is able to continuously absorb silver enhancement solution diffusing from the SE pad and to facilitate continuous evaporation of the reagent to self-power the diffusion process.

Fig. 4.9 shows a set of photos illustrating a complete process of growing the antenna as the silver-enhancement solution flows through the microfluidic channels. Fig. 4.9(a) was taken 1 min after the silver enhancement solution was applied through the SE aperture and reached adsorption pad. It can be seen that the silver micro-monopole antennas start to assemble but are not large enough to bridge the antenna gap. The dashed black line on adsorption pad highlights the boundary where the silver enhancement solution filled the pad. It can be seen in Fig. 4.9(a) to Fig. 4.9(f) that as time progresses the absorption pad fills up. After 25 minutes, the gap is fully bridged with AuNP cored silver shelled micro-monopole antennas and the split segments of the printed dipole antenna are now electrically bridged. It can be also be seen in Fig. 4.9(f) that even when the split antenna segments are bridged, the silver enhancement reagent hasn't filled up the volume of the adsorption pad, which indicates the adsorption pad is still capable to absorb more of the incoming reagent.

Experiments using 915MHz RFID reader

The process of bridging the antenna (leading to change in the effective length of the dipole) can be detected wirelessly using an COTS RFID reader. For calibration purposes an unmodified 915MHz dipole antenna (identical structure as the biosensor dipole but without gap) was also integrated with the biosensor. All interrogation measurements from the biosensors (L_1) were normalized with respect to the measurement obtained from the calibration dipole (L_2). To minimize the mutual loading the sensor tag and the calibration tag were placed next to each other and a ratiometric readout technique was used [102].

The preliminary results that compare the normalized detection range under two situations (shown in Fig. 4.10): silver enhancement does not occur when the target analyte is absent; silver enhancement process grows the antenna, which bridges the split ink-jet printed dipole antenna. In the first case, the measured farthest interrogation distance is only 23.5% with

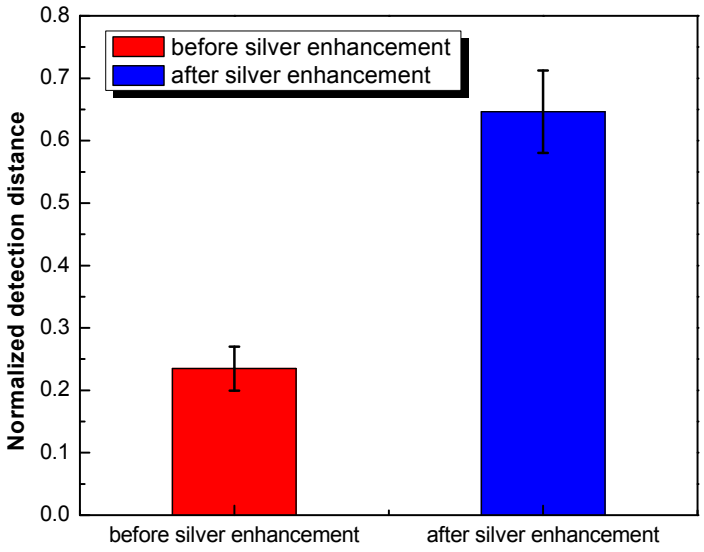

Figure 4.10: Measured results validating the proof-of-concept RFID biosensor.

respect to that of the calibration tag. For the second case that with silver enhancement, the measured maximum interrogation distance increases to 64.6% with respect to that of the calibration antenna. It validates the proof-of-concept of integration of paper based microfluidics in self-powered self-assembled RFID biosensor.

4.3 Integration of paper-based microfluidics on QR code biosensor

A paper-based microfluidics channel also has been integrated on the QR code biosensor underneath the substrate for acquiring, mixing and flowing the sample to areas on the substrate where different parts of the code can self-assemble in presence of immobilized gold nanorods.

4.3.1 Integration with paper-based microfluidics

Paper-based microfluidics is used for sampling and directing the flow of analytes to the regions of the QR code that can self-assemble. In this work we have used nitrocellulose membranes (manufactured by Millipore) as our microfluidics substrate due to its high bioreceptor (e.g. antibodies) binding capacity and consistent pore size [74]. When the silver enhancement solution is applied to the application pad, it diffuses through the nitrocellulose channel to the adsorption pad and in the process it interacts with the gold nanorods immobilized in the target area. For the proposed QR code, target specific primary probes could be immobilized in the specific regions of the code, for instance the highlighted region shown in Fig. 3.2(d). Similar to the operation principle of the lateral-flow immunoassay [89], target specific analyte will first conjugate with the AuNR labeled secondary probe to form a partial sandwich structure. When the partial sandwich conjugate diffuses to the regions where the primary probes are immobilized, a complete sandwich structure will be formed. Thus, the state of the QR code after the formation of the sandwich structure will be similar to that shown in Fig.3.2(d) because the AuNR cannot be detected by the QR code reader/scanner. After silver-enhancement based staining the color of the target region will change and depending on the concentration of the AuNR could make the QR code decodable (as shown in Fig. 3.2(c)).

4.3.2 Materials and methods

Materials and apparatus

Gold chloride ($HAuCl_4$), Hexadecyltrimethylammonium bromide (CTAB), sodium borohydride ($NaBH_4$), silver nitrate ($AgNO_3$), ascorbic acid and silver enhancement kit were purchased from Sigma-Aldrich (St. Louis, MO, USA). Nitrocellulose (NC) membranes with

flow-time (measure of flow rate) of 135sec/4cm was purchased from Millipore (Billerica, MA, USA). Deionized (DI) water used in the experiment was obtained through Millipore water purification systems (Billerica, MA, USA). An EPSON stylus C88+ ink-jet printer was used to print the QR code. The printing substrate, aqueous inkjet vehicle, the empty cartridge and aqueous inkjet vehicle were purchased from Novacentrix (Austin, TX, USA). Paper mate profile retractable ballpoint pens were bought from Amazon.com, Inc. All the chemicals were used as received without further purification. The experiments were carried out in a certified Biological Safety Level II laboratory.

Synthesis of gold nanorods

Gold nanorods were synthesized by using seed-mediated method [27, 37]. Seed solution was synthesized by adding 0.6 ml of an ice-cold $NaBH_4$ (10 mM) solution into 10 ml of $HAuCl_4$ (0.25 mM) and CTAB (0.1 M) solution under vigorous stirring at room temperature. The color of the seed solution changed from yellow to brown. Growth solution was prepared by mixing 5 ml $HAuCl_4$ (10 mM), 95 ml CTAB (0.1 M), 1 ml $AgNO_3$ (10 mM) and 0.55 ml ascorbic acid (0.1 M), consecutively. The solution was homogenized by gentle shaking. To the resulting colorless solution, 0.12ml of freshly prepared seed solution was added and kept undisturbed in the dark for 14h. Prior to use, the AuNR solution was centrifuged twice at 8000 rpm for 10 min to remove excess CTAB and re-dispersed in nanopure water. UV-Vis extinction spectra were measured using Shimadzu UV-1800 UV-Vis spectrophotometer and shown in Fig. 4.11. The extinction spectrum of AuNR exhibits two characteristic bands at 510 nm and 784 nm each corresponding to the transverse and longitudinal plasmon resonances. These represent unique signatures for a nanorod with a specific length and diameter. The length and diameter of AuNR were respectively measured to be 52.6 $\pm$ 4.4 nm and 13.1 $\pm$

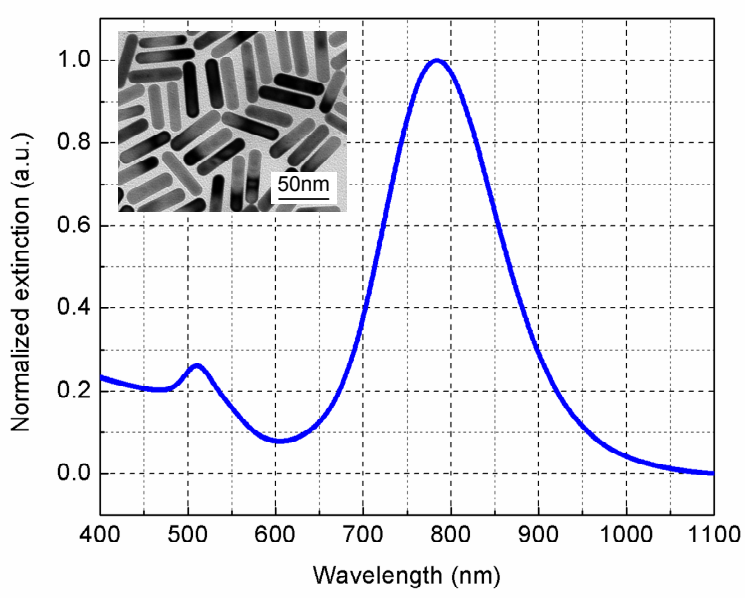

Figure 4.11: Optical extinction spectrum of AuNR verifying the dimensions of the nanorods (inset: TEM image of AuNR).

0.8 nm using Transmission electron microscopy (TEM) (inset in Fig. 4.11). TEM image was collected using a JEOL JEM-2100F field emission microscopy.

Since the focus of this part is the integration of QR code with silver-enhancement based self-assembly, we will skip the process of forming the sandwich structure as shown in Fig. 3.3 and directly pattern gold nanorods at different concentration levels. If we can detect and measure different concentration levels of AuNR, we should be able to extend the approach towards detecting different concentration levels of target analyte based on our previously reported approaches [97, 98, 102].

QR code biosensor prototype fabrication

Fig. 4.12 illustrates the fabrication procedure for the QR code FEC biosensor. QR code shown in Fig. 3.2(c) was first ink-jet printed on both the mesoporous polyethylene substrate and the plain printing paper (this will be used after step shown in Fig. 4.12(c)) with EPSON

Figure 4.12: Illustration of QR code FEC biosensor fabrication procedure: (a) QR code printed on the mesoporous substrate using normal ink; (b) The plastic substrate in the gray colored square dots area removed; (c) NC membrane is attached on the back side of the QR code; (d) AuNR ink is printed on the yellow area.

C88+ printer using normal black ink as shown in Fig. 4.12(a). The five gray squares can be distinguished from other black squares. Disposable Miltex Scalpel #11 blade is used to cut through the plastic substrate along the edges of those five gray modules to remove them from the substrate to form three open windows on the substrate as shown in Fig. 4.12(b). Nitrocellulose membrane with desired shape is attached on the back side of the substrate using transparent tape with nitrocellulose side facing the open windows created in the last step (Fig. 4.12(c)).

Then the single biosensor piece is aligned to the alignment marks on the letter sized printing paper which is printed in the first step and is fixed using transparent tape. For better alignment we used a transparent PET instead of an opaque substrate for printing and fabrication. When the QR code is printed on the transparent substrate, the biosensor can be aligned to the QR code which is printed on a plain printing paper. We can then adjust the position of biosensor by matching the alignment pattern of the QR code on the PET substrate to the alignment pattern of the QR code on the white paper.

The black ink cartridge is replaced with the one filled with aqueous inkjet vehicle. The printer was first initialized (to ensure uniform printing of AuNR patterns) using the procedure described in the previous section. The printing paper (with biosensor attached) is loaded in the printer, and the yellow bar area (shown in Fig. 4.12(d)) which covers the three open windows is printed with AuNR solution. The ink-jet printed AuNRs are captured by the porous nitrocellulose surface. The AuNR printing is a self-alignment process, which only allows the AuNR solution printed in the area facing to the open windows of the substrate to be captured by the nitrocellulose. All the rest ink-jet printed AuNR solution is printed on the surface of the plastic substrate, which improves the yield because normally the commercial printer (e.g. EPSON C88+ we used in our experiment) is not able to provide a very precise alignment for multiple loadings of a single sheet of paper.

Silver enhancement solution is then applied in the "Application pad" of the NC membrane shown in Fig. 4.12(d) and the solution will flow all the way down to the "Adsorption pad" due to the capillary force of the membrane. During this process, the AuNR is exposed to the silver enhancement solution. Silver ions start to get reduced into metallic silver on the surface of the AuNR, which will result in a visible color changing from white to brown or even black. Note that the Adsorption pad is designed to have a sufficiently large surface area

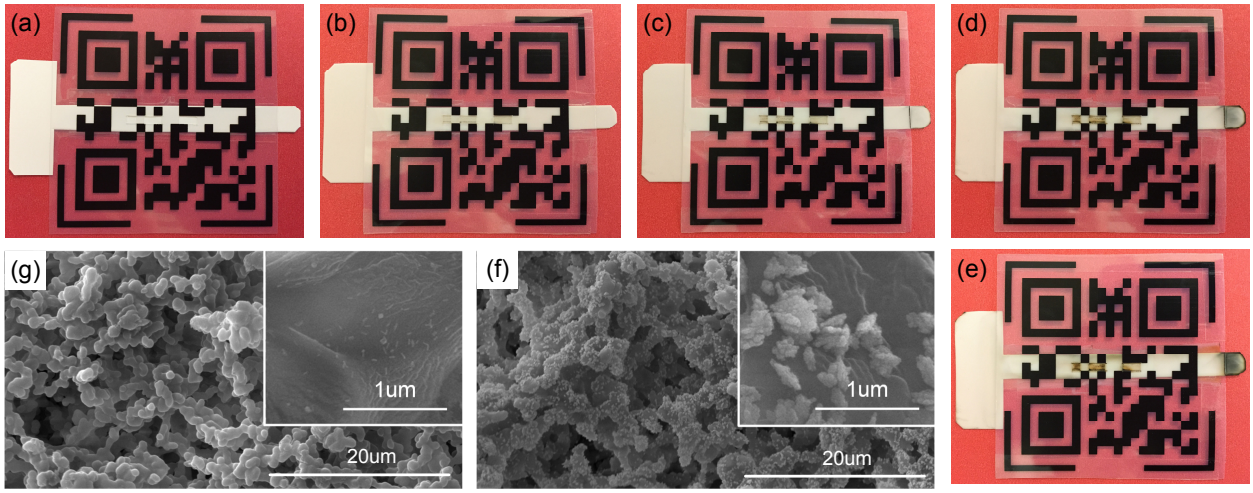

Figure 4.13: (a) AuNR solution printed on the nitrocellulose membrane where faces to the open windows on the substrate before silver enhancement solution applied; (b), (c), (d) and (e) show the color changes of the NC membrane with silver enhancement for 5min, 10min, 20min and 25min, respectively; (f) AuNR on NC membrane after silver enhancement; (g) AuNR captured on the NC membrane before silver enhancement.

so that it can continuously absorb silver enhancement solution diffusing from the application pad and to facilitate continuous evaporation of the reagent to self-power the diffusion process.

4.3.3 Measurement results

The fabricated biosensor prototype is shown in Fig. 4.13(a)-(e). AuNR is ink-jet printed on the NC membrane surface where faces to the open windows on the plastic substrate created by disposable scalpel. As it can be seen in Fig. 4.13(a), the printed AuNR is not visible and hence the QR code is not decodable. Fig. 4.13(b) to Fig. 4.13(e) shows a set of photos illustrating the process of silver enhancement as the QR code assembles. The color change can be visually observed even in just 5min after silver enhancement. In this set of photos the color turns into brown (even black) as time progresses. The word "POSITIVE" can be correctly decoded after 20 minutes' silver enhancement (Fig. 4.13(d)), which the reader can verify by using the QR code scanner on their smart-phones.

The process of silver-enhancement has been verified through an SEM analysis of the enhancement region as shown in Fig. 4.13(g) and Fig. 4.13(f), where the scans were obtained after 30 minutes of enhancement time. The SEM images were obtained using a FEI Nova 2300 Field Emission SEM at an accelerating voltage of 5 kV. The porous surface texture feature of the nitrocellulose membrane provides strong AuNR capturing capability as shown in the inset in Fig.4.13(g).

Quantitative measurement using QR codes

In the next set of experiments we verified if the procedure of QR decoding could be used to infer the concentration level of target analytes. Since in our previous papers we have already demonstrated that measuring the concentration of gold nanoparticle labels to the concentration of target analytes, in this experiment we only measure the concentration levels of immobilized AuNR. We found that direct dispensing of AuNR ink in the enhancement regions is not consistent for different concentration levels. The printer was unable to dispense equal amount of ink for different printing cycles. The primary reasons could be: 1) unequal distances between the tip of the printer head and the surface of the PET substrate and the nitrocellulose membrane creates different printing areas; and 2) the physical properties of the AuNR (e.g. viscosity, surface tension) is not optimized for the hybrid substrate.

Due these limitations, we resorted to calligraph the AuNR ink on the QR assembly regions using a regular ballpoint pen [87, 88]. Fig. 4.14(b) shows the retractable ballpoint pen (from PaperMate) that was used and the inset shows the SEM graph of the pen's dispensing tip. The original ink in the pen's refill container was pushed out using nitrogen gun after the tip and the refill are separated. Then the ballpoint pen refill and the tip are cleaned with ethanol by sonication for 2 days in a centrifuge tube. The ethanol was replaced every 3

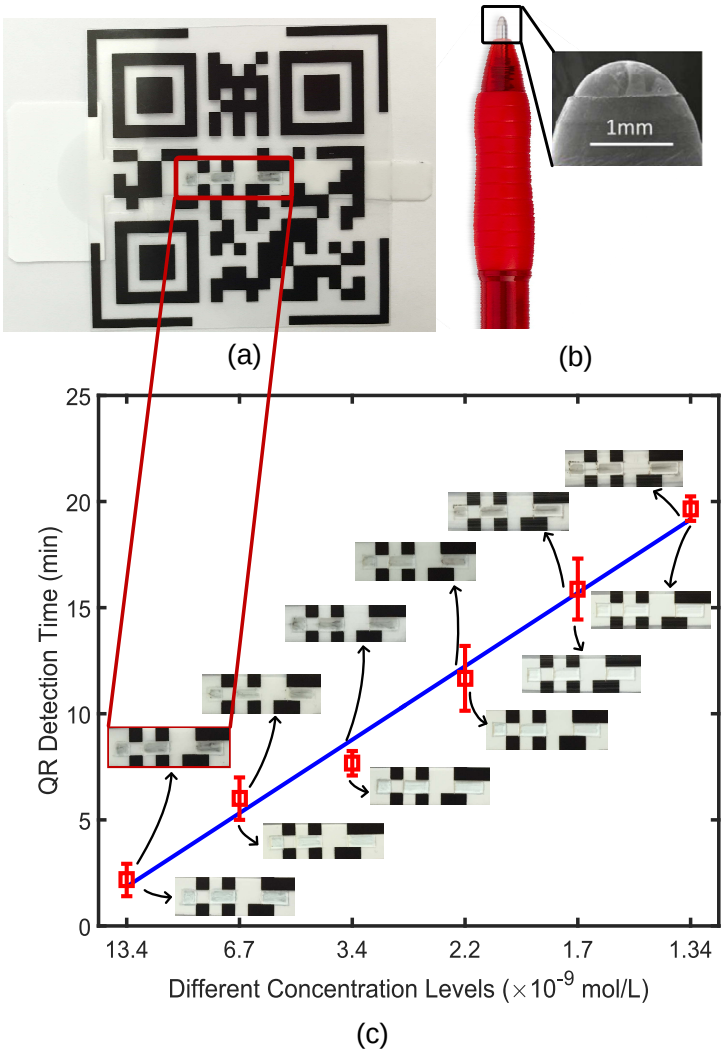

Figure 4.14: Experiments to measure different AuNR concentration levels using the example (a) assembled QR code; where the AuNR ink is dispensed using a (b) retractable ballpoint pen with an SEM image of the tip; (c) time measured to assemble the QR code using silver enhancement for different concentration levels of AuNR solution (Inset shows the sensing region before and after QR segments assembled).

hours. Different dilution levels (1:2 to 1:10) of AuNR solution were prepared and the AuNR concentration level was confirmed using ultra-voilet (UV) measurement [57, 69] according to:

$$A = \epsilon b C \tag{4.2}$$

where A is absorption, ϵ is extinction coefficient, b is the light path in the UV-cuvette, and C is molar concentration of nanoparticle solution. The concentration of AuNRs was determined from the optical extinction of colloidal suspension of AuNR. Extinction coefficient ϵ of AuNR is about 3×10^9 $M^{-1}cm^{-1}$. The extinction of 20× diluted AuNR solution in our study is 2.0, light path is 1 cm, so the molar concentration of AuNR solution (20× diluted) is 6.7×10^{-10} M. The diluted AuNR solution was injected into the cleaned ballpoint pen refill and the pen was then used for writing and dispensing the AuNR ink in the QR assembly regions.

The time to successfully decode the QR code after the silver-enhancement solution was applied was measured for different dilution levels. Each measurement was repeated three times and the relative error-bars are also shown in Fig. 4.14(c). As it can be seen from Fig. 4.14(c), the QR code detection time, or assembly time increases monotonically with respect to the AuNR dilution levels, thus demonstrating the use of QR decoding for measuring concentration levels of target analytes.

4.4 Summary and discussion

In this chapter, paper-based microfluidics channels have been integrated with RFID based biosensor (described in Chapter 2) and QR code based biosensor (described in Chapter 3). These paper-based microfluidics channels are used for acquiring, mixing and flowing the sample to areas on the substrate where different parts of the transducer can self-assemble in

presence of target analyte (immobilized gold nanorods in this case). For the RFID based biosensor, instead of using COTS RFID tags, we demonstrated a low-cost ink-jet printing method that can be used to precisely control the gap length and hence the flow of the silver-enhancement reagent. Nitrocellulose pads were designed, patterned with laser-ablation and integrated on the antenna for sample acquisition, mixing and guiding, serving as reservoirs. The adsorption pad could be designed to be sufficiently large (in volume) to ensure the silver-enhancement solution has enough time to spread and evaporate. Thus the operation of the integrated biosensor is completely self-powered.

There are two use cases for the proposed biosensors (RFID based and QR code based) in real-world applications. In the first use case, a consumer triggers the sampling of the analyte using a capillary channel (a dipstick configuration) and then waits for the result of silver-enhancement. Our measurement results show that the detection time will provide an estimate of the concentration of the target analyte which then could be used as a contamination flag. The second use case, which is more challenging is that the embedded biosensor continuously samples the analyte and updates the QR code. In this case the key challenges lie in the packaging of the biosensor and accurately controlling the flow of different reagents so that its operation matches the shelf-life of the product.

Future work will focus on enhancing the shelf-life of the biosensing platform and on optimizing the amount of reagent used for analysis. Note that for different types of targets and mediums being analyzed (e.g. milk or blood plasma), the parameters of the microfluidic channels (pore size, gap length and channel length) have to be appropriately optimized. So we envision that while the operational principle of the biosensing platform could remain unchanged, the structure of the platform will be different for each use case. Another challenge is to reproduce the quality of the biosensor and reduce its production cost when fabricated in large volumes. To address this issue the research focus will be to investigate inexpensive approaches for

developing silver-enhancement reagents and to investigate reliable dispensing of the AuNR ink and other reagents using the inkject printing technique. Leveraging cloud-based computation and data-fusion capabilities to improve the reliability of detection and to provide updated feedback to the end user could also be part of the future work.

Chapter 5

Analyte Sampling Powered by Light Absorption

In this chapter we exploit graphite's thermal absorption properties to drive the process of analyte sampling in paper-based biosensors. Graphite structures can be easily patterned or drawn on paper using a standard pencil and selective heating of the patterned layers can be remotely achieved using a light source. The resulting thermal gradient manifests itself as concentration gradients across the paper substrate which then triggers the flow of analyte to the selective areas. In this chapter we have validated this hypothesis using a prototype made out of a low-cost filter paper substrate and a 300mW 808nm remote infrared laser source. Compared to a control paper substrate, we show an increase in temperature by more than 70°C (from 50°C to 120°C) in areas where the graphite is patterned. As a result the proposed prototype is also shown to demonstrate a higher sample-flow rate compared to the control. We anticipate that the proposed remote triggering of sample acquisition would be useful for different variants of paper-based biosensors that need to be integrated inside the food-package.

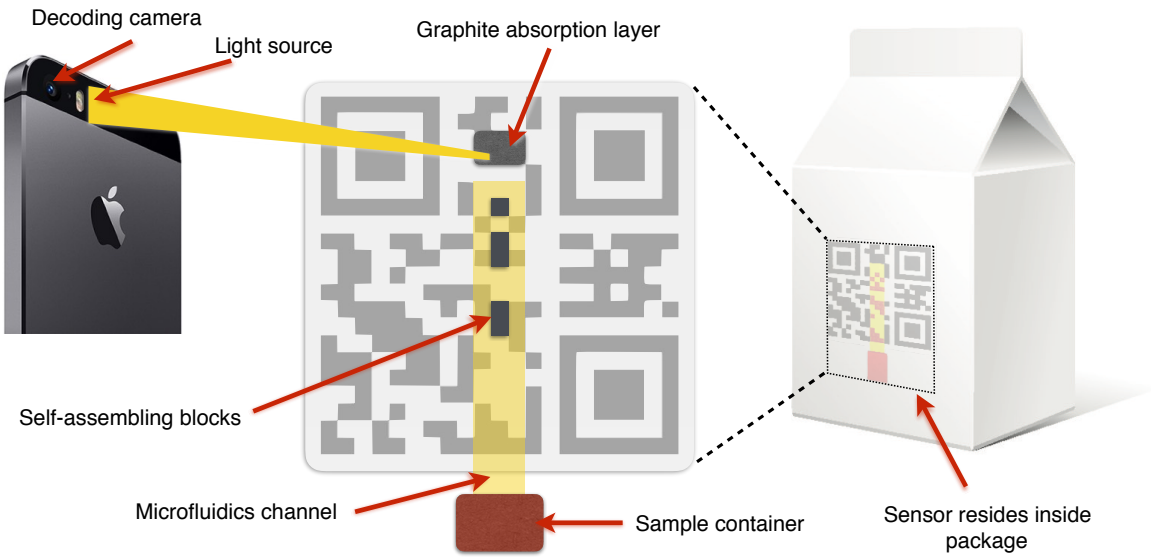

Figure 5.1: Different components of a QR code biosensor that can be integrated on a liquid package and the sample acquisition could be triggered using a smart-phone based light source.

5.1 Introduction

Paper-based microfluidics provide an ultra-low cost platform to implement biosensors for portable point-of-care (POC) diagnostics and on-site detection [93, 94] with applications ranging from immunoassays [25], urinalysis [66], environmental monitoring [65] to food safety [40]. In most of these applications, the process of sampling the analyte involves physically applying the reagent (using a pipette or a dipstick [36]) to the paper substrate. While this approach is convenient for cases when the analyte can be directly accessed, it is impractical for cases when the analyte is packaged or sealed. This scenario shows up in medical and food supply-chain applications (as shown in Fig. 5.1) where there exists a need to monitor the quality of the product at every point of the supply-chain. However, monitoring at every point in the product supply-chain could be overwhelming due to the volume and rate of the products and the due to the detrimental effects of false-positives. We had presented two wireless monitoring approaches for food supply-chain in the previous chapters: (a) a passive

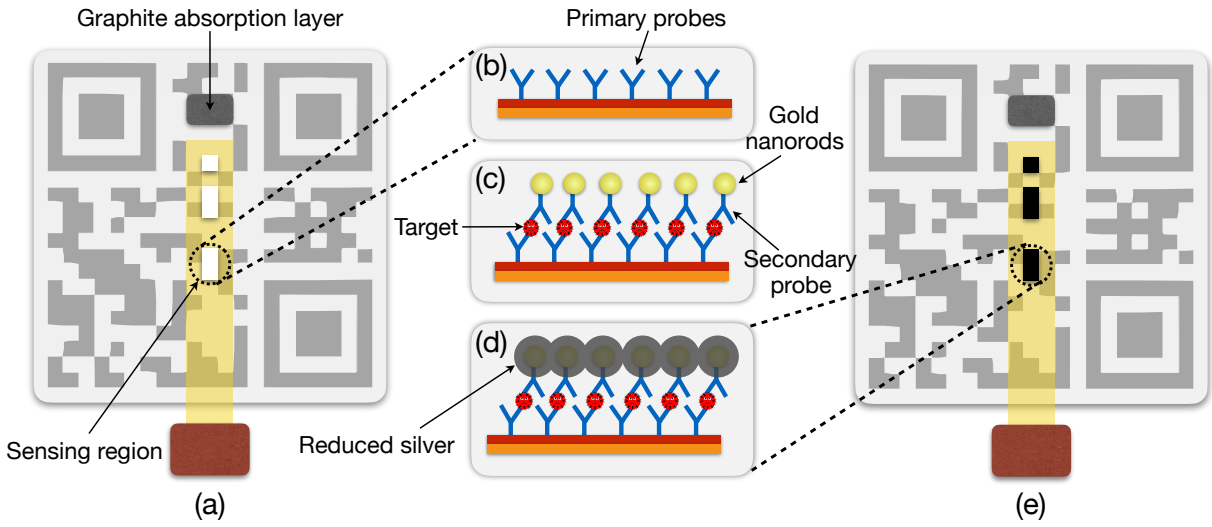

Figure 5.2: Principle of QR code self-assembly and biosensing using silver enhancement. (a) QR code sensor before target detection; (b) primary probes specific to the target analytes immobilized in the sensing regions; (c) target analytes captured on primary probes; (d) silver enhancement technique used to assemble the parts of the QR code as shown in (e).

radio frequency identification (RFID) tag based biosensor which can be interrogated with a standard RFID reader; and (b) a paper-based QR-code biosensor which can be used not only to encode the product information, but also can be used for encoding and decoding the process of analyte monitoring. The decoding of both RFID biosensor and QR code biosensor can be performed using a smart-phone, either by using the in-built RFID read-out capability or by using the in-built camera. In this manner it was envisioned that end-to-end supply-chain monitoring could be crowd-sourced to consumers equipped with only a smart-phone, as shown in Fig. 5.1.

The principle of QR code biosensor based on silver-enhancement self-assembly has been described in chapter 3 and is summarized here and in Fig. 5.2 for the sake of completeness. A QR code is a two dimensional bar-code that encodes the product information along with an in-built error-correcting and alignment capability. When some of the QR code components are missing (highlighted by white modules in Fig. 5.2(a)), the product information cannot

be successfully retrieved. In [105] we self-assemble the modules using a process of silver-enhancement in the sensing regions as shown in Fig. 5.2. Silver enhancement based analyte detection relies on the formation of a sandwich structure comprising of primary probe (e.g. antibodies), target analyte and gold nanorod (AuNR) conjugated secondary probe. The AuNR conjugated secondary probes first hybridize with their target analytes which then bind with the primary probes that are immobilized in the sensing regions, as shown in Fig. 5.2(c). Any unbounded secondary probes are washed away leaving the sandwich structure (with AuNR label) intact. Because the dimensions of AuNRs are in a scale of nanometers, they are not large enough to be optically visible. When the silver enhancement solution is applied, silver ions start reducing into metallic silver on the surface of AuNRs, as shown in Fig. 5.2(d). As time progresses, more silver ions are reduced and deposited, and a chain of AuNRs cored silver micro-structures assemble. Thus, the regions where the silver-enhancement occurs become darker, illustrated in Fig. 5.2(e). In this way, an invalid QR codeword (Fig. 5.2(a)) transits into a valid codeword (Fig. 5.2(e)) which can be successfully decoded using a standard smartphone. We have previously verified in Chapter 3 and Chapter 4 that longer time is needed to assemble a valid QR code to detect target analyte with low concentration levels.

5.2 Light-triggered analyte sampling principle

In this chapter we use a light-absorbing material to induce thermal gradients across the microfluidic channel which can be used to remotely trigger the process of analyte sampling. The operating principle is shown in Fig. 5.3, where microfluidics channel region is surrounded by hydrophobic material to prevent the analyte sample from leaking. One end of the substrate is kept in contact with the analyte sample and the heat is applied to the other end where a graphite-based heating layer is patterned. Graphite can be easily patterned on paper (using a standard pencil), which follows our previous work on ultra-low-cost fabrication of QR code

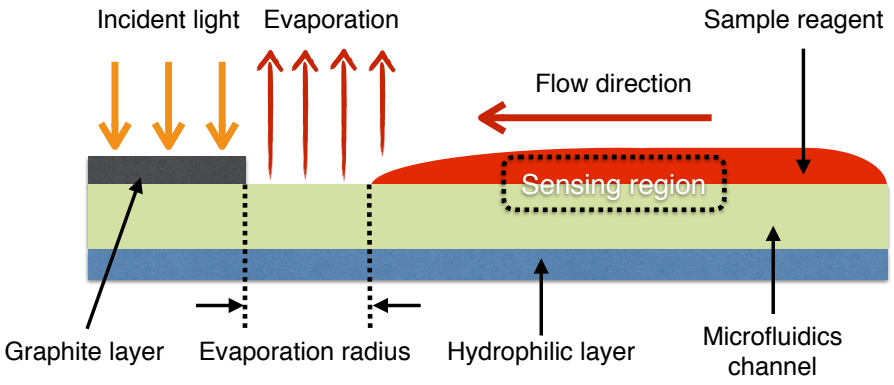

Figure 5.3: Principle of light triggered analyte sampling process.

biosensor, as summarized in Fig. 5.3. The resulting thermal gradient produces an increased rate of evaporation on one end of the substrate. This in turn produces a concentration gradient across the substrate which then triggers the flow of analytes to targeted regions. Analyte detection regions and regions for silver-enhancement self-assembly can be designed in the channel area where the flow of the target samples can be directed.

5.3 Prototype fabrication

The fabrication process of the proof-of-concept prototype verifying the proposed approach of sample acquisition process is shown in Fig. 5.4. A regular laboratory Whatman filter paper with size of 2cm×3.5cm was chosen as the substrate, as shown in Fig.5.4 (a). Microfluidics channel area was defined by patterning its surrounding area with hydrophobic layer using Sakura junior artist oil pastels in this case as shown in Fig. 5.4 (b). The substrate was then heated to a temperature of 125°C for 1 minute to allow the wax to penetrate through the filter paper as shown in Fig. 5.4 (c). To prevent the liquid reagent from leaking on the backside of the channel area, another hydrophobic layer was patterned on the backside of the device, as shown in Fig. 5.4 (d). The substrate was then heated again to a temperature of 80°C for 5 seconds (Fig. 5.4 (e)). Optimization of temperature and time is needed to make

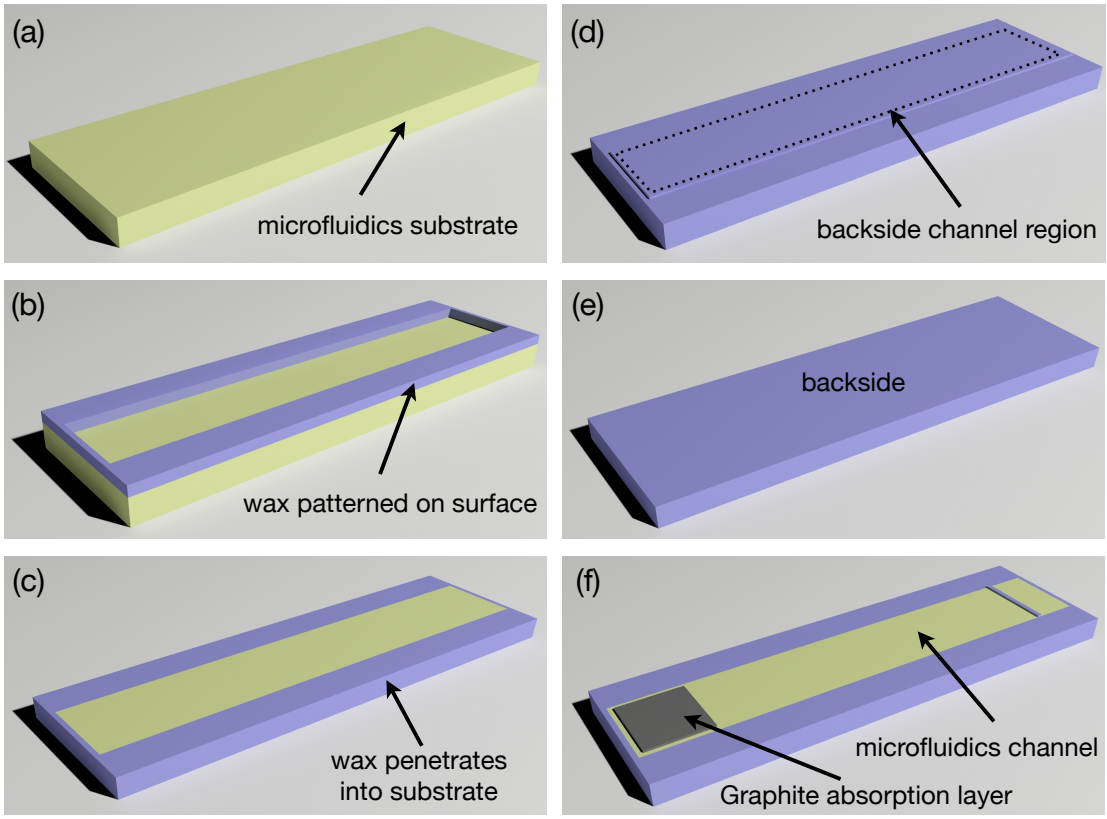

Figure 5.4: Illustration of light triggered reagent sampling prototype fabrication process: (a) filter paper with desired shape and size; (b) patterned with hydrophobic layer on the surface; (c) channel formed by heating at 125°C for 1min; (d) patterned with hydrophobic layer on back side of channel area to prevent reagent from leaking; (e) heated at 80°C for 5sec; (f) graphite layer patterned.

sure that the hydrophobic layer patterned in (d) only penetrates into a very thin layer on the backside of filter paper. Otherwise, the front side of microfluidics area will be blocked such that analyte cannot flow freely. The final step is to pattern a graphite layer that can efficiently absorbs light and convert it into heat on the front side as shown in Fig. 5.4 (f). Graphite used in our experiment is patterned by rubbing a standard pencil on the filter paper substrate.

The top view of a fully assembled prototype is shown in Fig. 5.5 (b). The laser system that is used to heat the graphite layer is shown in Fig. 5.6 which includes laser control unit, laser

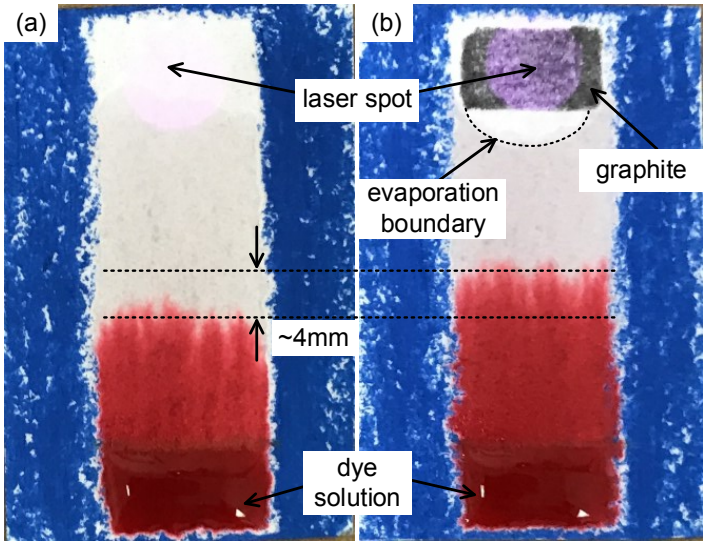

Figure 5.5: Comparison of penetration lengths achieved by the dye solution in prototypes (a) without and (b) with graphite heating layer, 5 min after the solution was applied.

module and the laser head. 808nm laser is emitted from the laser head and focused on the heating layer of the microfluidics channel. Distance between the laser head and heating layer is adjusted so that 300mW IR is received at the heating layer position. Note that IR laser is used in this experiment for the sake of simplicity of experimental implementation.

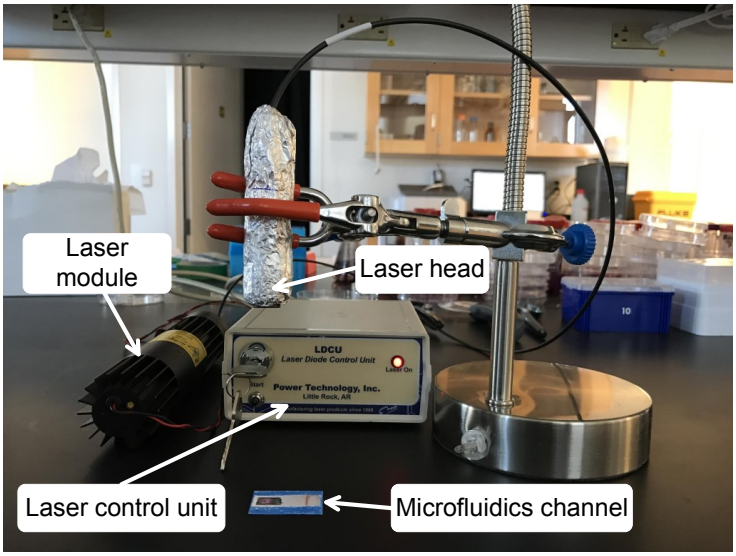

Figure 5.6: Experimental setup showing the infrared laser light source.

5.4 Measurement results

To verify the proposed hypothesis of analyte sampling triggered by light, two microfluidics channels were fabricated using the method reported in section 5.3. For control only one of the channels was patterned with a graphite heating layer as shown in Fig. 5.5 (a) and (b). For the purpose of visualization, a red dye solution was used as a sample analyte. The surrounding areas which are colored in blue are the patterned hydrophobic layers. In order to demonstrate the effects of light on the reagent flow rate, 50μL DI water was initially applied at the bottom area on both (a) and (b). The flow of the water was driven by the capillary force of the filter paper pores. As a result the water completely fills up the channel as time progresses. A beam of 300mW 808nm laser was focused on the laser spot area labeled in Fig. 5.5 for both cases (with and without heating layer) to create a concentration gradient. Then, a 50μL red dye solution is applied at the bottom area of the channel to visualize the effect of graphite based IR absorption. Photos in Fig. 5.5 are taken 5min after dye solution applied for both cases. For the microfluidics channel with graphite heating layer, the dye solution front

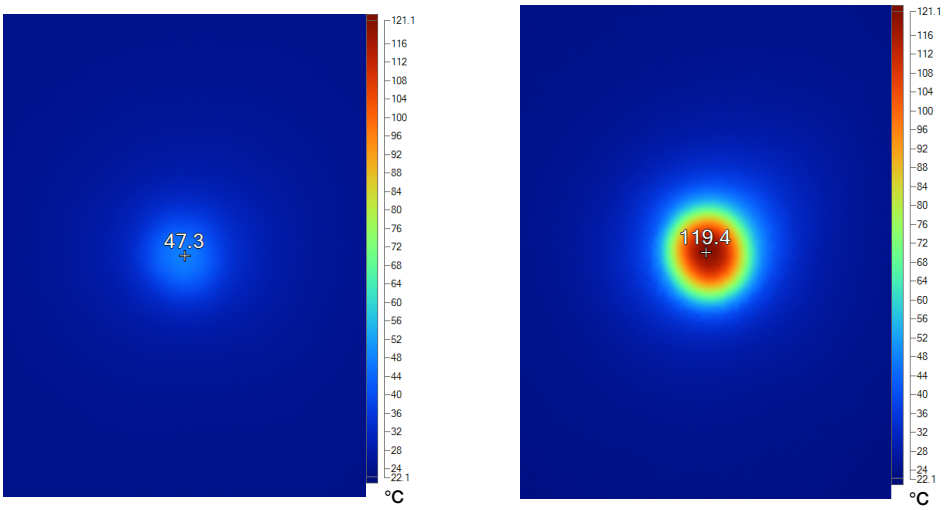

(a) without graphite heating layer (b) with graphite heating layer

Figure 5.7: Thermal images of the devices (a) without and (b) with graphite heating layer, when exposed to 300mW 808nm laser.

is 4mm ahead of that on the channel without heating layer after 5min. It means dye solution propagates faster on the microfluidics channel with graphite heating layer. Graphite layer patterned on filter paper converts light into heat more efficiently, which in turn facilitates liquid sample evaporation in its adjacent area. A sample concentration gradient is induced because liquid evaporates faster in the area close to the heating layer as we talked in section 5.1. A higher reagent flow rate is achieved due to this concentration gradient.

Photos in Fig. 5.7 show temperature differences of the laser spot when a beam of 300mW 808nm IR laser is focused on (a) regular Whatman filter paper and (b) filter paper coated with graphite layer at room temperature. Images are taken using a Fluke Ti100 Uncooled Microbolometer. A 70°C temperature increase (from 50°C to 120°C) is measured on the graphite coated filter paper compared to that on the regular filter paper. Measured temperature on graphite coated filter paper is much higher than boiling point of water at sea level. It is also shown in Fig. 5.5 (b) where the dashed line labeled as “evaporation boundary” indicates the water boiling temperature. We refer this distance between this boundary and

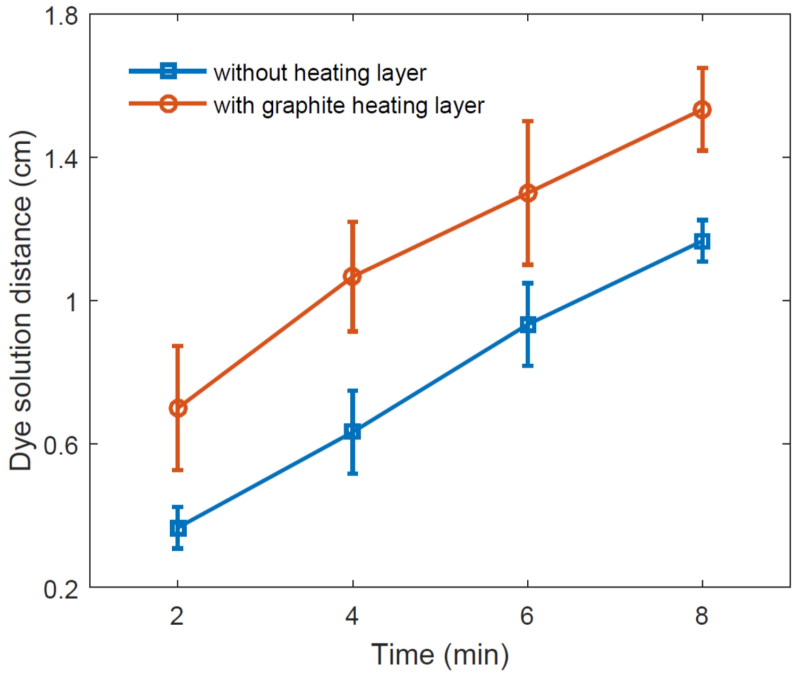

Figure 5.8: Comparison of dye solution flow-rates without and with graphite heating layer.

the heating layer as "evaporation radius", as labeled in Fig. 5.3. Water evaporates quickly once it reaches this boundary as it propagates on the microfluidics channel, which results in the liquid concentration gradient. The measured dye solution flow rates for cases with and without heating layer are shown in Fig. 5.8. The prototype with graphite heating layer provides a higher flow rate for dye solution, which validates our proposed approach.

5.5 Summary and discussion

In this chapter we have proposed a novel approach for automatic analyte sampling which can be triggered using a light source. The microfluidics sampling channel is formed based on a low-cost laboratory filter paper using a hydrophobic blocking method. A graphite heating layer is patterned on one end of the channel and is used for creating thermal gradient and hence concentration gradients when exposed to a light source. While the proof-of-concept

operation was demonstrated using a 300mW 808nm laser source in this paper, a more practical choice would be to use light sources already available on smart-phones. However, the intensity of the smartphone LED light source might be too weak to trigger analyte sampling using the current prototype implementation. Fortunately, the following two methods could be used to boost the efficiency of sampling, which could be part of the future work: (a) engineer heating material (e.g. nanoparticles [15, 28], metamaterials [33], or polydopamine [39]) with high absorption characteristics to the smartphone LED light spectrum; or (b) use a lensing scheme to focus the LED light (e.g. F. Lens [52]) onto the graphite layer.

Chapter 6

XNOR Biomolecular Logic Gate Construction

In previous chapters, we have successfully verified a biosensing approach which is to "grow" parts of an RFID antenna or a QR code-word. Both the RFID-based biosensor and QR code-based biosensor shown in previous chapters are designed for a single target analyte detection. One challenge needs to be addressed before deploying them in the field is the capability of multi-analyte detection since the product can be contaminated by any food-borne pathogen (or even a combination of them), and people would not know that beforehand. Although the most straight forward approach is to embed a bunch of biosensors which can be designed specific to different pathogens on the food product, it would be cumbersome and expensive since the number of tags or QR codes needed increases proportionally with respect to the number of analytes of interest. However, if we can build different Boolean logic gates directly during the target analyte detection process, we can construct more sophisticated code-word (equivalent to a more advanced circuit) that can be use for multi-analyte detection using a single RFID tag or a single QR code. In this chapter, we are trying to construct a

biomolecular XNOR logic gate. A hypothetical operating principle is illustrated in detail, and we have also designed some experiments to verify this hypothesis.

6.1 Introduction

Rapid progress in the field of bio-molecular logic systems over the last decades provides an alternate approach for unconventional computation [41]. There is a possibility to break limits due to silicon based technologies by implementing logic computation system directly with these fundamental bio-molecular blocks [42]. Researchers have constructed series of relatively simple Boolean gates (e.g. AND [7, 56], OR [60, 82], NOR [107], and so on). Many more sophisticated bio-molecular based logic circuits and systems – adder, substractor, multiplexer, demultiplexer, encoder and decoder to name a few, have also been formed by assembling these individual fundamental building blocks [21, 53].

Our research group made some efforts by applying forward error correction (FEC) technique to the biosensor field to improve biosensors' reliability [58, 61]. FEC is a technique that has been extensively used to design ultra-reliable communication and storage systems. The basic idea is to add sufficient redundancy during the encoding process such that decoder can successfully decipher the transmitted messages using this redundancy even when communication channel is noisy. In the biosensor settings, channel noise can be attributed to the artifacts, such as non-specific biomolecular bindings, sensor defects, and environmental artifacts. Biosensor reliability is crucially important in the sensor design, especially for detecting some specific pathogens at low concentration levels. For instance, the infectious dose of *E. coli* O157:H7 for human is less than 10 cells [30]. As more redundant biomolecular circuit elements are integrated on the biosensor, a higher fault tolerance is expected. Theoretically, a near perfect reliability can be achieved by adding sufficient FEC capabilities with the biosensors. Liu

Table 6.1: Truth Table of A XNOR B

Input A	Input B	A XNOR B
0	0	1
0	1	0
1	0	0
1	1	1

[61] has constructed two fundamental logic gates, AND gate and OR gate, by patterning different bio-molecular probes in different locations of the biosensor substrate. Significant improvement in the analyte detection reliability has been demonstrated using a "co-detection" principle based on the soft-logic circuits using these two logic gates [61]. XOR gates are useful fundamental logic functions for many circuit modules. For instance, many popular code, Hamming code as an example, is based on the XOR logic function. Unfortunately, compared to many others (e.g. AND gate, OR gate), XOR gate is more difficult to construct using biomolecular interactions. Liu stated in his thesis: "XOR logic may be difficult or even impossible to achieve in biosensors due to the structure or principle constraints… [58]".

In this chapter, we proposed a hypothesis that theoretically functions as an XNOR (simply inverse of XOR) gate in the two-target analytes detection process. We first describe the proposed operating principle for XNOR gate construction. It is then followed with some experiments designed to verify this hypothesis. Unfortunately, it is demonstrated that some key assumptions made at the very early stage are invalid, which make it does not work out as expected.

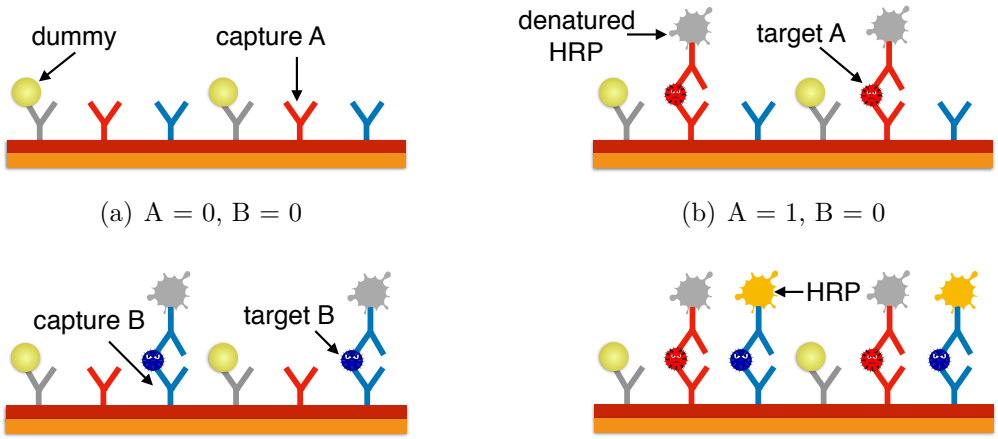

(a) A = 0, B = 0

(b) A = 1, B = 0

(c) A = 0, B = 1

(d) A = 1, B = 1

Figure 6.1: Hypothetical operating principle of our proposed XNOR logic gate.

6.2 Hypothetical operating principle

Table 6.1 is the truth table of a two-input version XNOR gate. The table indicates that a 0 output is produced in the case where if and only if one target analyte exists and is detected. Otherwise, a 1 will be generated if both inputs to the gate are the same. In this proposed biomolecular logical gate design, the target analytes to be analyzed are the inputs to the XNOR gate. Logic input 0 is defined as the absence of the target analyte, whereas logic input 1 is the case where target analyte concentration is significantly higher than zero. Output (0 or 1) of XNOR gate is determined by the colorimetric measurement result.

The hypothetical operating principle to construct a XNOR gate is illustrated in Fig. 6.1. Two target specific primary probes are first immobilized on a substrate which are labeled as *capture A* and *capture B* in Fig. 6.1. *Capture A* probe binds only to *target A*. Similarly, *capture B* is only specific to *target B*. The detection principle is similar to the traditional "sandwich" immunoassay where any unbound materials are washed away. When a solution of secondary probe is applied, a sandwich structure will be formed in the presence of target

analyte. Horseradish peroxidase (HRP) is conjugated to the secondary probe as reporter enzyme in this case.

Except for immobilizing two target specific primary probes on the substrate, a dummy unit, a gold nanoparticle (AuNP) labeled probe, is also immobilized on the substrate as shown in Fig. 6.1(a). The purpose of adding this dummy unit is to produce a high output in the absence of both *target A* and *target B* (or equivalently, A = 0, B = 0). During colorimetric development, silver enhancement solution will be first applied followed by the addition of HRP substrate. In the absence of both *target A* and *target B* as shown in Fig. 6.1(a), silver deposition will occur on the surface of AuNPs due to the silver enhancement process described in Chapter 2 and Chapter 3. It will result in a higher spectrum absorbance as the particle size increases monotonically with respect to the time, which is considered as a high output (output = 1).

In the case of if and only if one target analyte exists in the sample, either A = 1 and B = 0 (shown in Fig. 6.1(b)) or A = 0 and B = 1 (shown in Fig. 6.1(c)), silver enhancement solution is also first applied according to previously mentioned detection protocol. Different from previous case where silver ions are reduced into metallic form on the surface of AuNPs, we hypothesize silver nitrate will first denature HRP enzyme by disrupting salt bridges in proteins according to [72]. According to the same literature, an insoluble metal protein salt is typically generated due to the denaturing reaction between heavy metal salt and protein. We assume that Ag^+ involved in the HRP denaturation will cease to function for the silver deposition. By carefully tuning the amount of silver enhancement reagent to be applied, all the applied silver nitrate can be consumed due to HRP denaturation. With this assumption in mind, there will be no positive colorimetric detection results due to silver enhancement process since there is no excess reagent remaining for silver deposition. In the meantime, all the HRPs (corresponding to certain amount of the target analyte) are denatured and lose their enzymatic activity (depicted in gray color in Fig. 6.1). Negative detection result

(low spectrum absorption value) is then expected due to HRP denaturation. As a result, a low output (output = 0) can be produced if and only if one target analyte is present in the sample.

For the case where both *target A* and *target B* are present in the sample, two types of sandwich structures will be formed as shown in Fig. 6.1(d). Detection protocol remain the same and HRP will also be denatured when silver enhancement reagent is introduced. Fortunately, the system in this case has twice amount of HRP compared to the scenario with only one target analyte (shown in Fig. 6.1(b) or Fig. 6.1(c)). Only half HRP will be denatured if the amount of applied silver enhancement reagent is the same as scenario shown in Fig. 6.1(b) or Fig. 6.1(c). As a result, a high output (output = 1) can be generated due to the remaining half HRP when its substrate is applied.

6.3 Takeaway and discussions

To verify our proposed hypothesis in section 6.2, we have had lots of discussions and have run many experiments. For the sake of brevity, some results have been included in the appendix of this dissertation as supporting information. It can be noticed from the operating principle described in section 6.2 that one of the keys facilitating our proposed approach is that $AgNO_3$ contained in the silver enhancement reagent will denature HRP. We take this for granted in our experiment design. *Unfortunately, we found out that silver nitrate does not denature HRP or degrade its enzymatic activity after spending time and efforts on other experiments without verifying it at the very beginning.* It is the direct reason why the proposed bio-molecular based XNOR gate does not work out as expected.

Measurements in Fig. 6.2 show the effect of silver enhancer of different dilution factors on colorimetric measurement, and were collected according to a normal KIM-1 ELISA procedure.

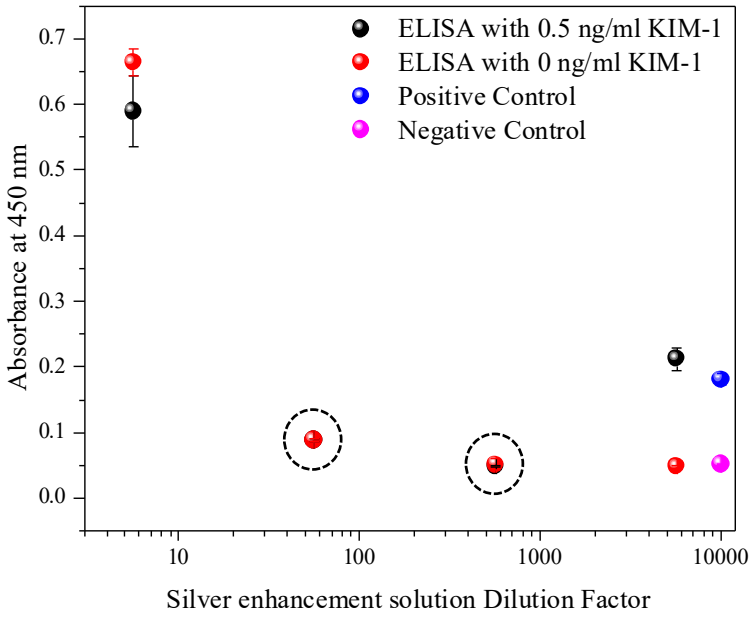

Figure 6.2: Absorbance of the solution at 450nm with respect to different silver enhancer dilution factors.

Target molecules with a concentration of 0.5 ng/ml were used in the experiment, and no target molecules were used in the control, shown in Fig. A.2 in Appendix. After adding streptavidin-HRP at the final step, it was then followed with PBS buffer wash for 3 times and DI water wash twice. The purpose of DI water washing is to remove salts contained in PBS buffer which have been proved to have an effect on the experiment outcomes (more information in Appendix A). All water inside the wells was then removed. A freshly prepared solution mixer, containing silver enhancer, AuNRs and H_2O, has been applied to each well. Silver enhancer reagent is prepared with different dilution factors ranging from 1.0X to 6,000X (shown in Fig. A.2 in Appendix). It was followed with applying HRP substrate, tetramethylbenzidine (TMB), for color development. Spectrum absorbance plot of the solution with respect to silver enhancer of different dilution factors is shown in Fig. 6.2, and visual assessment photo is shown in Fig. A.2.

It is easy to interpret high absorbance values under two extreme scenarios (excess silver enhancer and excess HRP) as shown in Fig. 6.2. For the case where excess silver enhancer reagent exists in the the well (1.0X and 5.6X diluted SEA/SEB in Fig. A.2), high absorbance is due to silver deposition as we described in previous chapters. For the case where silver enhancement reagent is extremely diluted (5667X diluted SEA/SEB in Fig. A.2), the developed color is caused by the reaction between HRP and its substrate. The region that interests us is in between these two extreme cases (dilution factors of 56X and 567X) where our proposed XNOR gate can operate according to the operating principle introduced in section 6.2. However, the measured absorbance for the case with target molecules is the same as that without target molecules, which is circled with dashed line in Fig. 6.2(a). If the assumption we made is valid, two different absorbance values are then expected. For the case of normal ELISA with target molecules, part of the applied $AgNO_3$ will be used to denature HRP. For the control experiment (without target molecules), all the applied $AgNO_3$ will participate in silver reduction due to the absence of target molecules (hence no HRP). We began to realize that something might be wrong with our assumption after seeing this experiment result.

Silver nitrate of different concentrations has been applied to HRP to investigate its effect on HRP activity. 100μl $AgNO_3$ of each concentration (ranging from 2nM to 2mM) was mixed with 15μl HRP. HRP solution was prepared at a fixed concentration of 1.26nM with DI H_2O. The mixture is then followed by adding HRP substrate, TMB, for color development. Fig. A.1 (Appendix A) is a photograph showing colorimetric response when $AgNO_3$ of different concentrations are applied, and no significant difference can be observed from visual assessment. A measured spectrum absorbance plot with respect to different $AgNO_3$ concentrations is shown in Fig. 6.3. Little changes for the measured absorbance values can be seen as $AgNO_3$ concentration varies. Even though the concentration of applied $AgNO_3$

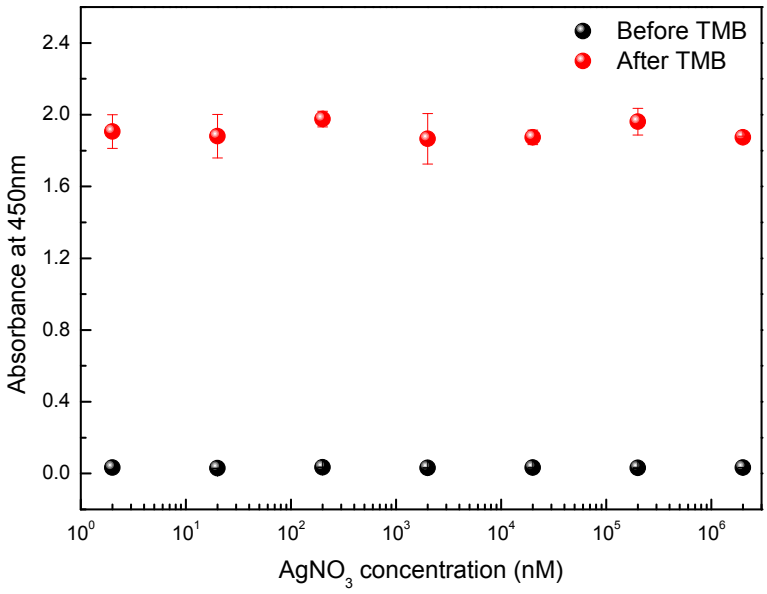

Figure 6.3: Absorbance of the solution at 450nm with respect to different silver nitrate concentrations showing it effect on colorimetric measurement.

increases from 2nM to 2mM, measured absorbance value remains almost unchanged at around a value of 2.0. This result demonstrates that silver nitrate does not denature the activity of HRP, which shows the key assumption made in section 6.2 is invalid.

In the remaining part of this section, I would like to explain how we come up with this hypothesis without confirming the effect of silver nitrate on HRP directly at very beginning. First and foremost, it is widely known that protein can be denatured in quite a few ways – heat, X-ray, acids, alkalies and salts of heavy metals to name a few [72]. Silver nitrate, one of the heavy metal salts, is reported to readily interact with proteins and denature enzymes [48]. Strong bonds with carboxylate anions of the acidic amino acids or SH groups of cysteine is formed to disrupt salt bridges in the protein as it is denatured by the heavy metal ions [72]. As a result, we presume HRP will be denatured by silver nitrate at the very early stage since it is a protein.

Secondly, with that assumption in mind, we designed a few experiments to verify the proposed hypothesis. Unfortunately, the collected data from these designed experiments is very misleading. Although I am not planning to detail each one of them here, it is worth to point out that among all the factors, the effect of PBS (composed of a variety of salts, such as NaCl, KCl, Na_2HPO_4, KH_2PO_4) has been neglected. It has been found out later that PBS is one of the most important factor that resulted in many of these misleading results. More information about this part is included in the Appendix A.

The complication of our experimental system is another reason that we didn't find it out earlier, since too many chemical reagents have been involved. It became extremely difficult to figure out the reason behind everything when the designed system is composed of a variety of chemical and biological components.

Chapter 7

Conclusions and Future Work

7.1 Summary

The ultimate goal of this research is to provide an alternative approach for the end-to-end food supply chain monitoring to prevent food-borne disease outbreaks. In this dissertation we investigate a wireless biosensing paradigm of "growing" transducer structures which is triggered only when analytes of interest are present in the sample. At the core of this self-assembly is a silver enhancement technique where silver ions reduce into metallic form in the presence of target analyte, which in turn leads to changes in electrical or optical property. First, we demonstrate an RFID tag based biosensor by exploiting electrical property change due to silver enhancement. A chain of micromonopole antennas is assembled in the presence of target analyte during the detection. This self-assembly process directly modulates the impedance matching between the antenna and the silicon chip of the RFID tag, and hence results in an improvement antenna's reflection efficiency. Second, we show a QR code based biosensor whose operating principle relies on the optical property changes also resulting from

silver enhancement. Target detection process assembles an invalid QR code into a valid QR code that can be further decoded with a standard smartphone. Third, since the biosensors will be embedded inside the food packages and no active power sources are available on these passive devices, it is challenging for these sensors (RFID based and QR code based) to reliably perform sample acquisition and pre-process. Paper-based microfluidics have been explored in this dissertation to provide a self-powered approach for sample processing. Lastly, graphite's thermal absorption properties have been explored to drive analyte sampling process on paper-based biosensors by creating a thermal gradient on the microfluidics channel. Based on this, one use case is to trigger the analyte detection process remotely by an end user by shining a beam of light on the biosensor.

7.2 Future directions

Except for the future work related to each theme that has already been pointed out in reach chapter, I would like to point out some additional future directions that have not be mentioned:

- Although the integration of paper-based microfluidics with biosensors (for both QR code based and RFID based) has been shown in this dissertation, all the sensor components should be packaged or sealed properly because the whole sensor is envisioned to be embedded inside the food package. In that scenario, the packaged biosensor will have a direct contact with food. In that sense, the biosensor should be packaged in a way such that sensor can continuously and slowly sample target analyte. In the meantime, no waste should leak out from the sensor package. Otherwise, food will get contaminated by the reagents contained in the biosensor.

- This dissertation mainly focuses on verifying the concept of analyte detection by "growing" sensor structures without too much emphasis on the details of target analytes. In this dissertation, rabbit IgG is used as the model target to verify our proposed sensing approach. Real pathogenic analyte of interest should be tested using the same sensing paradigm before deploying them in the field. All the optimizations and calibrations should also be performed to the specific target analyte accordingly.

- For the sake of simplicity, rabbit IgG has been used as the single model target in this dissertation to show the proof-of-concept. The capability to detect multiple analytes is also very important, since food can be contaminated by any food-borne pathogen (or even a combination of them), and people would not know that beforehand.

- The biosensor should be designed sufficiently robust such that it can survive from harsh real world operating environment. For instance, it should have a shelf life comparable to that of the product to be monitored. Another example is that the associated mechanical vibration in the supply chain should not impair or deteriorate the functionality of the biosensor.

References

[1] Muhammad Mustafa Abeer, Mohd Amin, Mohd Cairul Iqbal, and Claire Martin. "A review of bacterial cellulose-based drug delivery systems: their biochemistry, current approaches and future prospects". In: *Journal of Pharmacy and Pharmacology* 66.8 (2014), pp. 1047–1061.

[2] *Alien Technology Higgs-3 ALN-9640 Squiggle Inlay*. 2014. URL: `http://www.alientechnology.com/wp-content/uploads/Alien-Technology-Higgs-3-ALN-9640-Squiggle.pdf`.

[3] Rebecca Angeles. "RFID technologies: supply-chain applications and implementation issues". In: *Information Systems Management* 22.1 (2005), pp. 51–65.

[4] Kenji Aono, Nizar Lajnef, Fred Faridazar, and Shantanu Chakrabartty. "Infrastructural health monitoring using self-powered Internet-of-Things". In: *Circuits and Systems (ISCAS), 2016 IEEE International Symposium on*. IEEE. 2016, pp. 2058–2061.

[5] Siamak Aram, Amedeo Troiano, and Eros Pasero. "Environment sensing using smartphone". In: *Sensors Applications Symposium (SAS), 2012 IEEE*. IEEE. 2012, pp. 1–4.

[6] Grocery Manufacturers Association et al. "Capturing recall costs: measuring and recovering the losses". In: *The Association of Food, Beverage and Consumer Products Companies* (2011).

[7] Saira Bakshi, Oleksandr Zavalov, Jan Halámek, Vladimir Privman, and Evgeny Katz. "Modularity of biochemical filtering for inducing sigmoid response in both inputs in an enzymatic AND gate". In: *The Journal of Physical Chemistry B* 117.34 (2013), pp. 9857–9865.

[8] Michael Batz, Sandra Hoffmann, and J Glenn Morris Jr. "Disease-outcome trees, EQ-5D scores, and estimated annual losses of quality-adjusted life years (QALYs) for 14 foodborne pathogens in the United States". In: *Foodborne pathogens and disease* 11.5 (2014), pp. 395–402.

[9] *Burden of Foodborne Illness: Findings*. URL: `https://www.cdc.gov/foodborneburden/2011-foodborne-estimates.html`.

[10] Santiago Capdevila, Lluis Jofre, J-C Bolomey, and Jordi Romeu. "RFID multiprobe impedance-based sensors". In: *Instrumentation and Measurement, IEEE Transactions on* 59.12 (2010), pp. 3093–3101.

[11] Yu-Hsuan Chang, Chung-Hua Chu, and Ming-Syan Chen. "A General Scheme for Extracting QR Code from a non-uniform background in Camera Phones and Applications". In: *Multimedia, 2007. ISM 2007. Ninth IEEE International Symposium on*. IEEE. 2007, pp. 123–130.

[12] Kihun Chang, Yong-Ho Kim, Yong-Jun Kim, and Young Joong Yoon. "Functional antenna integrated with relative humidity sensor using synthesised polyimide for passive RFID sensing". In: *Electronics letters* 43.5 (2007), pp. 259–260.

[13] Jane Ru Choi et al. "An integrated paper-based sample-to-answer biosensor for nucleic acid testing at the point of care". In: *Lab on a Chip* 16.3 (2016), pp. 611–621.

[14] Stefano Cinti, Clarissa Minotti, Danila Moscone, Giuseppe Palleschi, and Fabiana Arduini. "Fully integrated ready-to-use paper-based electrochemical biosensor to detect nerve agents". In: *Biosensors and Bioelectronics* 93 (2017), pp. 46–51.

[15] Eduardo A Coronado, Ezequiel R Encina, and Fernando D Stefani. "Optical properties of metallic nanoparticles: manipulating light, heat and forces at the nanoscale". In: *Nanoscale* 3.10 (2011), pp. 4042–4059.

[16] *Cost Estimates of Foodborne Illnesses*. URL: `https://www.ers.usda.gov/data-products/cost-estimates-of-foodborne-illnesses/`.

[17] Dieter Croux et al. "Molecular imprinted polymer films on RFID tags: a first step towards disposable packaging sensors". In: *physica status solidi (a)* 210.5 (2013), pp. 938–944.

[18] Robert D Deegan, Olgica Bakajin, Todd F Dupont, Greb Huber, Sidney R Nagel, and Thomas A Witten. "Capillary flow as the cause of ring stains from dried liquid drops". In: *Nature* 389.6653 (1997), pp. 827–829.

[19] Wijitar Dungchai, Orawon Chailapakul, and Charles S Henry. "Electrochemical detection for paper-based microfluidics". In: *Analytical chemistry* 81.14 (2009), pp. 5821–5826.

[20] *EPC Radio-Frequency Identity Protocols Generation-2 UHF RFID*. 2015. URL: `https://www.gs1.org/sites/default/files/docs/epc/Gen2_Protocol_Standard.pdf`.

[21] Daoqing Fan, Jinbo Zhu, Yaqing Liu, Erkang Wang, and Shaojun Dong. "Label-free and enzyme-free platform for the construction of advanced DNA logic devices based on the assembly of graphene oxide and DNA-templated AgNCs". In: *Nanoscale* 8.6 (2016), pp. 3834–3840.

[22] Steve Feng, Romain Caire, Bingen Cortazar, Mehmet Turan, Andrew Wong, and Aydogan Ozcan. "Immunochromatographic diagnostic test analysis using Google Glass". In: *ACS nano* 8.3 (2014), pp. 3069–3079.

[23] Gilbert B Forbes and Grace M Forbes. "Silver nitrate and the eyes of the newborn: Crede's contribution to preventive medicine". In: *American journal of diseases of children* 121.1 (1971), pp. 1–4.

[24] B Foultier, L Moreno-Hagelsieb, D Flandre, and J Remacle. "Comparison of DNA detection methods using nanoparticles and silver enhancement". In: *Nanobiotechnology, IEE Proceedings*. Vol. 152. 1. IET. 2005, pp. 3–12.

[25] Lei Ge, Shoumei Wang, Xianrang Song, Shenguang Ge, and Jinghua Yu. "3D origami-based multifunction-integrated immunodevice: low-cost and multiplexed sandwich chemiluminescence immunoassay on microfluidic paper-based analytical device". In: *Lab on a Chip* 12.17 (2012), pp. 3150–3158.

[26] *Global Smartphone Market Analysis and Outlook: Disruption in a Changing Market*. URL: `http://www.lenovo.com/transactions/pdf/CCS-Insight-Smartphone-Market-Analysis-Full-Report-07-2014.pdf`.

[27] Anand Gole and Catherine J Murphy. "Azide-derivatized gold nanorods: functional materials for "click" chemistry". In: *Langmuir* 24.1 (2008), pp. 266–272.

[28] Alexander O Govorov and Hugh H Richardson. "Generating heat with metal nanoparticles". In: *Nano today* 2.1 (2007), pp. 30–38.

[29] Mathew J Gregoski, Martina Mueller, Alexey Vertegel, Aleksey Shaporev, Brenda B Jackson, Ronja M Frenzel, Sara M Sprehn, and Frank A Treiber. "Development and validation of a smartphone heart rate acquisition application for health promotion and wellness telehealth applications". In: *International journal of telemedicine and applications* 2012 (2012), p. 1.

[30] Judy D Greig, Ewen CD Todd, C Bartleson, and B Michaels. "Infective doses and pathogen carriage". In: *Food Safety Education Conference, Atlanta, Georgia*. 2010.

[31] Ming Gu and Shantanu Chakrabartty. "An adaptive analog low-density parity-check decoder based on margin propagation". In: *Circuits and Systems (ISCAS), 2011 IEEE International Symposium on*. IEEE. 2011, pp. 1315–1318.

[32] Sangkwon Han, Hyung Jong Bae, Junhoi Kim, Sunghwan Shin, Sung-Eun Choi, Sung Hoon Lee, Sunghoon Kwon, and Wook Park. "Lithographically Encoded Polymer Microtaggant Using High-Capacity and Error-Correctable QR Code for Anti-Counterfeiting of Drugs". In: *Advanced Materials* 24.44 (2012), pp. 5924–5929.

[33] Jiaming Hao, Lei Zhou, and Min Qiu. "Nearly total absorption of light and heat generation by plasmonic metamaterials". In: *Physical Review B* 83.16 (2011), p. 165107.

[34] Sandra Hoffmann, Michael B Batz, and J Glenn Morris Jr. "Annual cost of illness and quality-adjusted life year losses in the United States due to 14 foodborne pathogens". In: *Journal of food protection* 75.7 (2012), pp. 1292–1302.

[35] Hua Hu and Ronald G Larson. "Evaporation of a sessile droplet on a substrate". In: *The Journal of Physical Chemistry B* 106.6 (2002), pp. 1334–1344.

[36] Jie Hu, ShuQi Wang, Lin Wang, Fei Li, Belinda Pingguan-Murphy, Tian Jian Lu, and Feng Xu. "Advances in paper-based point-of-care diagnostics". In: *Biosensors and Bioelectronics* 54 (2014), pp. 585–597.

[37] Xiaohua Huang, Svetlana Neretina, and Mostafa A El-Sayed. "Gold nanorods: from synthesis and properties to biological and biomedical applications". In: *Advanced Materials* 21.48 (2009), pp. 4880–4910.

[38] Yi Jia, Michael Heiß, Qiuyun Fu, and Nicolas A Gay. "A prototype RFID humidity sensor for built environment monitoring". In: *Education Technology and Training, 2008. and 2008 International Workshop on Geoscience and Remote Sensing. ETT and GRS 2008. International Workshop on*. Vol. 2. IEEE. 2008, pp. 496–499.

[39] Qisheng Jiang, Hamed Gholami Derami, Deoukchen Ghim, Sisi Cao, Young-Shin Jun, and Srikanth Singamaneni. "Polydopamine-filled bacterial nanocellulose as a biodegradable interfacial photothermal evaporator for highly efficient solar steam generation". In: *Journal of Materials Chemistry A* 5.35 (2017), pp. 18397–18402.

[40] Jana C Jokerst, Jaclyn A Adkins, Bledar Bisha, Mallory M Mentele, Lawrence D Goodridge, and Charles S Henry. "Development of a paper-based analytical device for colorimetric detection of select foodborne pathogens". In: *Analytical chemistry* 84.6 (2012), pp. 2900–2907.

[41] Evgeny Katz. *Biomolecular information processing: from logic systems to smart sensors and actuators*. John Wiley & Sons, 2013.

[42] Evgeny Katz. "Enzyme-Based Logic Gates and Networks with Output Signals Analyzed by Various Methods". In: *ChemPhysChem* 18.13 (2017), pp. 1688–1713.

[43] Hassan Aqeel Khan and Shantanu Chakrabartty. "On the Channel Capacity of High-Throughput Proteomic Microarrays". In: *Molecular, Biological and Multi-Scale Communications, IEEE Transactions on* 1.1 (2015), pp. 50–61.

[44] Peter Kieseberg, Manuel Leithner, Martin Mulazzani, Lindsay Munroe, Sebastian Schrittwieser, Mayank Sinha, and Edgar Weippl. "QR code security". In: *Proceedings of the 8th International Conference on Advances in Mobile Computing and Multimedia*. ACM. 2010, pp. 430–435.

[45] Dieter Klemm, Friederike Kramer, Sebastian Moritz, Tom Lindström, Mikael Ankerfors, Derek Gray, and Annie Dorris. "Nanocelluloses: A new family of nature-based materials". In: *Angewandte Chemie International Edition* 50.24 (2011), pp. 5438–5466.

[46] Kaneyuki Kurokawa. "Power waves and the scattering matrix". In: *Microwave Theory and Techniques, IEEE Transactions on* 13.2 (1965), pp. 194–202.

[47] Sungjun Kwon, Hyunseok Kim, and Kwang Suk Park. "Validation of heart rate extraction using video imaging on a built-in camera system of a smartphone". In: *Engineering in Medicine and Biology Society (EMBC), 2012 Annual International Conference of the IEEE*. IEEE. 2012, pp. 2174–2177.

[48] Alan BG Lansdown. "Silver in health care: antimicrobial effects and safety in use". In: *Biofunctional textiles and the skin*. Vol. 33. Karger Publishers, 2006, pp. 17–34.

[49] Hee-Jo Lee, Jung-Hyun Lee, Hui-Sung Moon, Ik-Soon Jang, Jong-Soon Choi, Jong-Gwan Yook, and Hyo-Il Jung. "A planar split-ring resonator-based microwave biosensor for label-free detection of biomolecules". In: *Sensors and Actuators B: Chemical* 169 (2012), pp. 26–31.

[50] Hee-Jo Lee and Jong-Gwan Yook. "Biosensing using split-ring resonators at microwave regime". In: *Applied Physics Letters* 92.25 (2008), pp. 254103–254103.

[51] Seung Ah Lee and Changhuei Yang. "A smartphone-based chip-scale microscope using ambient illumination". In: *Lab on a Chip* 14.16 (2014), pp. 3056–3063.

[52] F. Lens. *The first flashlight booster for smartphones*. URL: `http://www.relio.it/flens`.

[53] Hailong Li, Yaqing Liu, Shaojun Dong, and Erkang Wang. "DNA-based advanced logic circuits for nonarithmetic information processing". In: *NPG Asia Materials* 7.3 (2015), e166.

[54] Xu Li, David R Ballerini, and Wei Shen. "A perspective on paper-based microfluidics: current status and future trends". In: *Biomicrofluidics* 6.1 (2012), p. 011301.

[55] Xu Li, Junfei Tian, and Wei Shen. "Progress in patterned paper sizing for fabrication of paper-based microfluidic sensors". In: *Cellulose* 17.3 (2010), pp. 649–659.

[56] Zhongjian Li, Miriam A Rosenbaum, Arvind Venkataraman, Tsz Kin Tam, Evgeny Katz, and Largus T Angenent. "Bacteria-based AND logic gate: a decision-making and self-powered biosensor". In: *Chemical Communications* 47.11 (2011), pp. 3060–3062.

[57] Xiong Liu, Mark Atwater, Jinhai Wang, and Qun Huo. "Extinction coefficient of gold nanoparticles with different sizes and different capping ligands". In: *Colloids and Surfaces B: Biointerfaces* 58.1 (2007), pp. 3–7.

[58] Yang Liu. *Forward error correction biosensors: Principles, modeling, and fabrication*. Michigan State University, 2010.

[59] Yang Liu and Shantanu Chakrabartty. "Factor graph-based biomolecular circuit analysis for designing forward error correcting biosensors". In: *Biomedical Circuits and Systems, IEEE Transactions on* 3.3 (2009), pp. 150–159.

[60] Yang Liu, Shantanu Chakrabartty, and Evangelyn C Alocilja. "Fundamental building blocks for molecular biowire based forward error-correcting biosensors". In: *Nanotechnology* 18.42 (2007), p. 424017.

[61] Yang Liu, Ming Gu, Evangelyn C Alocilja, and Shantanu Chakrabartty. "Co-detection: Ultra-reliable nanoparticle-based electrical detection of biomolecules in the presence of large background interference". In: *Biosensors and Bioelectronics* 26.3 (2010), pp. 1087–1092.

[62] Yang Liu, Deng Zhang, Evangelyn C Alocilja, and Shantanu Chakrabartty. "Biomolecules detection using a silver-enhanced gold nanoparticle-based biochip". In: *Nanoscale Research Letters* 5.3 (2010), pp. 533–538.

[63] Vigneshwaran Mani, Karteek Kadimisetty, Spundana Malla, Amit A Joshi, and James F Rusling. "Paper-based electrochemiluminescent screening for genotoxic activity in the environment". In: *Environmental science & technology* 47.4 (2013), pp. 1937–1944.

[64] Gaetano Marrocco. "The art of UHF RFID antenna design: impedance-matching and size-reduction techniques". In: *Antennas and Propagation Magazine, IEEE* 50.1 (2008), pp. 66–79.

[65] Andres W Martinez, Scott T Phillips, and George M Whitesides. "Three-dimensional microfluidic devices fabricated in layered paper and tape". In: *Proceedings of the National Academy of Sciences* 105.50 (2008), pp. 19606–19611.

[66] Andres W Martinez, Scott T Phillips, George M Whitesides, and Emanuel Carrilho. "Diagnostics for the developing world: microfluidic paper-based analytical devices". In: *Analytical chemistry* 82.1 (2009), pp. 3–10.

[67] Nikolaus Meyerbröker and Michael Zharnikov. "Hydrogel Nanomembranes as Templates for Patterned Deposition of Nanoparticles on Arbitrary Substrates". In: *ACS applied materials & interfaces* 6.16 (2014), pp. 14729–14735.

[68] *Multistate Outbreak of Listeriosis Linked to Blue Bell Creameries Products*. URL: `http://www.cdc.gov/listeria/outbreaks/ice-cream-03-15/`.

[69] Rachel D Near, Steven C Hayden, Ronald E Hunter Jr, Daniel Thackston, and Mostafa A El-Sayed. "Rapid and efficient prediction of optical extinction coefficients for gold nanospheres and gold nanorods". In: *The Journal of Physical Chemistry C* 117.45 (2013), pp. 23950–23955.

[70] Zhihong Nie, Frédérique Deiss, Xinyu Liu, Ozge Akbulut, and George M Whitesides. "Integration of paper-based microfluidic devices with commercial electrochemical readers". In: *Lab on a Chip* 10.22 (2010), pp. 3163–3169.

[71] Julaluk Noiphung, Temsiri Songjaroen, Wijitar Dungchai, Charles S Henry, Orawon Chailapakul, and Wanida Laiwattanapaisal. "Electrochemical detection of glucose from whole blood using paper-based microfluidic devices". In: *Analytica chimica acta* 788 (2013), pp. 39–45.

[72] Charles E Ophardt. "Virtual chembook". In: *Elmhurst College* (2003), pp. 121–125.

[73] So-Jung Park, T Andrew Taton, and Chad A Mirkin. "Array-based electrical detection of DNA with nanoparticle probes". In: *Science* 295.5559 (2002), pp. 1503–1506.

[74] *Rapid Lateral Flow Test Strips: Considerations for Product Development*. URL: `https://www.emdmillipore.com/US/en/products/ivd-oem-materials-reagents/lateral-flow-membranes/n6mb.qB.L0YAAAE_gut3.Lxi,nav`.

[75] Sumit Roy et al. "RFID: From supply chains to sensor nets". In: *Proceedings of the IEEE* 98.9 (2010), pp. 1583–1592.

[76] Tu San Park, Wenyue Li, Katherine E McCracken, and Jeong-Yeol Yoon. "Smartphone quantifies Salmonella from paper microfluidics". In: *Lab on a Chip* 13.24 (2013), pp. 4832–4840.

[77] Murilo Santhiago, Charles S Henry, and Lauro T Kubota. "Low cost, simple three dimensional electrochemical paper-based analytical device for determination of p-nitrophenol". In: *Electrochimica Acta* 130 (2014), pp. 771–777.

[78] Robert L Scharff. "State estimates for the annual cost of foodborne illness". In: *Journal of food protection* 78.6 (2015), pp. 1064–1071.

[79] Hyojeong Shin, Yohan Chon, and Hojung Cha. "Unsupervised construction of an indoor floor plan using a smartphone". In: *Systems, Man, and Cybernetics, Part C: Applications and Reviews, IEEE Transactions on* 42.6 (2012), pp. 889–898.

[80] Johan Siden, Xuezhi Zeng, Tomas Unander, Andrey Koptyug, and Hans-Erik Nilsson. "Remote moisture sensing utilizing ordinary RFID tags". In: *Sensors, 2007 IEEE*. IEEE. 2007, pp. 308–311.

[81] Arunan Skandarajah, Clay D Reber, Neil A Switz, and Daniel A Fletcher. "Quantitative imaging with a mobile phone microscope". In: *PloS one* 9.5 (2014), e96906.

[82] Guinevere Strack, Marcos Pita, Maryna Ornatska, and Evgeny Katz. "Boolean logic gates that use enzymes as input signals". In: *ChemBioChem* 9.8 (2008), pp. 1260–1266.

[83] Aidong Sun, Yan Sun, and Caixing Liu. "The QR-code reorganization in illegible snapshots taken by mobile phones". In: *Computational Science and its Applications, 2007. ICCSA 2007. International Conference on*. IEEE. 2007, pp. 532–538.

[84] SupplyChainDigest. *RFID News: Looking Back at the Wal-Mart RFID Time Line*. URL: `http://www.scdigest.com/assets/On_Target/09-02-23-1.php`.

[85] Nicole K Thom, Kimy Yeung, Marley B Pillion, and Scott T Phillips. ""Fluidic batteries" as low-cost sources of power in paper-based microfluidic devices". In: *Lab on a Chip* 12.10 (2012), pp. 1768–1770.

[86] Limei Tian, Qisheng Jiang, Keng-Ku Liu, Jingyi Luan, Rajesh R Naik, and Srikanth Singamaneni. "Bacterial Nanocellulose-Based Flexible Surface Enhanced Raman Scattering Substrate". In: *Advanced Materials Interfaces* (2016).

[87] Limei Tian, Sirimuvva Tadepalli, Mikella E Farrell, Keng-Ku Liu, Naveen Gandra, Paul M Pellegrino, and Srikanth Singamaneni. "Multiplexed charge-selective surface enhanced Raman scattering based on plasmonic calligraphy". In: *Journal of Materials Chemistry C* 2.27 (2014), pp. 5438–5446.

[88] Limei Tian, Sirimuvva Tadepalli, Sang Hyun Park, Keng-Ku Liu, Jeremiah J Morrissey, Evan D Kharasch, Rajesh R Naik, and Srikanth Singamaneni. "Bioplasmonic calligraphy for multiplexed label-free biodetection". In: *Biosensors and Bioelectronics* 59 (2014), pp. 208–215.

[89] Thomas C Tisone and Brendan O'Farrell. *Manufacturing the next generation of highly sensitive and reproducible lateral flow immunoassay*. Springer, 2009.

[90] Andrew D Warren, Gabriel A Kwong, David K Wood, Kevin Y Lin, and Sangeeta N Bhatia. "Point-of-care diagnostics for noncommunicable diseases using synthetic urinary biomarkers and paper microfluidics". In: *Proceedings of the National Academy of Sciences* 111.10 (2014), pp. 3671–3676.

[91] Stephen B Wicker and Vijay K Bhargava. *Reed-Solomon codes and their applications*. John Wiley & Sons, 1999.

[92] Zhen-Yu Wu, Hai-Wei Liang, Li-Feng Chen, Bi-Cheng Hu, and Shu-Hong Yu. "Bacterial Cellulose: A Robust Platform for Design of Three Dimensional Carbon-Based Functional Nanomaterials". In: *Accounts of chemical research* 49.1 (2015), pp. 96–105.

[93] Ali Kemal Yetisen, Muhammad Safwan Akram, and Christopher R Lowe. "Paper-based microfluidic point-of-care diagnostic devices". In: *Lab on a Chip* 13.12 (2013), pp. 2210–2251.

[94] Jinghua Yu, Lei Ge, Jiadong Huang, Shoumei Wang, and Shenguang Ge. "Microfluidic paper-based chemiluminescence biosensor for simultaneous determination of glucose and uric acid". In: *Lab on a Chip* 11.7 (2011), pp. 1286–1291.

[95] M Yuan, EC Alocilja, and S Chakrabartty. "Self-Powered Wireless Affinity-Based Biosensor Based on Integration of Paper-Based Microfluidics and Self-Assembled RFID Antennas." In: *IEEE transactions on biomedical circuits and systems* 10.4 (2016), pp. 799–806.

[96] Mingquan Yuan, Evangelyn C Alocilja, and Shantanu Chakrabartty. "A novel biosensor based on silver-enhanced self-assembled radio-frequency antennas". In: *IEEE Sensors Journal* 14.4 (2014), pp. 941–942.

[97] Mingquan Yuan, Evangelyn C Alocilja, and Shantanu Chakrabartty. "A novel biosensor based on silver-enhanced self-assembled radio-frequency antennas". In: *IEEE Sensors Journal* 14.4 (2014), pp. 941–942.

[98] Mingquan Yuan, Evangelyn C Alocilja, and Shantanu Chakrabartty. "Self-powered wireless biosensing based on integration of paper-based microfluidics with self-assembling RFID antennas". In: *Biomedical Circuits and Systems Conference (BioCAS), 2015 IEEE*. IEEE. 2015, pp. 1–4.

[99] Mingquan Yuan, Premjeet Chahal, Evangelyn C Alocilja, and Shantanu Chakrabartty. "Sensing by growing antennas: A novel approach for designing passive RFID based biosensors". In: *Circuits and Systems (ISCAS), 2015 IEEE International Symposium on*. IEEE. 2015, pp. 2121–2124.

[100] Mingquan Yuan, Premjeet Chahal, Evangelyn C Alocilja, and Shantanu Chakrabartty. "Sensing by growing antennas: A novel approach for designing passive RFID based biosensors". In: *Circuits and Systems (ISCAS), 2015 IEEE International Symposium on*. IEEE. 2015, pp. 2121–2124.

[101] Mingquan Yuan, Premjeet Chahal, Evangelyn C Alocilja, and Shantanu Chakrabartty. "Wireless Biosensing Using Silver-Enhancement Based Self-Assembled Antennas in Passive Radio Frequency Identification (RFID) Tags". In: *Sensors Journal, IEEE* 15.8 (2015), pp. 4442–4450.

[102] Mingquan Yuan, Premjeet Chahal, Evangelyn C Alocilja, and Shantanu Chakrabartty. "Wireless biosensing using silver-enhancement based self-assembled antennas in passive radio frequency identification (RFID) tags". In: *IEEE Sensors Journal* 15.8 (2015), pp. 4442–4450.

[103] Mingquan Yuan, Qisheng Jiang, Keng-Ku Liu, Srikanth Singamaneni, and Shantanu Chakrabartty. "Towards an Integrated QR Code Biosensor: Light-Driven Sample Acquisition and Bacterial Cellulose Paper Substrate". In: *IEEE transactions on biomedical circuits and systems* (2018).

[104] Mingquan Yuan, Keng-ku Liu, Srikanth Singamaneni, and Shantanu Chakrabartty. "Analyte sampling in paper biosensors powered by graphite-based light absorption". In: *Circuits and Systems (ISCAS), 2017 IEEE International Symposium on*. IEEE. 2017, pp. 1–4.

[105] Mingquan Yuan, Keng-ku Liu, Srikanth Singamaneni, and Shantanu Chakrabartty. "Self-powered Forward Error-correcting Biosensor based on Integration of Paper-based Microfluidics and Self-assembled Quick Response Codes". In: *IEEE transactions on biomedical circuits and systems* 10.5 (2016), pp. 963–971.

[106] Peter J Yunker, Tim Still, Matthew A Lohr, and AG Yodh. "Suppression of the coffee-ring effect by shape-dependent capillary interactions". In: *Nature* 476.7360 (2011), pp. 308–311.

[107] Jian Zhou, Mary A Arugula, Jan Halamek, Marcos Pita, and Evgeny Katz. "Enzyme-based NAND and NOR logic gates with modular design". In: *The Journal of Physical Chemistry B* 113.49 (2009), pp. 16065–16070.

[108] Xiaowei Zhu, Samar K Mukhopadhyay, and Hisashi Kurata. "A review of RFID technology and its managerial applications in different industries". In: *Journal of Engineering and Technology Management* 29.1 (2012), pp. 152–167.

Appendix A

Supporting Information: XNOR Biomolecular Gate Construction

A.1 Effect of $AgNO_3$ on HRP

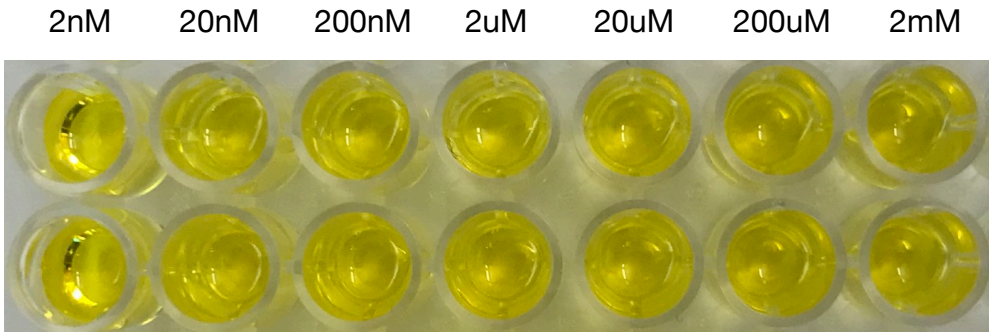

Figure A.1: Visual assessment of $AgNO_3$ of different concentrations (ranging from 2nM to 2mM) on HRP activity

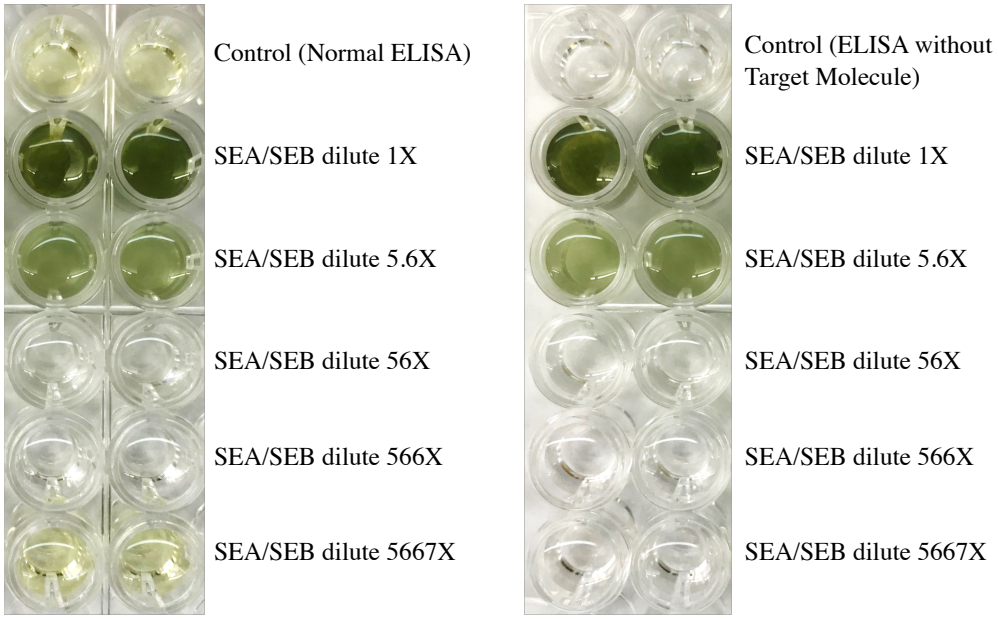

Figure A.2: Visual assessment of the effect of silver enhancer reagent with different dilution levels on color development.

A.2 Effect of silver enhancement reagent on colorimetric measurement

Measurements in Fig. A.3 and A.4 show the effect of silver enhancement reagent on colorimetric measurement, and were collected according to a normal KIM-1 ELISA procedure. Target molecules with a concentration of 0.5 ng/ml were applied to each well. After adding streptavidin-HRP at the final step, it was then followed with PBS buffer wash for 3 times and water wash twice. The purpose of DI water washing is to remove salts contained in PBS buffer which have been proved to have an effect on the experiment outcomes. Then all water inside the wells has been removed. A freshly prepared solution mixer, containing silver enhancer, AuNRs and H_2O, has been applied to each well. It was followed with applying HRP substrate, tetramethylbenzidine (TMB), for color development. Measurements shown in Fig. A.3 and Fig. A.4 were collected 20 minutes after applying TMB.

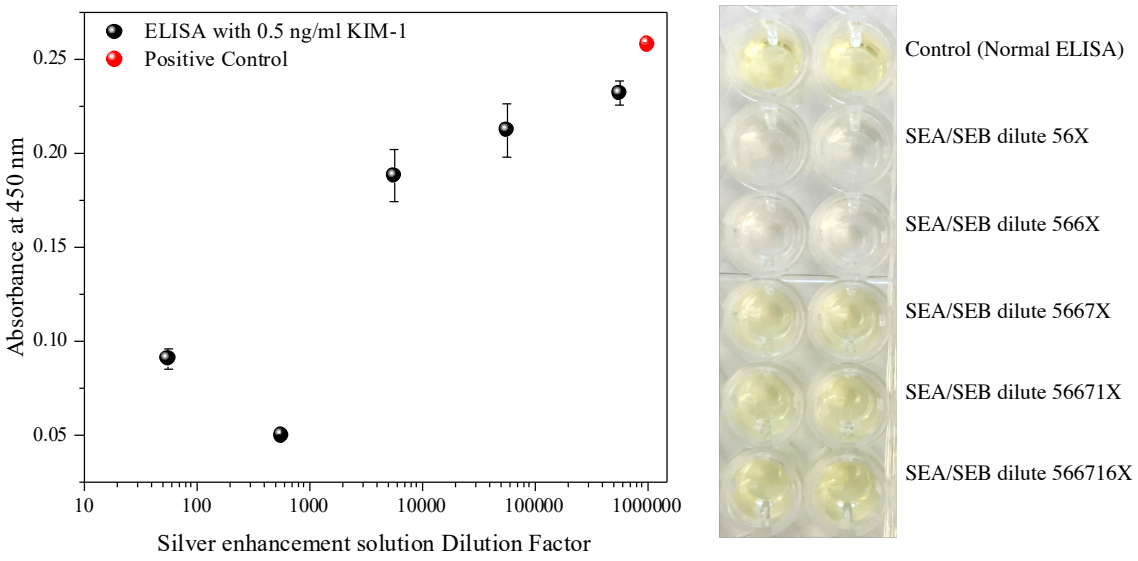

(a) (b)

Figure A.3: Effect of silver enhancement reagent on colorimetric measurement: (a) absorbance of the solution at 450nm with respect to different silver enhancer dilution factors; (b) visual assessment of the effect of silver enhancement with different dilution levels on color development.

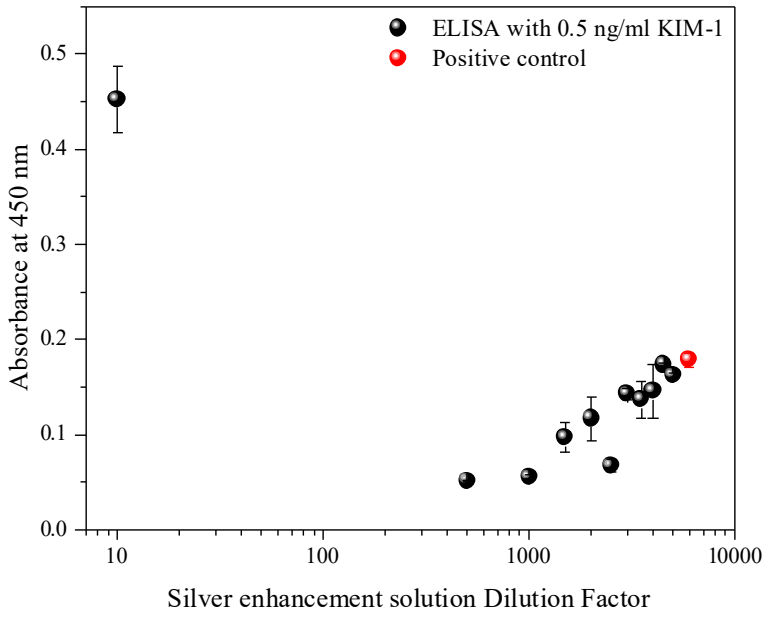

(a)

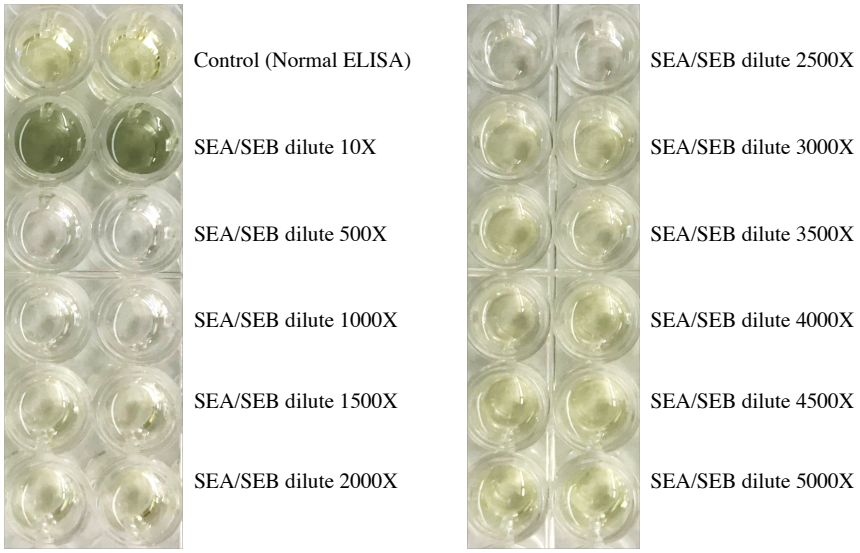

(b)

Figure A.4: Effect of silver enhancement reagent on colorimetric measurement: (a) absorbance of the solution at 450nm with respect to different silver enhancer dilution factors; (b) photos showing the effect of silver enhancement with different dilution levels on color development.

A.3 Effect of AuNR on HRP activity

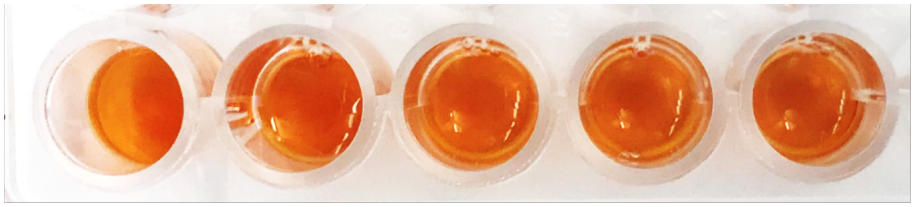

(a) (b) (c) (d) (e)

Figure A.5: Visual assessment of effect of AuNR with different concentrations on HRP activity.

Table A.1: AuNR with different concentrations used in Fig. A.5 to show its effect on colorimetric assessment

(a)	30μl PBS buffered HRP + 30μl **H_2O** + 10μl Dopamine + 30μl 0.3% H_2O_2
(b)	30μl PBS buffered HRP + 30μl **ext 0.45 AuNRs** + 10μl Dopamine + 30μl 0.3% H_2O_2
(c)	30μl PBS buffered HRP + 30μl **ext 0.90 AuNRs** + 10μl Dopamine + 30μl 0.3% H_2O_2
(d)	30μl PBS buffered HRP + 30μl **ext 1.34 AuNRs** + 10μl Dopamine + 30μl 0.3% H_2O_2
(e)	30μl PBS buffered HRP + 30μl **ext 1.80 AuNRs** + 10μl Dopamine + 30μl 0.3% H_2O_2

A.4 Effect of PBS buffer on colorimetric measurement

Table A.2: Reagents used in Fig. A.6(a)

Tube 1	30μl HRP + 5μl AuNR + 15μl SE + 5μl Dopamine + 1μl H_2O_2
Tube 2	15μl HRP + **15μl H_2O** + 5μl AuNR + 15μl SE + 5μl Dopamine + 1μl H_2O_2
Tube 3	**30μl H_2O** + 5μl AuNR + 15μl SE + 5μl Dopamine + 1μl H_2O_2

Table A.3: Reagents used in Fig. A.6(b)

Tube 1	30μl HRP + 5μl AuNR + 15μl SE + 5μl Dopamine + 1μl H_2O_2
Tube 2	15μl HRP + **15μl PBS** + 5μl AuNR + 15μl SE + 5μl Dopamine + 1μl H_2O_2
Tube 3	**30μl PBS** + 5μl AuNR + 15μl SE + 5μl Dopamine + 1μl H_2O_2

Table A.4: Reagents used in Fig. A.7

Tube 1	**30μl H_2O** + 7.5μl SEA + 5μl Dopamine
Tube 2	**15μl H_2O + 15μl PBS** + 7.5μl SEA + 5μl Dopamine

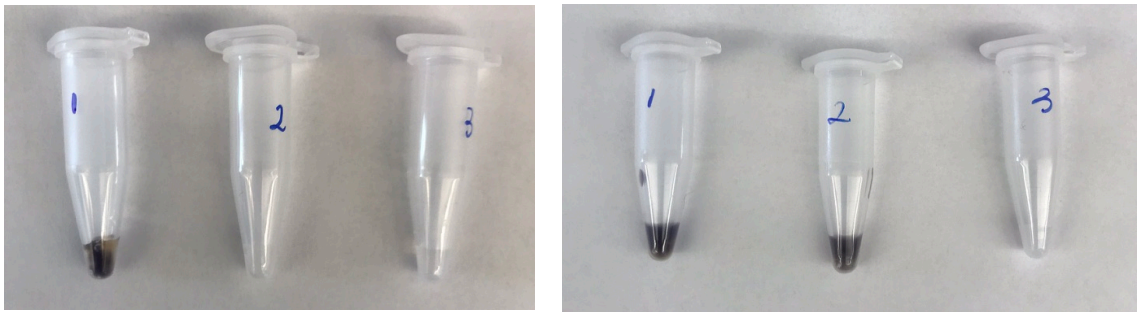

(a) (b)

Figure A.6: Visual assessment showing effect of PBS on color development.

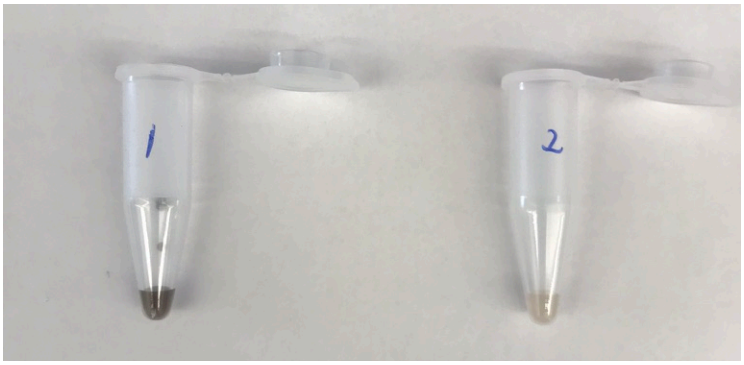

Figure A.7: Black color in tube 1 is due to reaction between dopamine and $AgNO_3$ which is consumed by Cl^- (due to PBS) to generate AgCl in tube 2.

A.5 Silver nitrate and dopamine

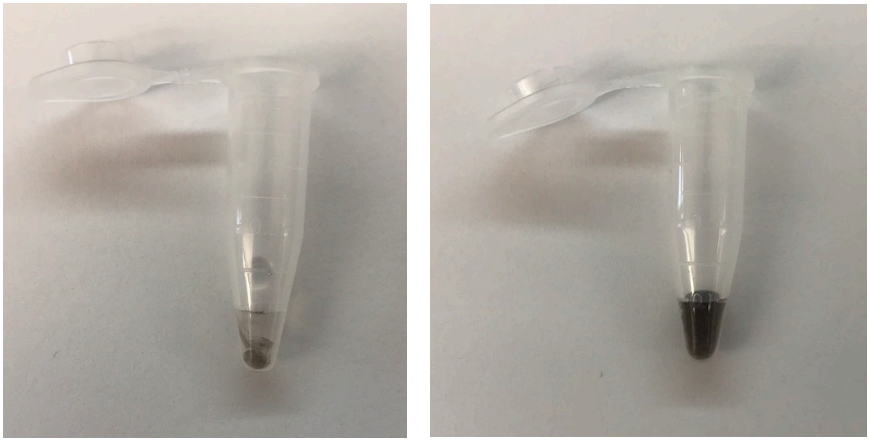

(a) (b)

Figure A.8: Black sediment is generated immediately after adding (a) 1μl and (b) 10μl 100mM $AgNO_3$ into dopamine solution.